Spaceborne SAR Remote Sensing for Monitoring of Vegetation Dynamics in Arid and Semi-arid Environment

Dissertation

zur

Erlangung des Doktorgrades (Dr. rer. nat.)

der

Mathematisch-Naturwissenschaftlichen Fakultät

der

Rheinischen Friedrich-Wilhelms-Universität Bonn

vorgelegt von

Ayman Eliewa Elsayed Abdelhamid Bahteamy

aus

Sharkia, Ägypten

Bonn, 2019

Angefertigt mit Genehmigung der Mathematisch-Naturwissenschaftlichen Fakultät der Rheinischen Friedrich-Wilhelms-Universität Bonn

1. Gutachter : PD Dr. Olena Dubovyk
2. Gutachter : Prof. Dr. Klaus Greve

Tag der Promotion: 23.03.2020
Erscheinungsjahr: 2020.

Preface

This thesis is submitted in partial fulfilment of the requirements for obtaining the Ph.D. degree in Natural Sciences (*Doctor rerum naturalium*) at the University of Bonn. The work described in this thesis was conducted at the Center for Remote Sensing of Land Surfaces (ZFL), at the University of Bonn, under the supervision of Prof. Dr. Gunter Menz, PD Dr. Olena Dubovyk, and Prof. Dr. Klaus Greve. The thesis follows a paper-based approach in accordance with the guidelines of the University of Bonn and includes the following articles:

[1] **Abdel-Hamid A.**, Dubovyk O., Abou El-Magd I., and Menz G. 2018. Mapping mangroves extents on the Red Sea coastline in Egypt using polarimetric SAR and high resolution optical remote sensing data, *Sustainability*, 10, 646.

[2] **Abdel-Hamid A.**, Dubovyk O., Graw V., and Greve K. 2019. Assessing the impact of drought stress on grasslands using multi-temporal SAR data of Sentinel-1: A case study in Eastern Cape, South Africa, *European Journal of Remote Sensing*, in Review.

[3] **Abdel-Hamid A.**, Dubovyk O., and Greve K. 2019. The potential of Sentinel-1 InSAR coherence for grasslands monitoring in Eastern Cape, South Africa [Manuscript].

The following conferences proceedings and other co-authored publications were also written during the Ph.D. period, and deal with the general topic of the thesis:

[4] **Abdel-Hamid A.**, Dubovyk O., Abou El-Magd I., and Menz G. 2017. Integration of SAR and Optical remote sensing data for mapping of mangroves extents. In Benoît Otjacques, Patrik Hitzelberger, Stefan Naumann (Eds.) - From Science to Society: The Bridge provided by Environmental Informatics Proceedings of the 31st EnviroInfo conference, Neimenster Abbey, Luxemburg.

[5] Graw, V., Ghazaryan, G., Dall, K., Delgado Gómez, A., **Abdel-Hamid, A.**, Jordaan, A., Piroska, R., Post, J., Szarzynski, J., Walz, Y., and Dubovyk, O. 2017. Drought Dynamics and Vegetation Productivity in Different Land

Management Systems of Eastern Cape, South Africa—A Remote Sensing Perspective. *Sustainability*, 9, 1728.

[6] **Abdel-Hamid A.**, Dubovyk O., Graw V., and Greve K. 2018. Multi-temporal SAR data of Sentinel-1 for assessing the impact of drought stress on grasslands in Eastern Cape, South Africa. 38th EARSeL Symposium on Earth Observation Supporting Sustainability Research, 9-12 July 2018, Chania, Greece.

[7] Graw, V., Ghazaryan, G., Schreier, J., Gonzalez, J., **Abdel-Hamid, A.,** Walz, Y., Dall, K.; Post, J., Jordaan, A., and Dubovyk, O. 2018. Timing is everything – drought classification for risk assessment. In Proceedings of IEEE International Geoscience and Remote Sensing Symposium IGARSS 2018, Valencia, Spain, pp. 8267–8270.

Ayman Abdel-Hamid
Bonn, October 2019

Acknowledgements

This work could not have been completed without the support of many people. Here I would like to take this opportunity to express my deepest gratitude.

Firstly, I am very grateful to Prof. Dr. Gunter Menz who gave me the opportunity to join the Center for Remote Sensing of Land Surfaces (ZFL) at the University of Bonn to develop my research project and supported me during the first year of my doctoral study.

I would like to express my special appreciation and thanks to PD. Dr. Olena Dubovyk for her continuous support, and for discussing my findings and sharing her experience. I extend my appreciation and gratitude to Prof. Dr. Klaus Greve for his support, encouragement, and valuable advice.

I am appreciative to the team members of ZFL and the Remote Sensing Research Group (RSRG) at the University of Bonn, for their support. I would like to thank my colleagues; Javier Gonzalez, Valerie Graw, Javier Muro, Adrian Strauch, Frank Thonfeld, Fabian Santos, Andreas Tewes, Gohar Gahzaryan, Paul Heid, and Jonas Schreier. Special thanks go to Ellen Götz and Carsten Oldenburg for their support and assistance in the administrative and IT issues. I would like to thank Dr. Guido Lüchters from the Center for Environment and Development (ZEF) for his support, thanks extended to Dr. Günther Manske and Mrs. Maike Retat-Amin from ZEF for their support.

I would like to thank my colleagues and friends at the National Authority for Remote Sensing and Space Sciences (NARSS) in Cairo, Egypt, for their support and encouragement. My thanks extended to my colleagues at Wadi El-Gemal-Hamata Office, Nature Conservation Sector, for their support during the fieldwork on the Red Sea coastal area in Egypt. Furthermore, I would like to thank the research group of the Disaster Management Training and Education Centre for Africa (DiMTEC) at the University of Free State for their support during the fieldwork in South Africa.

A special thanks to my family, words cannot express how grateful I am to my parents for all of the sacrifices that they have made on my behalf. I would like to thank my brother and my sister for their support and encouragement, my thanks extended to my big family and friends in Ismailia for their support and encouragement.

Finally, I am truly grateful to my wife Hadier and my daughter Menna for their support, encouragement, and patience during my Ph.D. study. I dedicate this dissertation to them.

Abstract

Drylands are under constant threat from multiple stresses and challenges, which occur as a result of a complex interaction of natural processes, and human-induced processes caused by unsustainable land use practices, leading to vegetation degradation and desertification, which is believed to be one of the most serious environmental problems. Understanding the existing distribution of vegetation in the drylands, and changes in vegetation properties in response to climate change and land use change is essential for conservation and sustainable management of vegetation in this environment. This research focused on mapping and monitoring of vegetation in the arid and semi-arid regions in the drylands of Africa.

Assessment of the state of vegetation and their dynamics relies on the use of optical remote sensing data. Although there are many advantages of using optical remote sensing data, a major limitation is the availability of cloud-free scenes, which stimulates studies of other remote sensing data sources such as the Synthetic Aperture Radar (SAR). SAR data have been used to complement the cloud problems of optical sensor images because SAR data are not influenced by weather conditions. To explore the potential of spaceborne SAR data for mapping and monitoring of vegetation in the drylands of Africa, we selected two main vegetation types in the arid and semi-arid environment, namely; mangroves and grasslands.

Mangroves are among the most productive ecosystems, providing many critical ecological functions and ecosystem services. Despite of their economic and ecological importance, they experience high yearly loss rates due to unmanaged human activities, including; over-cutting, over-grazing, and habitat destruction. This places other environmental services provided by mangroves at considerable risk. There is a growing demand for mapping of mangroves extents, especially in the context of climate change and land use change. In this thesis, we integrated SAR data of ALOS/PALSAR with high resolution optical data of RapidEye for mapping of mangroves extents on the Red Sea coastline. We applied the object-based image analysis method and evaluated different machine learning algorithms and various input features, such as; spectral properties, texture features, and SAR derived parameters. The object-based analysis allowed clearly discriminating the different land cover classes within mangroves ecosystem, producing accurate maps of mangroves in the study area, as well as making recommendations on the suitability

of remote sensing data and selection of the classification methods for accurate mangroves mapping.

The importance of grasslands lies in supporting human, fauna and flora populations by providing numerous goods and services. However, the ecosystem services provided by grasslands, they are facing several pressures, including the impact of drought. It has been one of the major factors influencing vegetation dynamics in grasslands, with substantial social and economic consequences. This makes it essential to monitor the grasslands state on a repeated and regular basis.

We assessed the impact of drought on grasslands in Eastern Cape Province, using multi-temporal analysis of Sentinel-1 SAR backscattering and InSAR coherence and applying linear mixed-effects regression analysis. This also allowed us to detect the impact of drought on communal and commercial grasslands during drought and non-drought seasons. Results indicated that vegetation dynamics in grasslands ecosystems in the study area are highly responsive to climatic fluctuations. In addition, communal grasslands are more affected by drought impact than commercial grasslands due to the unsustainable use of resources in the communal grasslands, while in commercial grasslands, management activities were able to improve the growing conditions, reduce the impact of drought stress, and subsequently increase the resilience and productivity of this ecosystem.

Results of this research confirmed the feasibility of using Spaceborne SAR data for mapping and monitoring of vegetation state and dynamics in the arid and semi-arid environment in Africa. SAR remote sensing data have shown their potential to derive spatial information from both mangroves ecosystems and grasslands. The elaborated approach can serve as decision-making support for developing a regional action plan for conservation and management of vegetation in the arid and semi-arid environment, as well as it could be applied for similar applications worldwide.

Zusammenfassung

Trockengebiete sind einer ständigen Bedrohung durch vielfältige Belastungen und Herausforderungen ausgesetzt, die sich aus einem komplexen Zusammenspiel natürlicher Prozesse und durch Menschen verursachter Prozesse aufgrund nicht nachhaltiger Landnutzungspraktiken ergeben. Dies führt zu Vegetationsabbau und Wüstenbildung, was als eines der schwerwiegendsten Umweltprobleme angesehen wird. Das Verständnis der vorhandenen Vegetationsverteilung in den Trockengebieten, die Veränderungen der Vegetationseigenschaften als Reaktion auf den Klimawandel und die Änderung der Landnutzung sind für die Erhaltung und nachhaltige Bewirtschaftung der Vegetation in dieser Umgebung von wesentlicher Bedeutung. Diese Forschung konzentrierte sich auf die Kartierung und das Monitoring der Vegetation in den ariden und semi-ariden Regionen in den Trockengebieten Afrikas.

Die Beurteilung des Vegetationszustands und seiner Dynamik stützt sich auf die Verwendung optischer Fernerkundungsdaten. Obwohl die Verwendung optischer Fernerkundungsdaten viele Vorteile bietet, besteht eine wesentliche Einschränkung in der Verfügbarkeit wolkenfreier Szenen, die Studien zu anderen Fernerkundungsdatenquellen wie dem Synthetic Aperture Radar (SAR) anregen.. Um das Potenzial weltraumgestützter SAR-Daten für die Kartierung und das Monitoring der Vegetation in den Trockengebieten Afrikas zu untersuchen, haben wir zwei Hauptvegetationstypen in ariden und semi-ariden Gebieten ausgewählt: Mangroven und Grasland.

Mangroven gehören zu den produktivsten Ökosystemen und bieten viele wichtige ökologische Funktionen und Ökosystemleistungen. Trotz ihrer wirtschaftlichen und ökologischen Bedeutung weisen sie hohe jährliche Verlustraten aufgrund nicht verwalteter menschlicher Aktivitäten auf. Dies birgt ein erhebliches Risiko für andere durch Mangroven erbrachte Umweltleistungen. Es besteht ein wachsender Bedarf an der Kartierung von Mangrovenbeständen. In dieser Arbeit haben wir SAR-Daten von ALOS / PALSAR mit hochauflösenden optischen Daten von RapidEye für die Kartierung von Mangroven-Ausmaßen an der Küste des Roten Meeres integriert. Dabei haben wir die objektbasierte Bildanalysemethode angewendet und verschiedene Algorithmen für maschinelles Lernen und verschiedene Eingabemerkmale ausgewertet. Die objektbasierte Analyse ermöglichte eine klare Unterscheidung der verschiedenen Landbedeckungsklassen innerhalb des

Mangroven-Ökosystems, die Erstellung genauer Karten der Mangroven im Untersuchungsgebiet sowie Empfehlungen zur Eignung von Fernerkundungsdaten.

Die Bedeutung von Grasland liegt in der Unterstützung der Bevölkerung, der Fauna und Flora durch die Bereitstellung zahlreicher Waren und Dienstleistungen. Bei den von Grasland erbrachten Ökosystemleistungen sind sie jedoch mehreren Belastungen ausgesetzt, einschließlich der Auswirkungen von Dürreperioden. Es war einer der Hauptfaktoren, der die Vegetationsdynamik in Grasland mit erheblichen sozialen und wirtschaftlichen Folgen beeinflusste. Daher ist es wichtig, den Graslandzustand in regelmäßig Abständen zu überwachen. Um die Auswirkung der Dürre auf Grasland in der Provinz Ostkap zu bewerten, verwendeten wir eine mehrzeitige Analyse der Sentinel-1-SAR-Rückstreuung und der InSAR-Kohärenz. Die Ergebnisse zeigten, dass die Vegetationsdynamik in Graslandökosystemen im Untersuchungsgebiet stark auf klimatische Schwankungen reagiert. Außerdem sind kommunale Graslandflächen aufgrund der nicht nachhaltigen Ressourcennutzung in den kommunalen Graslandflächen stärker von Dürreeinflüssen betroffen als gewerbliche Graslandflächen. In gewerblichen Graslandflächen konnten die Bewirtschaftungsmaßnahmen die Wachstumsbedingungen verbessern, die Auswirkungen von Trockenstress verringern und anschließend Steigern Sie die Belastbarkeit und Produktivität dieses Ökosystems.

Die Ergebnisse dieser Studie bestätigten die Machbarkeit der Verwendung weltraumgestützter SAR-Daten zur Kartierung und Monitoring des Vegetationszustands und der Vegetationsdynamik in ariden und semi-ariden Gebieten in Afrika. SAR-Fernerkundungsdaten haben gezeigt, dass sie räumliche Informationen sowohl aus Mangrovenökosystemen als auch aus Grasland ableiten können. Der ausgearbeitete Ansatz kann als Entscheidungshilfe für die Entwicklung eines regionalen Aktionsplans zur Erhaltung und Bewirtschaftung der Vegetation in ariden und semi-ariden Gebieten dienen und für ähnliche Anwendungen weltweit angewendet werden.

Table of Contents

List of Figures

List of Tables

List of Abbreviations

ALOS	Advanced Land Observing Satellite
COSMO-Skymed	Constellation of small Satellites for the Mediterranean basin Observatory
DLR	Deutsches Zentrum für Luft- und Raumfahrt (German Aerospace Center)
ENVISAT	Environmental satellite
ERS	European Remote Sensing Satellite
ESA	European Space Agency
EVI	Enhanced Vegetation Index
FBD	Fine Beam Double polarization mode
FBS	Fine Beam Single polarization mode
GCP	Ground Control Point
GRD	Ground Range Detected
InSAR	Interferometric synthetic aperture radar
IW	Interferometric Wide mode
JAXA	Japanese Aerospace Exploration Agency
JERS	Japanese Earth Resources Satellite
MERIS	Medium Resolution Imaging Spectrometer
NASA	National Aeronautics and Space Administration
NDVI	Normalized Difference Vegetation Index
OBIA	Object-based Image Analysis
PALSAR	Phased Array L-band Synthetic Aperture Radar
RE	RapidEye images
RE-ML	Random-effects Maximum Likelihood regression
RF	Random Forests classifier
S1	Sentinel-1 SAR data
SAR	Synthetic Aperture Radar
SLC	Single Look Complex
SNAP	Sentinel Application Platform of the European Space Agency ESA
SRTM	Shuttle Radar Topography Mission
SVM	Support Vector Machine
UTM	Universal Transverse Mercator
VCI	Vegetation condition index
VV	Vertical transmit and receive polarization
WV-1	WorldView-1 images

Chapter 1

Introduction

This chapter provides an introduction to the thesis including; dryland ecosystems, environmental degradation in drylands of Africa, and using SAR remote sensing for mapping and monitoring of vegetation in this environment. The chapter concludes by providing the objectives of the work, research questions, and an outline of the thesis structure.

1. Overview

1.1. Dryland Ecosystems

Drylands cover about 41% of the earth's land surface, comprising hyper-arid to dry sub-humid climate zones that are defined by low mean annual precipitation amounts compared to potential evaporation, that is, a ratio of mean precipitation to potential evaporation less than 0.65 (Thomas and Middleton, 1994; Safriel *et al*., 2005; Stellmes *et al*., 2015, Figure 1.1). They include a large number of ecosystems that belong to the four broad biomes, namely; forests, Mediterranean, grasslands, and deserts (Safriel *et al*., 2005), and are home to about one-third of the global population, with many residents directly depending on dryland ecosystem services (MEA, 2005).

The dominant land uses in drylands are rangelands and croplands, jointly accounting for 90% of dryland areas; while forests and woodlands account for only 10% of the drylands. These land uses, in turn, support the livelihoods of more than two billion people, about one-third of the world population (MEA, 2005). Dryland ecosystems provide different regulatory services, including the provision of food, forage, water, and other resources. Drylands also provide ecosystem services of global significance, such as climate regulation by sequestering and storing vast amounts of carbon due to the large areal extent (Lal, 2004; Stellmes *et al*., 2015).

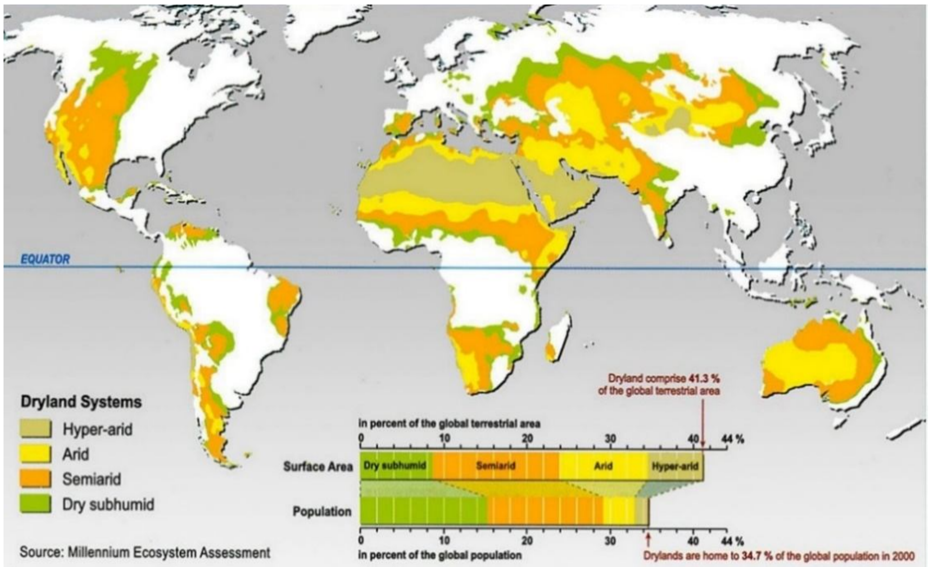

Figure 1.1. Distribution of drylands throughout the world (MEA, 2005).

Arid, semiarid and dry sub-humid areas, collectively denominated drylands, are characterized by unique climatic conditions, including scarce and variable precipitation, high temperatures, and high potential evapotranspiration (Reynolds *et al*., 2007). Most frequently, soils contain low nutritious reserves and have low contents of organic matter and nitrogen (Skujins, 1991). Water availability and the tolerance to periods of water scarcity are key factors in drylands productivity (Stafford Smith *et al*., 2009). In response to water scarcity and climatic variability, drylands' species show many remarkable adaptations to water stress, including the ability to conserve water, to extract water efficiently when it is scarce, or to survive periods without water (Davies *et al*., 2012).

More than half of the African continent can be classified as a dryland system that is characterized by low rainfall and high evapotranspiration. Indeed, Africa contains some of the driest regions on Earth that constitute some of the oldest continually inhabited environments (Templeton, 2002). The human-environment connection in the drylands of Africa forms a complex, interlinked system that provides ecosystem services. The majority of food consumed comes from domestic sources, making the natural system a crucial direct factor that acts both as a source of livelihood and nutrition. However, this system is susceptible to climatic variability that affects the supply of its products, which affects the demand for these products (Barrett and Upton, 2013).

Vegetation degradation is common in the drylands of Africa and this directly leads to soil degradation and desertification (Middleton and D. Thomas, 1997). Desertification threatens the sustainability of land, and is believed to be one of the most serious global environmental problems. The UNCCD definition of desertification emphasizes two main causative factors, notably climatic variations and human activities; particularly removal of natural vegetation cover (UNCCD, 2005). The extent of degradation in semi-arid zones is more influenced by agricultural activities than in the arid zone, while over-exploitation in the arid zone is more important in natural resource degradation (FAO, 2001).

Understanding the existing distribution of vegetation in the drylands of Africa, and changes in vegetation properties in response to climate change and land use change is essential for developing strategies for conservation and sustainable management of vegetation in this environment. It provides crucial information for biogeographic analysis (Siqueira and Durigan, 2007), conservation of rare and/or endangered species (Engler *et al*., 2004), and assists in determining priority areas for conservation (Ortega-Huerta and Peterson, 2004).

2. Mapping and Monitoring of Vegetation in Drylands

Earth observation (EO) data and techniques are the most promising for monitoring environmental changes at multiple scales and high temporal frequencies (Pettorelli *et al*., 2014). EO is essential for providing useful information with a high level of details for large areas with short repetition intervals (Wulder and Franklin, 2003; Masek *et al*., 2015). Such detailed and up-to-date information about vegetation dynamics is necessary for assessment of ecological conditions

(Wulder *et al*., 2004; Zlinszky *et al*., 2015), and for sustainable management (Franklin, 2001). Remote sensing is considered a viable method for gathering information in a spatially and temporally continuous manner. It offers an efficient and reliable means of collecting spatial information required for assessing vegetation dynamics. The development and deployment of satellites have enhanced the collection of remotely sensed data over large areas (Franklin, 2001).

Spaceborne remote sensing is economically competitive with other forms of data collection such as aerial photography, especially where low or moderate resolutions data are adequate. Broad swath widths and the advent of high resolution systems enable frequent repeat coverage of vegetation in the arid and semi-arid environment. Spaceborne systems can also collect data over denied or remote areas without interruption. The capacity of spaceborne remote sensing to identify and monitor land surfaces and environmental conditions has expanded greatly over the last few years and remotely sensed data became an essential tool in natural resources management (Sanderson *et al*., 2002).

3. SAR Data for Mapping and Monitoring of Vegetation in Drylands

A challenge for understanding vegetation dynamics in the arid and semi-arid regions with respect to rapid climate change and land use change has been the lack of sustained observations of ecosystem processes. However, more detailed and area-specific information is necessary for many applications; there is a need for consistent, repeatable monitoring of vegetation properties and processes across the arid and semi-arid ecosystems (Langley *et al*. 2001; Nordberg and Evertson 2003).

Assessment of the state of vegetation and their dynamics generally relies on the use of optical remote sensing data. Although there are many advantages of using optical data for mapping and monitoring of vegetation, a major limitation is the availability of cloud-free scenes, which stimulates usage of other remote sensing data sources such as Synthetic Aperture Radar (SAR) (Mitchard *et al*., 2011; Carreiras *et al*., 2013). SAR is an advanced radar system that utilizes image processing techniques to synthesize a large virtual antenna, which provides much higher spatial resolution than using a real-aperture radar (Curlander and McDonough, 1991). It has great potential in monitoring and assessment of environmental changes. Moreover, SAR sensors, being active instruments with their own source of energy, can acquire images in all-weather conditions and with no difference between day and night (Lillesand *et al*., 2008).

Several studies have demonstrated the potential of SAR data for vegetation mapping and monitoring indicating that SAR-based methods can potentially outperform the optical data especially when cloud coverage restrain applications of optical satellite images (Almeida-Filho *et al*., 2009; Lang and McCarty, 2008; Hoekman *et al*., 2010). However, there is little published research on using SAR data for mapping and monitoring of vegetation in the drylands of Africa. This gap remains to be addressed to be able to produce more accurate spatially explicit information on vegetation dynamics in the arid and semi-arid environments based on remote sensing data to eventually support the sustainable management of vegetation in this environment.

To explore the potential of SAR data for mapping and monitoring of vegetation in the arid and semi-arid regions in Africa, we selected two main case studies. They represent the two main threats affecting the distribution of vegetation in this environment, particularly; climate change, and human disturbance. The first case study is located on the Red Sea coastline in Egypt and focused on mapping of mangroves ecosystems, which suffer from the heavy impacts of human disturbance, including over-grazing, over-cutting, and habitat destruction. The second case study is located in Eastern Cape Province, in South Africa, and focused on monitoring of grasslands, which suffer from the impact of drought and land degradation. The next sections provide more details about the two main vegetation types investigated in this thesis (mangroves and grasslands) including their distribution, importance, threats affecting their distribution, as well as the potential of using Earth Observation data for mapping and monitoring of these valuable ecosystems.

3.1. Mapping of Mangroves Extents on the Red Sea Coastline

Mangroves are the dominant vegetation for over 70% of tropical and subtropical coastlines of the world (Spalding *et al*., 1997). They are salt-tolerant evergreen forests, represent interphase between terrestrial and marine communities, and provide a habitat to both aquatic and terrestrial organisms (Feller *et al*., 2010). They may grow as trees or shrubs according to the climate, salinity of the water, topography and edaphic features of the area in which they exist. They have developed morphological, physiological and reproductive adaptations that have allowed the colonization of salty, waterlogged and frequently reducing soils, with rapid growth in areas subject to geomorphic changes (Hogarth, 1999). Mangrove species diversity and cover are fairly low. However, as mangroves are often the only forest ecosystem found along the coasts, they provide needed resources for local communities and a habitat for a wide range of wildlife and are important in the conservation of forest genetic resources (FAO, 2007).

Mangroves are among the most productive and biologically important ecosystems in the world. They have adapted to the harsh conditions of high salinity, warm air, and water temperatures, extreme tides, muddy sediment-laden waters, and oxygen-depleted soils, they have a thick, partially exposed network of aerial roots, penetrate deeply into the anaerobic mud, bringing oxygen to deeper portions of the root. They are highly productive ecosystems with a rich diversity of flora and fauna (Twilley and Rivera-Monroy, 2005). They support the conservation of biological diversity by providing habitats, nurseries, and nutrients for a number of animals and marine organisms, it creates a wide diversity of niches, which serve as suitable habitats for feeding, breeding, spawning and hatching of sedentary and migratory species (Barbier and Sathiratai, 2004).

They are considered of great ecological importance in shoreline stabilization, reduction of coastal erosion, sediment and nutrient retention, flood and flow control, and water quality (Giri *et al*., 2007; Gedan *et al*., 2011; Vo *et al*., 2013), besides their regular economic benefit through various forest products; providing firewood, charcoal, and timber (Walters *et al*., 2008). Mangroves also provide other socially and economically important materials such as fodder for livestock, medicines, and dyes. They are of great value to the local communities, and of considerable national and international importance. With the current acceleration of climate change, mangroves are being increasingly seen as carbon sinks and carbon stores (FAO, 2007).

Despite of their economic and ecological importance, mangrove ecosystems experience high yearly loss rates of 1-2% (Beaumont *et al*., 2011) and thus more than 50% have already disappeared in recent times (Feller *et al*., 2010). High population pressure in coastal areas has led to the conversion of many mangrove areas to other uses, and numerous case studies described these mangrove losses over time (FAO, 2007). Reasons for this loss are for example; over-exploitation, unsustainable wood extraction, conversion by urbanization, agriculture, aquaculture, and the pollution and alteration of the hydrological system (Hogarth, 1999; Lacerda, 2001). Mangroves along the Red Sea coastline in Egypt became threatened due to unmanaged human activities including over-cutting, over-grazing, and habitat destruction. A marked increase in traditional use is reported with a rapidly expanding human population and urban development along the coastal zone. This places other environmental services provided by mangroves, such as fish nursery areas, coastal protection, and bird roosting areas, at considerable risk.

There is a growing demand for integrated assessment to address the risk on mangroves ecosystems, especially in the context of climate change, human disturbance, and related threats to coastal ecosystems. Remote sensing is the most appropriate tool for mapping and assessing changes in mangrove ecosystems, due to its ability to capture high spatio-temporal variability over large geographical scales (Archibald and Scholes, 2007). It provides a fast, cost-effective, and efficient methods for mangroves mapping, it is particularly useful since many mangroves extents are located in remote areas, where field measurements are difficult, time-consuming, and expensive (Held *et al*., 2003). Remote sensing data offers many advantages in this respect and has been used in several studies for mangroves mapping (Green *et al*., 1996).

A variety of sensors and image processing methods have been used in the remote sensing of mangroves, such as SPOT (Système Pour l'Observation de la Terre) (Jensen *et al*., 1991; Rasolofoharinoro *et al*., 1998) and Landsat Thematic Mapper (TM) (Long and Skewes, 1996; Green *et al*., 1998). Since mangroves along the Red Sea coastline often grow in narrow small patches, high resolution remotely sensed data are required to capture the newly colonized individual stands or relatively small patches of mangroves stands that cannot be captured with medium spatial resolution satellite data *e.g.*, Landsat imagery (Neukermans *et al*., 2008).

Several studies have demonstrated the potential of SAR data for mapping of mangroves indicating that SAR-based methods can potentially outperform the optical remote sensing data (Almeida-Filho *et al*., 2009; Hoekman *et al*., 2010; Häme *et al*., 2009). SAR sensors are particularly used for woody structural mapping, because of their capacity to capture within-canopy properties (Le Toan *et al*., 2011; Sun *et al*., 2011; Santoro *et al*., 2007), and lack of sensitivity to cloudy conditions. L-band SAR provided by the Advanced Land Observing Satellite (ALOS) Phased Array L-band Synthetic Aperture Radar (PALSAR) has been proven to be the most effective in forests mapping and characterization (Mitchard *et al*., 2011; Carreiras *et al*., 2013; Naidoo *et al*., 2015) due to the high penetration of L-band into the canopy.

3.2. Monitoring of Grasslands in Eastern Cape Province

Grasslands cover more than 40% of the Earth's land surface and are widely used for livestock grazing and fodder production, thereby contributing to global food production in major ways (FAO, 2006). They are generally located in drier regions and experience high inter-annual variability in precipitation, which is a key driver of grasslands production and resource deterioration and recovery

(McKeon *et al*., 2004; Cobon *et al*., 2017). They are a major component of the natural vegetation in South Africa, it covers almost one-third of the country's land surface, with a biome comprising 295,233 km^2 of the central region of the country (Palmer and Ainslie, 2005).

The importance of grasslands lies in several factors, including its use in the production of livestock, and grasslands' role in maintaining biodiversity and soil erosion protection. Grasslands ecosystems support human, fauna and flora populations by providing numerous goods and services, such as the provision of forage for livestock, wildlife habitats, and biodiversity conservation (White *et al*., 2000). Additionally, grasslands are the largest terrestrial carbon sink after forests (Derner and Schuman, 2007), and play a vital role in regulating the global carbon cycle (Franzluebbers, 2010).

However, the ecosystem services provided by grasslands, they are facing several pressures due to the impact of climate change and unsustainable land management practices. At least 40% of the Grasslands Biome has been irreversibly modified, and nearly 60% of the remaining grassland areas are classified as threatened, this means that these ecosystems are losing vital aspects of their composition, structure, and functioning. This, in turn, influences their ability to deliver the essential services they provide (Palmer and Ainslie, 2005).

Drought has been one of the major factors influencing vegetation dynamics in grasslands (Cook *et al*., 2007) with substantial social and economic consequences (Wilhite and Buchanan-Smith, 2005). The two relevant droughts, influencing grasslands, are meteorological drought, which is a consequence of a reduction of precipitation, and agricultural drought, which refers to a shortage of the available water for plant growth (Wilhite, 2000; Keyantash and Dracup, 2002). Severe drought can limit grasslands production (Knapp and Smith, 2001), alter nutrient cycling (Evans and Burke, 2013), and increase wildfire risk, and susceptibility to invasive plant species (Abatzoglou and Kolden, 2011).

There is a critical need to understand how drought affects grasslands, in part because drought severity and drought-associated grasslands disturbances are expected to increase with the climatic change that might lead to a potential degradation. On the other hand, spatially explicit data on the impact of drought on grassland can provide vital information for various applications such as biodiversity conservation, and monitoring land use intensification in areas with high conservation value (Wessels *et al*. 2007; Paudel and Andersen, 2010).

Remote sensing offers a unique perspective for drought monitoring that complements the *in situ*–based climate data traditionally used for this application. Vegetation estimates from MODIS and AVHRR have been extensively used for studying vegetation dynamics (Piñeiro *et al*., 2006), but complex spatial patterns that result from the interaction of disturbances with soils, topography, and vegetation are often undetectable with moderate-low resolution sensors (0.25–1 km). Satellite-based indices such as the Normalized Difference Vegetation Index (NDVI) became increasingly used for various environmental monitoring applications including drought monitoring (Kogan, 1997; Peters *et al*., 2002).

SAR data have been used to complement the cloud problems of optical sensors because SAR data are not influenced by weather conditions (Lang and McCarty, 2008). Due to their sensitivity to dielectric and structural land surface features, SAR data have shown their potential to derive spatial information from land surfaces, especially radar backscatter from polarimetric SAR systems allows a detailed description of different vegetation and soil properties (Morandeira *et al*., 2016).

4. Research Objectives

The main objective of this study focuses on exploring the potential of spaceborne SAR data for enhancing vegetation mapping and monitoring in the arid and semi-arid regions of Africa. The specific objectives are:

(a) Exploring the potential of ALOS PALSAR data for mapping of mangroves extents on the Red Sea coastline (*Chapter 4*).

(b) Assessing the impact of drought on grasslands in Eastern Cape Province using multi-temporal SAR data of Sentinel-1 (*Chapter 5*).

(c) Evaluating the potential of Interferometric SAR (InSAR) coherence of Sentinel-1 for grasslands monitoring in Eastern Cape Province (*Chapter 6*).

5. Research Questions

The research objectives of this thesis can be formulated into three main questions, each question will be investigated in a separate chapter:

(a) How precisely SAR data could be used for mapping of mangroves extent on the Red Sea coastline? and what is the applicability of integrating SAR data with optical data for mangroves mapping?

(b) What is the potential of using multi-temporal SAR data of Sentinel-1 for assessing the impact of drought on communal and commercial grasslands in Eastern Cape Province?

(c) Could the InSAR coherence derived from Sentinel-1 SAR data be used for monitoring of grasslands under drought and non-drought conditions?

6. Thesis outlines

This thesis is structured in two main parts. *The first part* (chapters 1, 2 & 3) includes an introduction into the thesis, principles of SAR systems, and the study area description. **Chapter 2** provides an overview of the principles of SAR systems and the properties of SAR data. **Chapter 3** provides an overview of the study area and the different data sources used in this thesis. *The second part* (chapters 4, 5 & 6) consists of three publications concerning the applications of Spaceborne SAR remote sensing in mapping and monitoring of vegetation dynamics in the arid and semi-arid environments. **Chapter 4** focuses on using SAR data of ALOS/PALSAR integrated with high resolution optical data for mapping of mangroves extents on the Red Sea coastline in Egypt. **Chapter 5** investigates the use of multi-temporal SAR data of Sentinel-1 for assessing and detecting the impact of drought on grasslands in Eastern Cape Province in South Africa. **Chapter 6** explores the potential of using Sentinel-1 InSAR coherence for grasslands monitoring in Eastern Cape Province. Finally, **Chapter 7** outlines the conclusions of the work and the outlook for the future.

Chapter 2

Principles of SAR Systems

This chapter provides an overview of the principles of SAR systems, including the concepts necessary for understanding the operating principles of SAR, the properties of SAR images, SAR Polarimetry, and scattering mechanisms of SAR data.

1. Principles of SAR Systems

1.1. Spaceborne RADAR Remote Sensing

Remote sensing is divided into passive and active, passive sensors record the emitted or reflected radiation from objects on the earth's surface. In most cases, the source of radiation is the sun. Optical sensors and passive microwave sensors are examples of passive sensors. They capture the visible, near-infrared, short wave infrared and thermal infrared wavelengths. Active sensors, on the other hand, transmit microwave pulses from their antenna to the ground and record the backscatter such as laser light (LIDAR), or radio waves RADAR (Radio Detection and Ranging) (Henderson and Lewis, 2008).

Radar is an active sensor operates in the microwave portion of the electromagnetic spectrum (Figure 2.1). Unlike optical waves, microwaves are not affected by clouds; they can penetrate vegetation canopies to some degree. They are sensitive to moisture and rainfall. Indeed, they are affected by the dielectric properties of the surface that change with the moisture conditions, they are also affected by imaging geometry, topography, and surface roughness of the target (Henderson and Lewis, 2008; Lillesand *et al*., 2008). Radar systems transmit and receive signals in the wavelength range of 1 cm to 1 m, equivalent to a frequency of between 300 MHz and 30 GHz (Campbell, 2002, Figure 2.2).

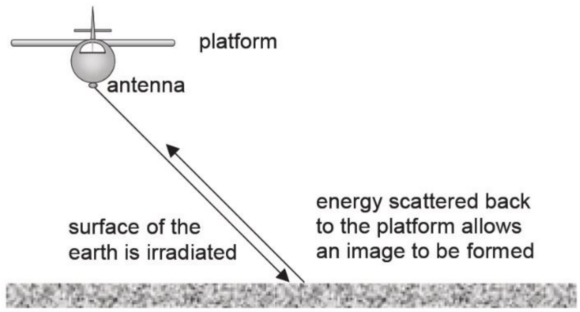

Figure 2.1. The fundamental arrangement for active microwave remote sensing (Richards, 2009).

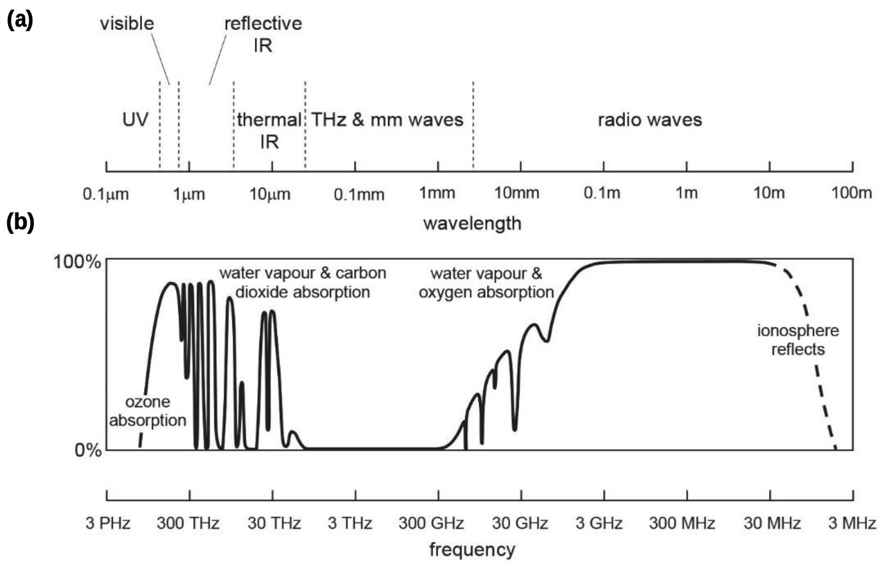

Figure 2.2. (a) The electromagnetic spectrum, and (b) the indicative transmittance of the atmosphere on a path between space and the Earth (Richards, 2009).

1.2. Synthetic Aperture Radar (SAR)

Synthetic Aperture Radar (SAR) is a microwave imaging system. It is actively illuminating the ground with electromagnetic pulses with a microwave frequency (0.3–300 GHz) (Curlander and McDonough, 1991). SAR sensors are side-looking systems, with a long-track flight path referred to as the azimuth and a cross-track (right angle to flight direction) described as the range (Lillesand *et* *al*., 2008). SAR uses the forward motion of the sensor to simulate a long antenna by integrating several looks of the same scene. SAR transmitter sends regular pulses of microwave energy to the ground. The radar pulse interacts with the Earth's surface and scattered in all directions, with some energy reflected back toward the radar's antenna known as backscatter. The backscattered energy received by the antenna is dependent on the dielectric properties of the ground, its surface roughness, and local incidence angle (Campbell, 2002, Figure 2.3).

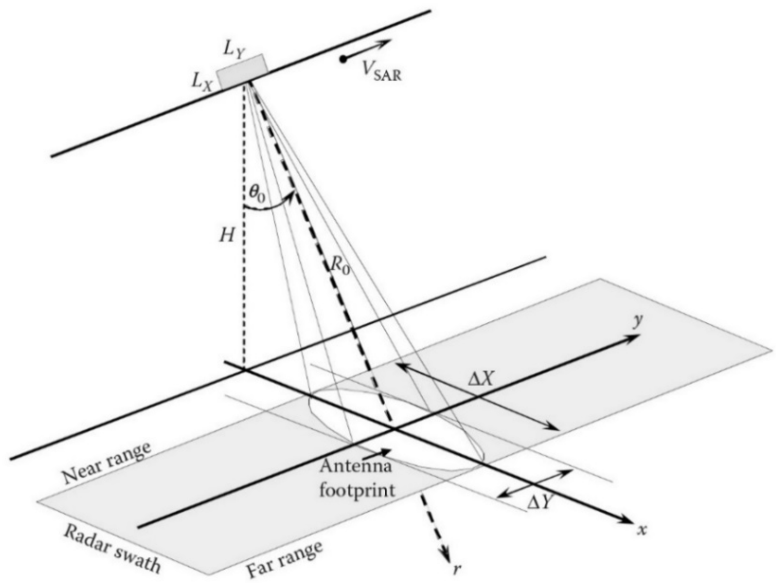

Figure 2.3. SAR imaging geometry (Richards, 2009)

1.3. SAR System Parameters

Spaceborne SAR data have been acquired since the late 1970s by several satellites using various systems and acquisition parameters. This section provides a brief introduction to some of the different parameters of SAR systems.

1.3.1. Frequency

Two of the key parameters that determine the interaction of the radar signal with vegetation are the radar wavelength or frequency and polarization. Most SAR satellites have operated in three frequencies: X-band, C-band, and L-band. The shorter wavelength X-band signal interacts mainly with upper sections of the vegetation, the intermediate C-band signal penetrates further and can penetrate the entire canopy under some circumstances, and the L-band signal can penetrate throughout the vegetation and interact with the surface beneath the vegetation (Lillesand *et al*., 2008, Figure 2.4). SAR instruments considered in this thesis are ALOS PALSAR, which uses L-band, and Sentinel-1, which uses C-band. Table (2.1) shows the different spaceborne SAR sensors with different frequencies and polarizations.

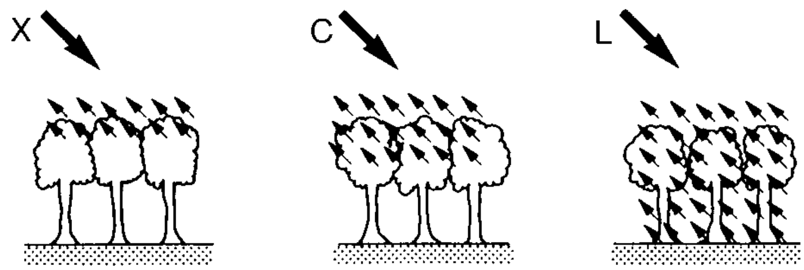

Figure 2.4. Interaction of L-band and C-band SAR data with vegetation.

Table 2.1. Spaceborne SAR sensors, modified after Wdowinski and Eriksson (2009).

Satellite	Frequency and Polarization	Agency	Time
ERS-1	C-band, VV pol	ESA	1992-1996
ERS-2 (SAR)	C-band, VV pol	ESA	1996-2011
JERS-1	L-band, HH pol	JAXA	1992-1998
Rasarsat-1	C-band, HH pol	CSA	1995-2013
Space shuttle (SRTM)	X-, C-, and L-band	NASA	2000
Envisat (ASAR)	C-band, dual pol	ESA	2002-2012
ALOS (PALSAR)	L-band, dual pol, quad pol	JAXA	2006-2011
Radarsat-2	C-band, quad pol	CSA	2007-present
TerraSAR-X/TanDEM-X	X-band, dual pol, quad pol	DLR	2007-present
COSMO-SkyMed	X-band, dual pol	ISA	2007-present
ALOS (PALSAR-2)	L-band, dual pol, quad pol	JAXA	2014-present
Sentinel-1A	C-band, dual pol	ESA	2014-present
Sentinel-1B	C-band, dual pol	ESA	2016-present

Sensitivity to surface roughness is higher in longer wavelengths (lower frequencies) as compared to shorter wavelengths (higher frequencies). Surface roughness in SAR imaging depends on the wavelength of the microwave. A land surface can appear smooth to a long-wavelength radar, while the same surface appears rough at a short wavelength. If a SAR, with an L-band, illuminates a surface with a roughness of the order of 5 cm, the surface will appear dark because of low backscatter. In contrast, in an X-band, the same surface will appear bright because of high backscatter (Mattia *et al.*, 1997, Figure 2.5).

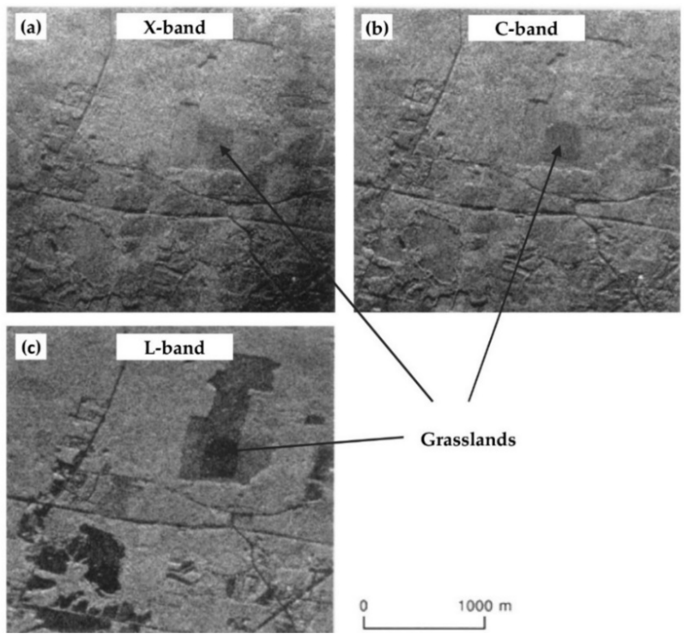

Figure 2.5. Variation in microwave backscatter from a rough surface as a function of wavelength. As the wavelength gets longer, the backscattering decrease.

1.3.2. Polarization

Polarization refers to the orientation of the electric field vector of the transmitted beam with respect to the horizontal direction. If the beam is horizontally polarized, the vector oscillates along a direction parallel to the horizontal direction. On the other hand, if the oscillation of the electric field vector is along a direction perpendicular to the horizontal direction, the beam is vertically polarized (Campbell, 2002, Figure 2.6).

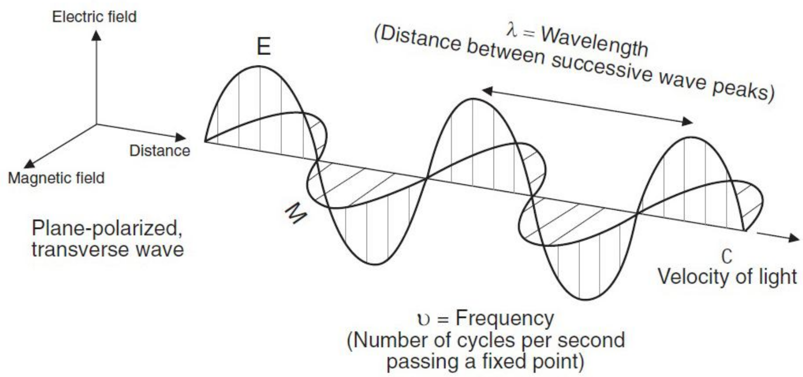

Figure 2.6. Electromagnetic wave (adapted from Lillesand and Kiefer 1999).

Transmitting pulses from a SAR satellite can be polarized horizontally (H) or vertically (V) and can also be received in either H or V or with a combination of HH, VV, HV or VH. The first generation of SAR satellites operated in a single polarization mode, such as HH (horizontal transmitted and horizontal received) by RSAT-1 or VV (vertical transmitted and vertical received) by ERS-1/2. The second generation of SAR satellites, such as Envisat and ALOS, already operated with dual-polarization modes, such as HH + HV (horizontally transmitted and two types of receptions, horizontal and vertical) or VV + VH. The composition of polarization provides information on the form and orientation of scattering on the target surface. Multiple polarizations help to distinguish the physical structure of the scattering surface (Campbell, 2002; Lee and Pottier, 2009).

1.3.3. Backscattering

Radar waves interact differently with vegetation, soil, water, and man-made objects such as buildings and roads because the backscatter is affected by the surface properties of the objects. For a smooth surface such as water or a road, most of the incident energy is reflected away from the radar system resulting in a very low return signal. In contrast, rough surfaces will scatter the emitted energy in all directions and return a significant portion back to the antenna. In general, vegetation is usually moderately rough with most radar wavelengths (Richards, 2009, Figure 2.7).

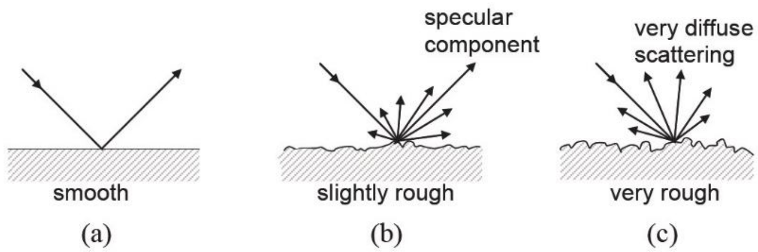

Figure 2.7. Diffuse surface scattering increases as roughness increases (Richards, 2009).

Backscatter is also sensitive to the dielectric constant, which is a measure of the electrical properties of surface materials (Lillesand *et al*., 2008). Backscattering coefficient is measured in decibel (dB) units ranging from +5 dB for very bright objects to –40 dB for very dark surfaces. Vegetation can be a complicating factor as radar interaction depends strongly on the frequency and polarization of the microwave energy as well as the structure of the canopy (Lillesand *et al*., 2008). Backscatter is also affected by the incidence angle, it is the angle between the incidence radar signal and the direction perpendicular to the ground surface that the signal strikes. For angles less than about 25 degree smoother surfaces have greater backscatter than rougher surfaces (Campbell, 2002; Lillesand *et al*., 2008, Figure 2.8).

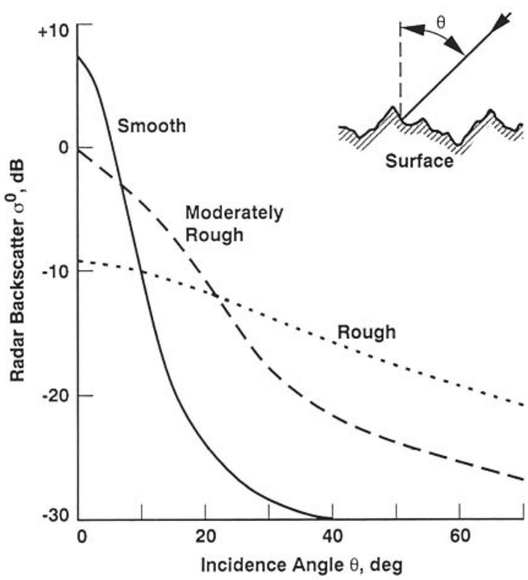

Figure 2.8. Radar backscatter as a function of incidence angle for representative surfaces.

1.3.4. Speckle Filtering

In all types of coherence data including SAR imagery, there is a random constructive and destructive interference scattered by the target within one resolution pixel creating noise-like granulation called speckle. Speckle is a noise-like scattering phenomenon embedded in the image itself possibly due to insufficient resolution of the sensor to resolve individual scatterers within an imaged pixel. In most situations, speckle makes the SAR image segmentation and classification difficult (Woodhouse, 2006).

The presence of speckle in SAR data reduces the visibility of the imagery hence decreasing the discrimination of the target. To minimize the speckle effect in SAR imagery, incoherent averaging is performed. There are two main approaches for speckle filtering and enhancement; using the Doppler phenomenon where several parts often called 'looks' are averaged incoherently 'multi-looking', the second method involves averaging the neighboring pixels using a windowing size function (Lillesand *et al*., 2008, Figure 2.9).

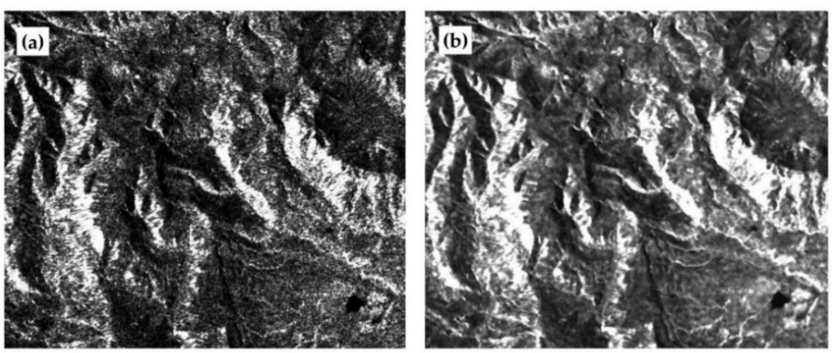

Figure 2.9. (a) speckled image, and (b) speckle filtered image.

1.4. SAR Scattering Mechanisms

Figure (2.10) shows the three main scattering mechanisms, which explain the interactions of SAR signals with the surface and vegetation; surface scattering, volume scattering and double-bounce scattering (Freeman and Durden, 1998). Surface scattering is influenced by the surface roughness of the surface in relation to the SAR frequency. Volume scattering is the interaction of the SAR signal with vegetation canopy. This is especially prevalent in dense vegetation areas. Double-bounce scattering is where the SAR signal interacts with objects orthogonal to the surface, such as the vertical stems of trees or the sides of buildings (Richards, 2009).

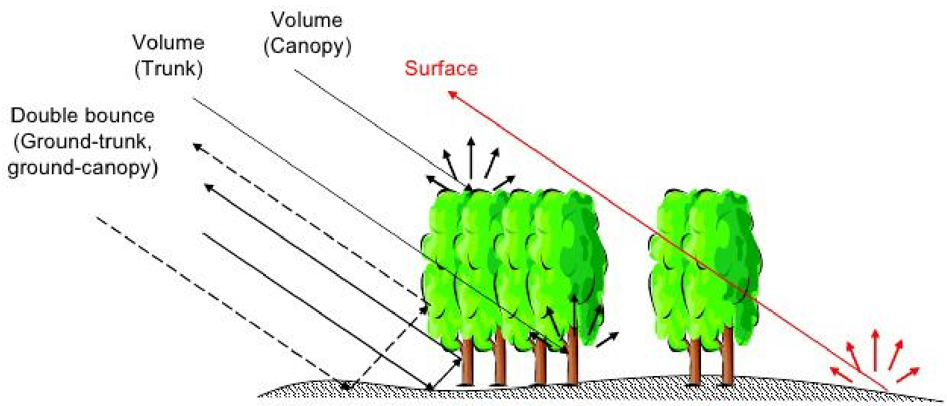

Figure 2.10. Different scattering mechanisms including; surface scattering, volume scattering, and double-bounce scattering (Watson *et al*., 2000).

SAR signals returned are often a combination of the scattering mechanisms. In a forest, there are SAR backscattering returned from the canopy, through volume scattering, and double-bounce from the ground and the stems of the trees. For vegetation with smaller stems, such as shrubs or tall grass, a combination of volume scattering and surface scattering is returned. However, since the scattering mechanisms are frequency-dependent, different scattering interactions can be separated to a large degree, C-band interacts largely with the canopy, through volume scattering, whereas longer wavelengths such as L-band will penetrate the canopy, and return scattering from the stems and large branches through double-bounce scattering (Richards, 2009).

Chapter 3

Study Area and Data Sources

This chapter provides an overview of the study area, the selected study locations with different study sites and different vegetation types. The chapter concludes with the different data sources used in the current study, including SAR and optical sensors with different characteristics.

1. Study Area Description

To achieve the objectives of the current study, two case studies were selected at different geographical locations in the arid and semi-arid environments in Africa, with different climatic conditions, vegetation structure, as well as different land use patterns; the first case study is located on the Red Sea coastline in Egypt (site A). The study focused on mapping of mangroves extents on the Red Sea coastline using ALOS PALSAR data integrated with high resolution optical data of RapidEye. The second case study is located in Eastern Cape Province in South Africa (site B). The study focused on using multi-temporal SAR data of Sentinel-1 intensities and InSAR coherence for assessing and detecting the impact of drought on grasslands.

1.1. Site (A) on the Red Sea Coastline

Site (A) is located on the Red Sea coastline in Egypt. The Red Sea is a semi-enclosed elongated and narrow-shaped tropical basin (Figure 3.1). It extends between the Mediterranean Sea, to the northwest, and the Indian Ocean, to the southeast. At the northern end, it separates into the Gulf of Suez and the Gulf of Aqaba and connected to the Mediterranean Sea through the Suez Canal. At the southern end, it is connected to the Gulf of Aden, and the outer Indian Ocean through the Strait of Bab-el-Mandab. The Red Sea covers a wide span of latitudes, from 12°N to 30°N, and longitudes, from 32°E to 44°E. The basin extends from north to south over a distance of approximately 1,900 km. Its average width from east to west is 280 km, with a maximum of 306 km, in the south, and a minimum of 26 km, at Bab-el-Mandeb Strait. The basin has a total area of about 440,000 km^2, and more than 4,000 km of coastlines (Head, 1987, Figure 3.1).

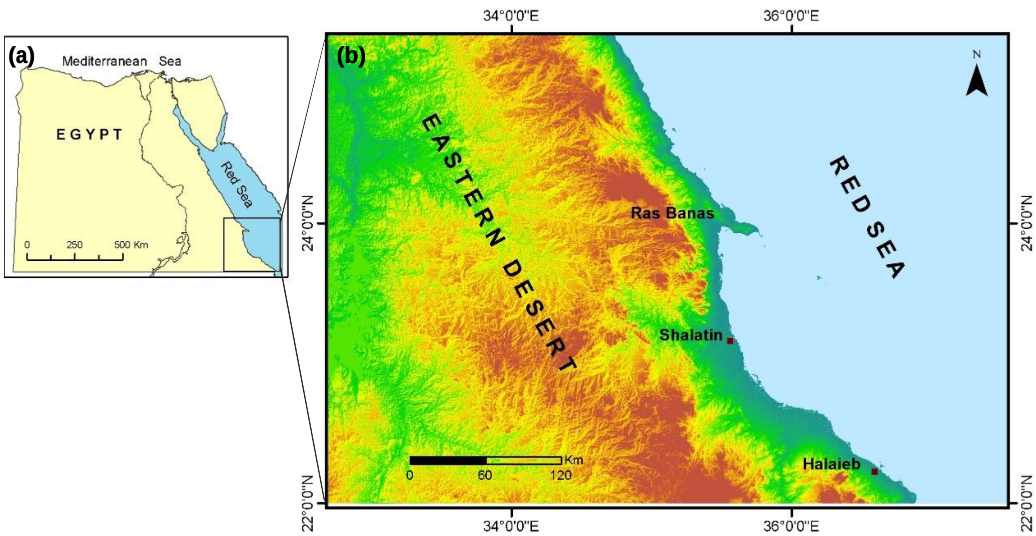

Figure 3.1. Map showing the geographical location of the study area; (a) reference map of Egypt, and (b) The study area on the Red Sea coastline overlaid on SRTM digital elevation model.

The study site is also located in the Eastern Desert (ED) of Egypt. ED occupies the area extending from the Nile Valley eastward to the Red Sea, about 223,000 km^2. It is higher than the Western Desert as it consists essentially of high, rugged mountains running parallel to and at a relatively short distance from the Red Sea coast (Abu Al-Izz, 1971). The mountains of the Eastern Desert are of two types: igneous and limestone. The igneous mountains extend southward from Lat. 28°N to the north of the igneous mountains are the extensive limestone mountains (Zahran and Willis, 2009). The Red Sea coastline varies geomorphologically from a rugged coastline with marine terraces and rocky shores, to coastal sabkhas, alluvial plains, and wadis. There are a large number of dry riverbeds, alluvial fans, and estuaries extending along the coast.

Desert or semi-desert areas, with no major freshwater inflow, surround the Red Sea. Given the absence of rivers and permanent streams, occasional runoff is due only to wadis. In this arid region, extremely high temperatures characterize the weather, particularly in summer, increasing from the northern to the southern area. Warm to very warm surface water temperatures in all parts of the Red Sea basin were recorded and vary seasonally between 22 and 32 °C. During the summer, the temperature averages 26 °C in the north and 30 °C in the south, with only about 2-4 °C variation during the winter, averaging 23 °C (Maillard and Soliman, 1986; Sheppard *et al.*, 1992).

Mangrove communities in Egypt represent the northern latitudinal limits of the Endo-Pacific East African mangroves, and owing to its extreme environmental conditions (high salinity, low rainfall, and extreme temperatures), the trees are generally stunted, rarely exceeding five meters in height (FAO, 2007). They are found scattered along the Red Sea coastline, and the Gulf of Aqaba coastline, their usual habitat is shallow water, such as lagoons, bays, coral or sand bars parallel to the shore. Two species only of mangroves were recorded in Egypt; *Avicennia marina* (Forssk.) Vierh., and *Rhizophora mucronata*. Mangrove vegetation on the Red Sea coastline is usually dominated by *A. marina* (Figure 3.2); it is a tolerant species to relatively high salinity, low rainfall and temperature conditions (Zahran and Willis, 2009), while *R. mucronata* occurs at several southern locations on the Red Sea coastline; south of 25°N, and close to the Sudanese border, it requires more humid conditions and is less tolerant to high salinity when compared with *A. marina* (El-Gazzar, 1995; Galal, 1999).

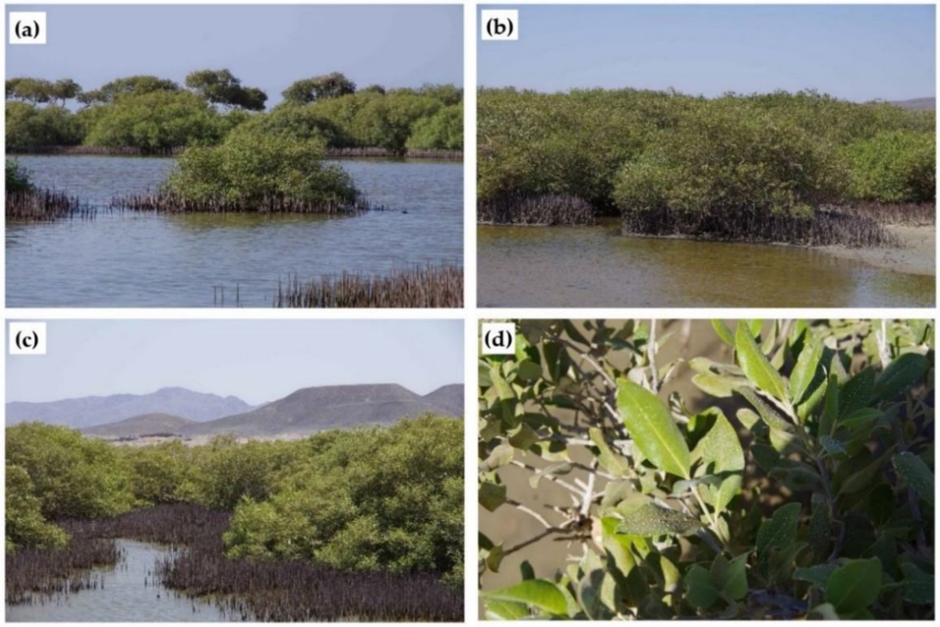

Figure 3.2. Field photographs showing; (a) the mangroves ecosystem on the Red Sea coastline, (b) the surrounding habitats, (c) aerial roots of the mangroves, and (d) the accumulation of salts on the leaves of *Avicennia marina*.

1.2. Site (B) in Eastern Cape Province

The Eastern Cape Province is one of the nine provinces in South Africa, it covers an area of approximately 169,000 km^2. It is the second-largest province in South Africa after the Northern Cape and located in the southeast of South Africa. It borders KwaZulu Natal, Free State and Lesotho to the north, and the Northern Cape and Western Cape to the west. The Indian Ocean forms the southern and eastern border of the Eastern Cape Province (Jordaan, 2017).

Bisho is the capital of Eastern Cape Province. It is located between the port cities of East London and Port Elizabeth, which are the largest cities in the province. They are also the main centers of industry and trade in Eastern Cape. The province consists of one metropolitan municipality, six district municipalities, and 38 local municipalities. The population is at 12.7 million of which they most live in Port Elizabeth, East London and the Northern Municipality of O.R. Tambo. A total of 60% of the population lives in rural areas, where some areas lack sufficient access to infrastructure and education (Jordaan, 2017).

Eastern Cape is characterized by topographic and climatic complexity and diversity, with very steep and complex environmental gradients leading to a rich mixture of floristic elements. All of South Africa's biomes occur in Eastern Cape, except for Desert. The Grassland, dwarf-shrub vegetation (Nama Karoo), Thicket, and Savanna biomes are the most extensive. The mountainous region in the north of the province forms part of the Great Escarpment Mountains. Further south the Cape Folded Mountains start between East London and Port Elizabeth and continue westwards into the Western Cape. The coastal area north of East London is characterized by many short, deeply incised rivers flowing parallel to each other out to sea (Hoare and Bredenkamp, 2001).

The climate range in Eastern Cape varies from mild warm temperatures to sub-tropical in the coast. Droughts can occur throughout the year, but grasslands are particularly vulnerable to droughts in the summer. The climatic conditions of the coastal areas lie between the subtropical conditions prevalent in KwaZulu-Natal, and the Mediterranean climate of the Western Cape. The inland area is bisected by the great escarpment resulting in the southern reaches defined by a series of rivers and corresponding wetland fauna and flora, and while the northern areas are those of the altitudinous plains of the Plateau and Great Karoo. The precipitation regime is characterized by large variability at various time scales from intra-seasonal, through inter-annual to decadal and multi-decadal (Kane, 2009). We focused in this study on Sakhisizwe municipality (2,355 km^2); it is located in the Chris Hani District in Eastern Cape Province. The main two towns in Sakhisizwe municipality are Cala and Elliot (Figure 3.3).

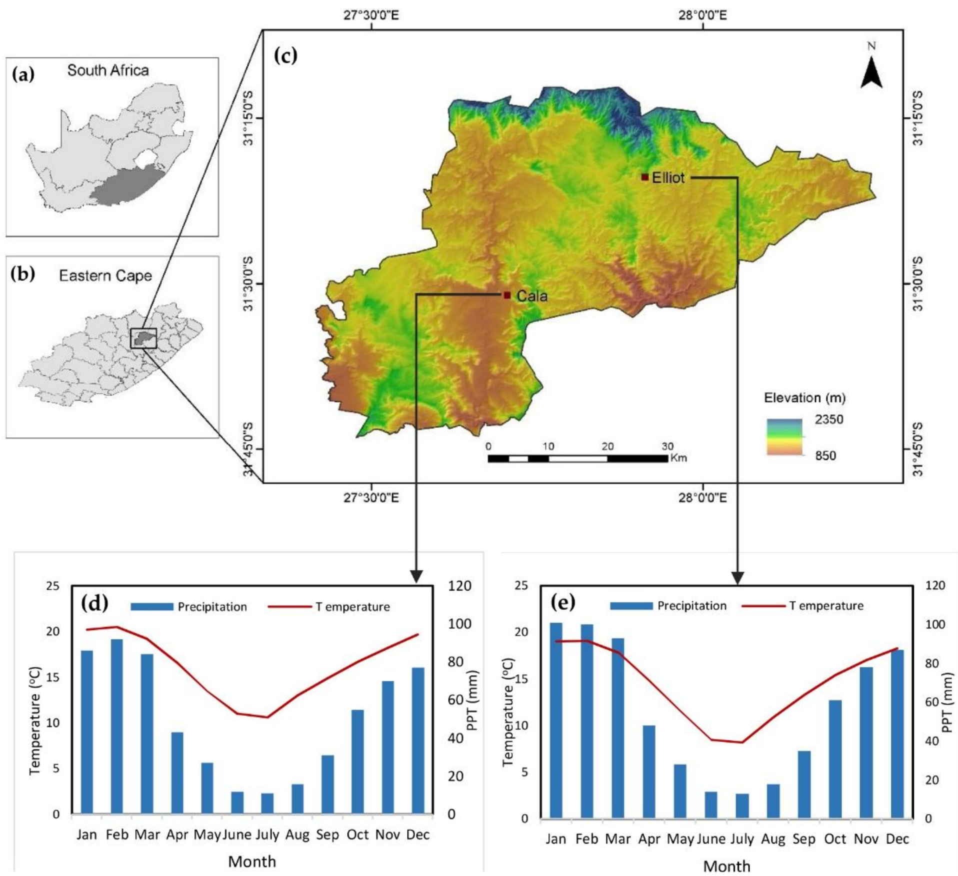

Figure 3.3. Map showing the location of the study area; (a) South Africa, (b) Eastern Cape Province, (c) Sakhisizwe municipality overlaid on SRTM digital elevation model, and the mean temperature and total precipitation in the two main towns in the municipality, (d) Cala, and (e) Elliot.

Grasslands are a major component of the natural vegetation in South Africa, it covers almost one-third of the country's land surface, with the biome comprising 295,233 km^2 of the central region of the country. They extend across the boundaries of seven provinces, spanning a complex array of socio-economic situations and land use contexts. The interface between grasslands and other biomes contributes substantially to their floristic and faunal diversity and to the important role they play in the agricultural economy (Palmer and Ainslie, 2005).

The importance of grasslands lies in several factors, including its use in the production of livestock, and grasslands' role in maintaining biodiversity and soil erosion protection. Grasslands ecosystems support human, fauna and flora populations by providing numerous goods and services, such as the provision of forage for livestock, wildlife habitats, and biodiversity conservation (White *et al*., 2000, Figure 3.4).

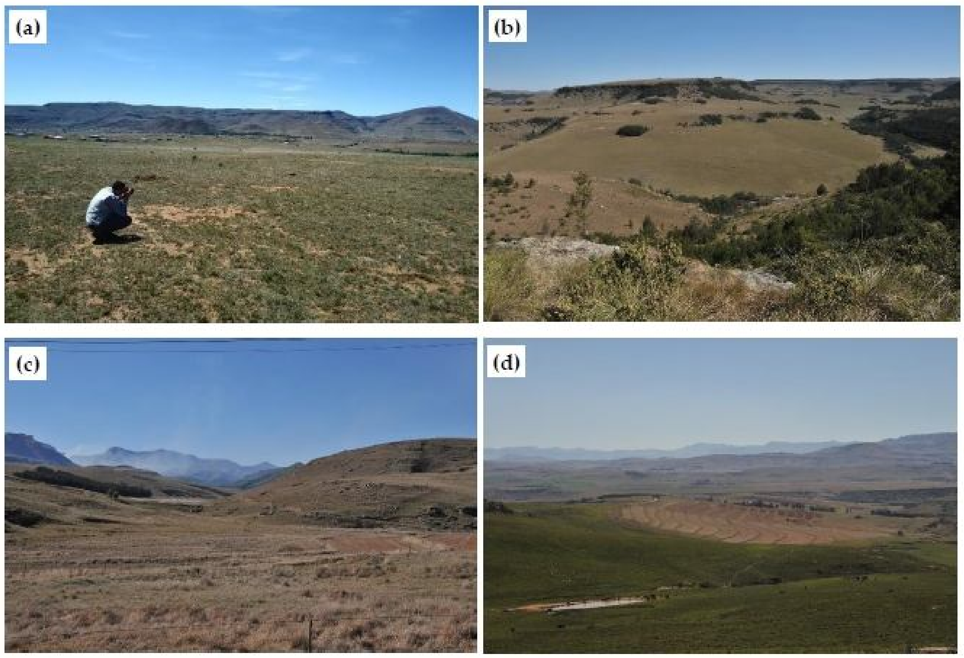

Figure 3.4. Field photographs in the study area showing; (a) different landforms, (b) different terrain and topography, (c) grassland fields, and (d) the surrounding habitats.

2. Data Sources

2.1. SAR Remote Sensing Data

Two types of SAR data were used in this thesis. The first dataset belongs to ALOS PALSAR data with L-band, and the second dataset belongs to Sentinel-1 SAR data with C-band. A brief introduction to each of them is presented in this section. Details of SAR data processing can be found in the next chapters.

2.1.1. ALOS PALSAR Data

The Phased Array L-band Synthetic Aperture Radar (PALSAR) is an active microwave sensor aboard the Advanced Land Observing Satellite (ALOS) and operates at L-band (~23.6 cm wavelength). It was launched in January 2006 and came to the end of its life after five years in May 2011 (JAXA, 2011). PALSAR was operated in five different observation modes: Fine Beam Single-polarization (FBS), Fine Beam Dual-polarization (FBD), Polarimetric mode (POL), ScanSAR mode, and Direct Transmission (DT) mode (Rosenqvist *et al*., 2007, Figure 3.5).

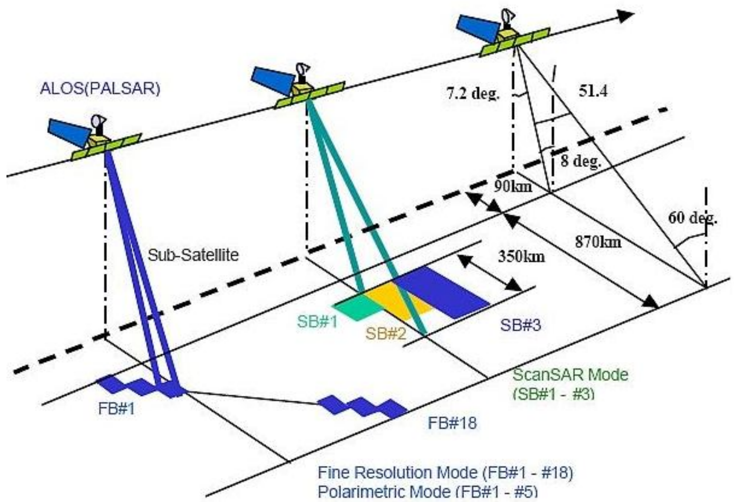

Figure 3.5. Different modes of ALOS PALSAR.

Data used in this thesis was acquired in FBD mode (HH and HV), and FBS mode (HH), in an ascending orbit, with an off-nadir angle of 34.3°. Data were acquired in a slant range single-look complex format (SLC, L1.1). Each scene covers an area of approximately 60 × 70 km. Table (3.1) provides the specifications and technical details of the ALOS PALSAR dataset.

Table 3.1. ALOS PALSAR mission specifications.

Mission characteristic	Information
Duration	2006 - 2011
Altitude	691.685 km
Repeat cycle	46 days
Polarization	FBS (HH), FBD (HH/HV) POL (HH/HV/VH/VV)
Incidence angle	FBS and FBD (34.3^{o}) POL (21.5^{o})
Swath width	30 km
Pass direction	Ascending
Application	Biophysical parameters retrieval

2.1.2. Sentinel-1 SAR Data

Sentinel-1 is an imaging radar mission providing continuous all-weather, day-and-night imagery at C-band. It provides high reliability, improved revisit time, geographical coverage, and rapid data dissemination to support operational applications in the priority areas of land surface monitoring. It carries a single C-band synthetic aperture radar instrument (5.405 GHz), and composed of a constellation of two satellites (S-1A and S-1B) to assure data continuity provided by the ERS-1/2 and ENVISAT satellites. Sentinel-1 operates in four image modes with various observation strategies, swath widths, and spatial resolutions; the Strip Map mode (SM), Interferometric Wide swath mode (IW), Extra Wide swath mode (EW), and Wave swath mode (WV) (Torres *et al*., 2012, Figure 3.6).

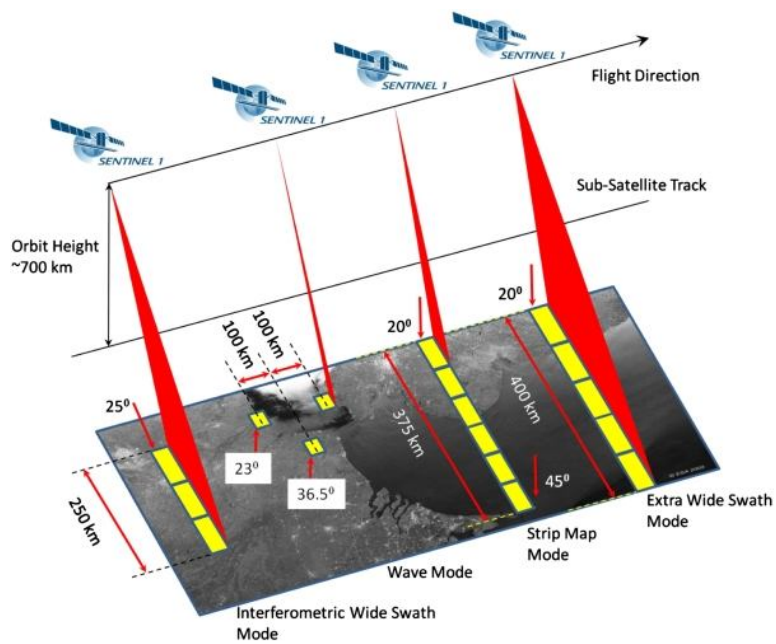

Figure 3.6. Different modes of Sentinel-1.

Interferometric Wide swath mode (IW) is the main acquisition mode over land and satisfies the majority of service requirements. It acquires data with 250 km swath at 5 x 20 m spatial resolution and captures three sub-swaths using Terrain Observation with Progressive Scans SAR (TOPSAR) technique. IW SLC products contain one image per sub-swath and one per polarization channel, for a total of three (single-polarization) or six (dual-polarization) images in an IW product. Each sub-swath image consists of a series of bursts, where each burst has been processed as a separate image. S1 data used in this thesis were acquired in the IW mode, SLC format, and dual-polarization VV/VH. Table (3.2) provides the specifications and technical details of Sentinel-1 SAR data.

Table 3.2. Sentinel-1 SAR IW specifications.

Mission characteristic	Information
Centre Frequency	5.405 GHz
Polarization	Dual HH+HV, VV+VH, Single HH, VV
Repeat cycle	12 days with one satellite or 6 days with two satellites
Swath width	250 km
Incidence angle range	29.1°- 46.0°
Sub-swaths	3
Pass direction	Ascending and Descending

2.2. Optical Remote Sensing Data

In addition to SAR data, two main optical remote sensing datasets were used in this thesis; RapidEye (RE) with high resolution data, and Landsat-8 Operational Land Imager (OLI). RapidEye data were used in the first case study, integrated with ALOS PALSAR data for mapping of mangroves extents on the Red Sea coastline, while Landsat-8 were used in the second case study, combined with Sentinel-1 SAR data for monitoring of grasslands in Eastern Cape Province. This section provides more details about these two optical datasets.

RapidEye (RE) is a commercial optical Earth observation mission that consists of a constellation of five satellites (Tyc *et al*., 2005). The sensors deliver high spatial resolution imagery with a ground sampling distance of 6.5 m at nadir. RapidEye data (3A product) were acquired from the RapidEye Science Archive (RESA) of the German Aerospace Centre (DLR). Table (3.3) provides the specifications and technical details of RapidEye data.

Table 3.3. RapidEye Satellite Sensor Specifications.

Mission characteristic	Information
Number of satellites	5
Orbit altitude	630 Km sun-synchronous orbit
Sensor type	Multi-spectral imager
spectral bands	Wavelength (nm)
Ground sampling distance (nadir)	6.5 m
Pixel size (ortho-rectified)	5 m
Swath width	77 km
Revisit time	Daily (off-nadir)/5.5 days (at nadir)

Landsat-8 was launched on February 11, 2013, as a backup of Landsat-7 to ensure the continuity of data beyond the duration of the Landsat-7 mission. Initially named as Landsat Data Continuity Mission (LDCM), it was renamed later as Landsat-8. It has two sensors, namely Operational Land Imager (OLI) and thermal infrared sensor (TIS) onboard. Landsat-8 OLI data were used in this thesis. Landsat provides the longest continuous archive of optical satellite data for land surface mapping and monitoring. The launch of the Landsat-8, in particular, has brought new opportunities and a platform for continuity in optical remote sensing. Landsat-8 surface reflectance was used to calculate the Normalized Difference Vegetation Index (NDVI) (Tucker, 1979). Vegetation indices are less sensitive to image-to-image noise, viewing geometry, and atmospheric attenuation, making them particularly advantageous over reflectance products when using large area mosaics covering scenes spread over multiple paths, rows, and dates (Vermote *et al*., 2016).

2.3. Ancillary data

In addition to remote sensing data, other ancillary data were used in this thesis including; field data, climatic data, land cover maps, and digital elevation model (DEM). Field data were obtained through field expeditions carried out in the two main study areas; (a) on the Red Sea coastline for collecting data for the mangroves case study, and (b) in Eastern Cape Province, for collecting data for the grasslands case study, and for validation of the remote sensing data analysis.

During these expeditions, field measurements including; ground truth data with a corresponding description of the study sites were collected. In addition, identifying the main geographical features in the study area, as well as vegetation patterns, and species distribution. Fieldwork also included identifying the main classes within the mangroves ecosystem in the first case study, and identifying the different tenure systems in grasslands; communal and commercial grasslands in the second case study.

Meteorological data covering the main study locations with communal and commercial grasslands, and the surrounded area in Eastern Cape Province, were obtained from the South African Weather Service Organization. In addition, precipitation information based on the Climate Hazards Group Infrared Precipitation with Station (CHIRPS) data were used in the current study. The CHIRPS product provides daily precipitation data for the quasi-global coverage of 50°N-50°S from 1981 to present (Funk *et al*., 2015). SRTM DEM data was used in the first case study to identify the potential mangrove areas based on the elevation. Land cover information covering the study area in the second case study was obtained based on the South African National Land-cover dataset for South Africa produced by GEOTERRAIMAGE (Graw *et al*., 2017).

Chapter 4

Mapping Mangroves Extents

*This chapter has been published as **Abdel-Hamid, A.**, Dubovyk, O., Abou El-Magd, I., and Menz, G. 2018. Mapping mangroves extents on the Red Sea coastline in Egypt using polarimetric SAR and high resolution optical remote sensing data. Sustainability, 10, 646.*

ABSTRACT

Mangroves ecosystems dominate the coastal wetlands of tropical and subtropical regions throughout the world. They are among the most productive forest ecosystems. They provide various ecological and economic ecosystem services. Despite of their economic and ecological importance, mangroves experience high yearly loss rates. There is a growing demand for mapping and assessing changes in mangroves extents especially in the context of climate change, land use change, and related threats to coastal ecosystems. The main objective of this study is to develop an approach for mapping of mangroves extents on the Red Sea coastline in Egypt, through the integration of both L-band SAR data of ALOS/PALSAR and high resolution optical data of RapidEye. This was achieved via using object-based image analysis method, through applying different machine learning algorithms, and evaluating various features such as spectral properties, texture features, and SAR derived parameters for discrimination of mangroves ecosystem classes. Three non-parametric machine learning algorithms were tested for mangroves mapping; random forest (RF), support vector machine (SVM), and classification and regression trees (CART). As an input for the classifiers, we tested various features including vegetation indices (VIs) and texture analysis using the gray-level co-occurrence matrix (GLCM). The object-based analysis method allowed clearly discriminating the different land cover classes within the mangroves ecosystem. The highest overall accuracy (92.15%) was achieved by the integrated SAR and optical data. Among all

classifiers tested, RF performed better than other classifiers. Using L-band SAR data was beneficial for mapping and characterization of mangroves growing in small patches. The maps produced represents an important updated reference suitable for developing a regional action plan for conservation and management of mangroves resources along the Red Sea coastline.

Keywords: Mangroves mapping, Pol-SAR, ALOS PALSAR, RapidEye, Red Sea.

1. INTRODUCTION

Mangroves are highly productive ecosystems located in the intertidal tropical and sub-tropical regions. They act as buffer zones between terrestrial and marine ecosystems, and therefore, play an important role in the functioning of adjacent ecosystems, such as salt marshes, seagrass beds, and coral reefs (Spalding *et al*., 1997). Mangroves support the conservation of biological diversity by providing habitats, nurseries, and nutrients for a number of animals and marine organisms (Barbier and Sathiratai, 2004). They are considered of great ecological importance in coastlines stabilization, reduction of coastal erosion, sediment, and nutrient retention, flood and flow control, and water quality (Giri *et al*., 2007; Gedan *et al*., 2011; Vo *et al*., 2013). They are also of high economic importance and often provide valuable ecosystem goods and services for local communities (Walters *et al*., 2008).

Despite of their economic and ecological importance, mangroves experience high yearly loss rates of 1–2% (Beaumont *et al*., 2011; Feller *et al*., 2010). High population pressure in coastal areas has led to the conversion of many mangroves areas to other uses, and numerous case studies described mangroves' losses over time (FAO, 2007). Among the reasons for this loss are over-exploitation, unsustainable wood extraction; conversion by urbanization, aquaculture; and alteration of the hydrological system (Hogarth, 1999; Lacerda, 2001). In addition, long-term climatic change and the different interacting effects associated with global temperature increase and sea-level rise are deemed as a global hazard to mangroves (Gilman *et al*., 2008). Degradation and loss of these coastal buffering systems due to climate change and direct human impacts contradict the coastal protection they provide and increase their vulnerability, with significant environmental, economic and social consequences for indigenous people in the coastal areas (Ellison, 2015).

Mangroves in Egypt represent the northern latitudinal limits of the Endo-Pacific East African mangroves. Due to the area's extreme environmental conditions (high salinity, low rainfall, and extreme temperatures), the trees are generally stunted, rarely exceeding five meters in height (FAO, 2007). They are found scattered along the Red Sea coastline, and their usual habitat is shallow water, such as lagoons, or sand bars parallel to the shoreline. Two of the four mangrove species known to occur in the Red Sea were recorded in Egypt; *Avicennia marina* (Forssk.) Vierh, and *Rhizophora mucronata* (Galal, 1999).

There is a growing demand for integrated assessment to address the risk on mangroves ecosystems, especially in the context of climate change, sea-level rise, and related threats to coastal ecosystems. Therefore, mapping and retrieval of up-to-date information regarding the extent and conditions of mangroves are essential for conservation and sustainable management of mangroves ecosystems on the Red Sea coastline. Mapping of mangroves requires frequent and spatially detailed assessments; such information can be prohibitively expensive to be collected directly. Remote sensing is the most appropriate tool for mapping and assessment of mangroves, due to its ability to capture high spatio-temporal variability over large geographical scales (Archibald and Scholes, 2007). Remote sensing provides a fast, cost-effective, and efficient methods for mangroves mapping, it is particularly useful since many mangroves extents are located in remote areas, where field measurements are difficult, time-consuming, and expensive (Held *et al*., 2003). Remote sensing data offers many advantages in this respect and has been used in several studies for mangroves mapping (Green *et al*., 1996). However, the accuracy of the mangroves maps is affected by the ability of the classification procedure to discriminate between various elements and vegetation types in the mangroves ecosystem, which is partly a function of the sensors' resolution, and the image processing method or classification procedure adopted. This gap remains to be addressed to be able to produce more accurate spatially explicit information based on remote sensing data to eventually support the sustainable management of mangroves ecosystems.

A variety of sensors and image processing methods have been used in the remote sensing of mangroves, such as SPOT (Système Pour l'Observation de la Terre) (Jensen *et al*., 1991; Rasolofoharinoro *et al*., 1998) and Landsat Thematic Mapper (TM) (Long and Skewes, 1996; Green *et al*., 1998). Since mangroves along the Red Sea coastline often grow in narrow small patches, high resolution remotely sensed data are required to capture the newly colonized individual stands or relatively small patches of mangroves stands that cannot be captured with medium spatial resolution satellite data *e.g.*, Landsat imagery. High resolution data provide opportunities for mangroves mapping and interpretation, as well as it can be used to recognize, identify, and delineate mangroves at the individual tree level (Neukermans *et al*., 2008).

Object-based image analysis (OBIA) is a suitable approach for the classification of high resolution satellite images, it allows extraction of meaningful objects, rather than single pixels during image segmentation because the spectral response of individual pixels no longer represents the characteristics of a target of interest e.g., tree canopies (Blaschke, 2010; Ke *et al*., 2010). OBIA involves the identification of homogeneous groups of pixels that have similar spectral and/or spatial characteristics (Hay and Castilla, 2008). In addition, the object-based image analysis offers various advantages of using spectral characteristics, texture, shape, and context information with adjacent image objects that can be used in the mapping of mangroves extents (Liu *et al*., 2006).

Although there are many advantages of using optical remote sensing data for mapping of mangroves, a major limitation is the availability of cloud-free scenes, which stimulates usage of other remote sensing datasets, such as the Synthetic Aperture Radar (SAR) data, and its more advanced operational mode polarimetric SAR (PolSAR) for mapping and characterization of mangroves extents. Several studies have demonstrated the potential of SAR data for mapping of mangroves indicating that SAR-based methods can potentially outperform the optical remote sensing data especially in the tropical areas, where cloud coverage restrain application of optical satellite images (Almeida-Filho *et al*., 2009; Hoekman *et al*., 2010; Häme *et al*., 2009).

SAR sensors are particularly used for woody structural mapping, because of their capacity to capture within-canopy properties (Le Toan *et al*., 2011; Sun *et al*., 2011; Santoro *et al*., 2007), and lack of sensitivity to cloudy conditions. L-band SAR provided by the Advanced Land Observing Satellite (ALOS) Phased Array L-band Synthetic Aperture Radar (PALSAR) has been proven to be the most effective in forests mapping and characterization (Mitchard *et al*., 2011; Carreiras *et al*., 2013; Naidoo *et al*., 2015) due to the high penetration of L-band into the canopy. L-band SAR data have been shown to be useful for mangroves mapping as a function of structural differences between species and growth stages (Lucas *et al*., 2007). Using SAR data in the mapping of mangroves is challenging because of the complexity of the backscatter signal received from mangroves ecosystems. Different bands of radar backscatter are affected differently by the interactions between the transmitted signal and biophysical properties of mangroves, such as size, geometry, orientation of leaves, trunks, branches, different types of roots, and the moisture content of both mangroves trees and the underlying soil (Lucas *et al*., 2007; Aslan *et al*., 2016).

The main objective of this study was to develop an approach for mapping of mangroves extents on the Red Sea coastline through the integration of both L-band SAR data of ALOS/PALSAR and high resolution optical data of RapidEye. We applied the object-based image analysis method and assessed different machine learning algorithms, as well as evaluated various input features for discrimination of mangroves ecosystem classes in the study area. The performed tests allowed to produce accurate mangroves maps in the study area as well as to make recommendations on the suitability of remote sensing data and selection of the classification methods for accurate mangroves mapping. This information is important for the development of a regional action plan for conservation and management of mangroves resources along the Red Sea coastline as well as could be applied for similar applications worldwide.

2. MATERIALS AND METHODS

2.1 Study area

Wadi Lehmy stand is located on the Red Sea coastline in Egypt (latitude 24◦130, longitude 35◦250, Figure 4.1). It is one of the few mangroves stands growing along the Red Sea coastline. The study area is divided into three main units: The Red Sea Mountains, the coastal plain, and the Red Sea coast. The coastal plain reaches in width from 15 to 25 km, and it is made of undulating sand and gravels that separates the mountainous range from the Red Sea coast. Mangroves grow in small patches along the Red Sea coast. As halophytes, mangroves thrive well in saline water, but require fresh water to a certain extent in order to maintain an optimum salinity balance and to get nutrients, which explains why mangroves grow on the mouths of wadis (seasonal riverbeds), where suitable sediments and sources of freshwater allow the mangroves to grow in a high-saline substrate frequently inundated by seawater.

Wadi Lehmy stand is dominated by *Avicennia marina*; it is a tolerant species to the relatively high salinity, low rainfall and high-temperature conditions (Zahran and Willis, 2009). Avicennia grows on a sandy substrate at the mouth of W. Lehmy, surrounding a shallow lagoon. The trees have developed morphological, physiological and reproductive adaptations to the high salinity of the swamp. Climatologically, the Egyptian Red Sea coast, which supports the distribution of mangroves, belongs to the category of warm coastal deserts. The climate of Ras Banas in the south shows an annual mean of the minimum and maximum temperature of 19.1 ◦C and 32.4 ◦C with an annual mean of 17.4 mm year^{-1} rainfall.

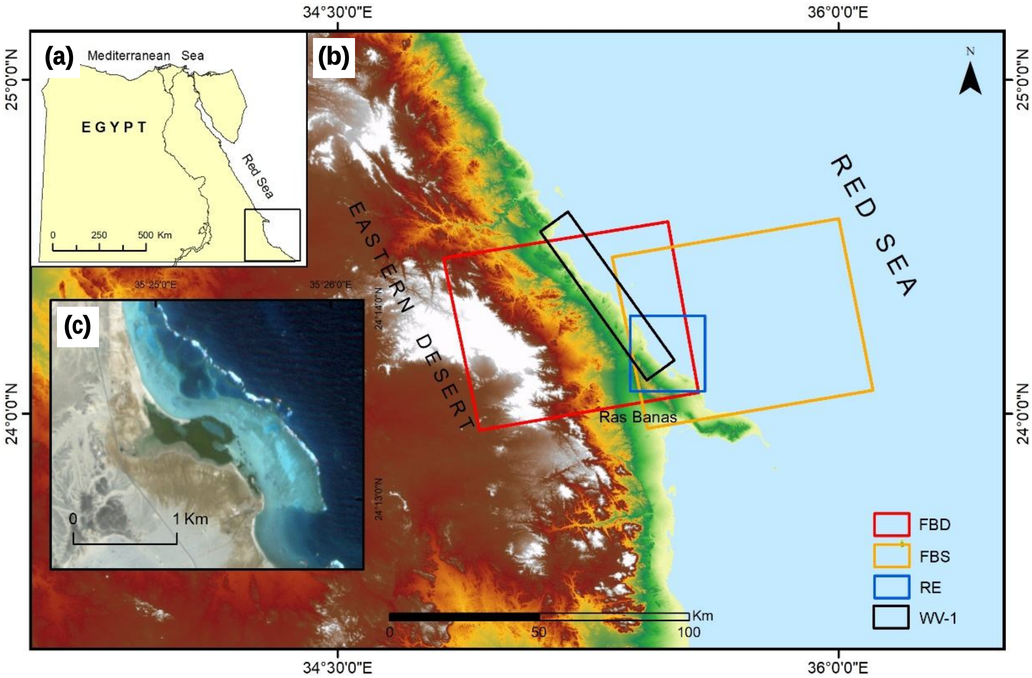

Figure 4.1. (**a**) Location of the study area on the Red Sea coastline in Egypt; (**b**) the study area overlaid on SRTM digital elevation model, and footprints of the remote sensing data used in this study; FBD: fine beam dual-polarization, FBS: fine beam single-polarization, RE: RapidEye, and WV-1: WorldView-1; and (**c**) subset of the RE image showing W. Lehmy stand.

2.2. Remote Sensing Data

This work is based on the integration of three different remote sensing datasets; SAR data provided by ALOS/PALSAR, high resolution optical data of RapidEye, and very high resolution data of WorldView-1. ALOS/PALSAR data used in this work was acquired at L-band (~23.6 cm wavelength), in a fine-beam dual-polarization mode (HH and HV), and fine-beam single polarization mode (HH), in an ascending orbit, with an off-nadir angle of 34.3°. Data were acquired in a slant range single-look complex format (SLC, L1.1) acquired on 22 June 2007. Each scene covers an area of approximately 60 × 70 km.

RapidEye is a commercial optical Earth observation mission that consists of a constellation of five satellites (Tyc *et al*., 2005). The sensors deliver high spatial resolution imagery with a ground sampling distance of 6.5 m at nadir. RapidEye image was acquired on 25 February 2015. It is a 3A product from the RapidEye

Science Archive (RESA) of the German Aerospace Centre (DLR). At this processing stage, the image was already radiometrically and geometrically corrected for sensor related issues and aligned to a cartographic map projection (WGS 1984/UTM zone 36N) (Wegmüller, 1999). WorldView-1 data with 0.5 m spatial resolution was acquired on 21 November 2015, the image was radiometrically and geometrically corrected. Our focus in the current study was on SAR data availability, particularly L-band; therefore, there is an unavoidable time of eight years between the acquisition times of PALSAR data and the optical data, assumed to be insignificant for observation and mapping of mangroves as woody vegetation (Santini *et al*., 2013).

ALOS/PALSAR images were pre-processed from the SLC format according to the following steps; (a) SAR images for a given acquisition mode (FBD) were co-registered using a cross-correlation algorithm (Wegmüller, 1999); (b) each SLC image was then calibrated to convert the DN values to radar backscatter coefficients ($\sigma°$) in decibels (dB) using the following formula (Shimada *et al*., 2009):

$$\sigma^{o}(dB) = 10 \times \log_{10}(DN^{2}) - 83.4, \qquad (1)$$

where DN is the image pixel digital number measured in the SAR image, and −83.4 is the calibration factor of ALSO/PALSAR data; (c) multi-looking was carried out using mode-specific factors aiming at achieving roughly squared pixels of 12.5 m in range and azimuth (Shimada *et al*., 2009; Maurizio *et al*., 2015), followed by subset of the obtained backscatter images to the boundaries of the study area; (d) 5 × 5 Lee filter was applied to the images to reduce the effect of speckle noise, Lee filter was selected because it preserves polarimetric information (Lee *et al*., 1999); (e) H/A/Alpha polarimetric decomposition parameters were extracted based on eigenvector decomposition of the (2 × 2) complex covariance matrix [C2] (Cloude and Pottier, 1997; Pottier *et al*., 2009) to be used along with the other derived SAR parameters for mangroves mapping; (f) terrain-correction was carried out to remove the effect of geometric distortions, such as foreshortening, layover, and shadow; and (g) geocoding of the images to the UTM projection (zone 36N and WGS-84 datum) using SRTM Digital Elevation Model (DEM) using Sentinel application platform (SNAP) V5.0 toolbox provided by European Space Agency (ESA). In addition to HH and HV, the ratio HV/HH, total power HV + HH and difference HV – HH were calculated. Finally, the HH, HV polarizations and all the derived parameters were stacked to one multi-layered image for further analyses.

In addition to remote sensing data, other ancillary data were used in the current study including the SRTM DEM data, it was used to identify the potential mangrove areas based on the elevation, mangroves normally survive in the intertidal zones; therefore, SRTM could be used to identify the potential mangrove areas (Treuhaft *et al*., 2004).

2.3. Data Analysis

Following image pre-processing, various procedures were performed to prepare the multi-sensor with multi-resolution input bands alongside with the derived and calculated features and parameters of both SAR and optical data for the subsequent analysis and categorization for mangroves mapping and characterization.

Two different methods were used to combine information from the remote sensing datasets used in the current study. The first method is data fusion; it combines information from multi-source images to obtain a new image with more information that can be separately derived from the original images (Pohl and Van Genderen, 1998; Amarsaikhana *et al*., 2010; Ehlers *et al*., 2010). This method was used to combine the optical data of RapidEye image with a five-meter spatial resolution, and the Worldview-1 image with 0.5 m spatial resolution, to enhance the visual interpretation and improve the quantitative analysis performance of both datasets for mangroves mapping. Several data fusion techniques have been tested including; the intensity-hue-saturation (IHS), Brovey transformation, Gram Schmidt fusion, and Ehlers fusion techniques (Pohl and Van Genderen, 1998; Benz *et al*., 2004; Lang, 2008; Amarsaikhana *et al*., 2010; Ehlers *et al*., 2010), the IHS method was applied in this study for preserving the multispectral characteristics and improving the spatial features in the output. The second method is data integration, it combines images in different layers algorithmically, without creating a new set of images (Pohl and Van Genderen, 1998; Amarsaikhana *et al*., 2010). It was applied to combine both SAR data of ALOS/PALSAR and optical data of RapidEye to investigate the potential of the integrated SAR and optical data for mapping of mangroves, while optical data represent the reflective properties of ground cover, SAR data are sensitive to the shape, roughness and moisture content of the observed objects (Figure 4.2).

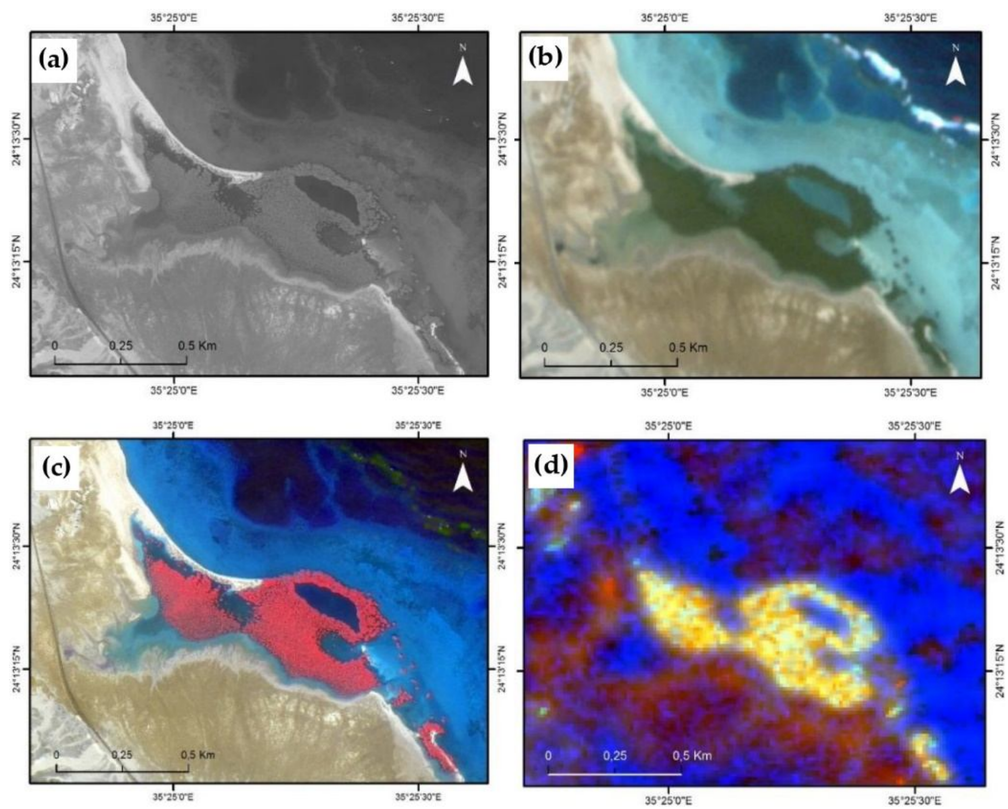

Figure 4.2. Remote sensing data covering the study area (**a**) WorldView-1 image; (**b**) RapidEye image (RGB); (**c**) Pan-sharpened RapidEye image (NIR, R, G); and (**d**) dual-polarization ALOS/PALSAR data in RGB (HH, HV, HV/HH).

2.4. Field Data

Field data were obtained from a field expedition carried out in the study area in June 2013. During this expedition, field measurements including; ground truth data (GPS points) with a corresponding short description were collected randomly to determine topographic reference points, and the main geographical features in the study area, as well as vegetation patterns, species distribution, and identification of the mangroves ecosystem classes (Figure 4.3). Five classes were identified within the mangroves ecosystem in the study area, these classes are; mangroves (MV), water (WT), intertidal zone (TZ), waterlogged areas (WG), and coastal plain (CP). Additionally, apart from the GPS-based sampling, the higher resolution optical data were utilized for ground-truthing purposes especially within the mangroves swamps and remote areas that were not accessible during the field work (Figure 4.4).

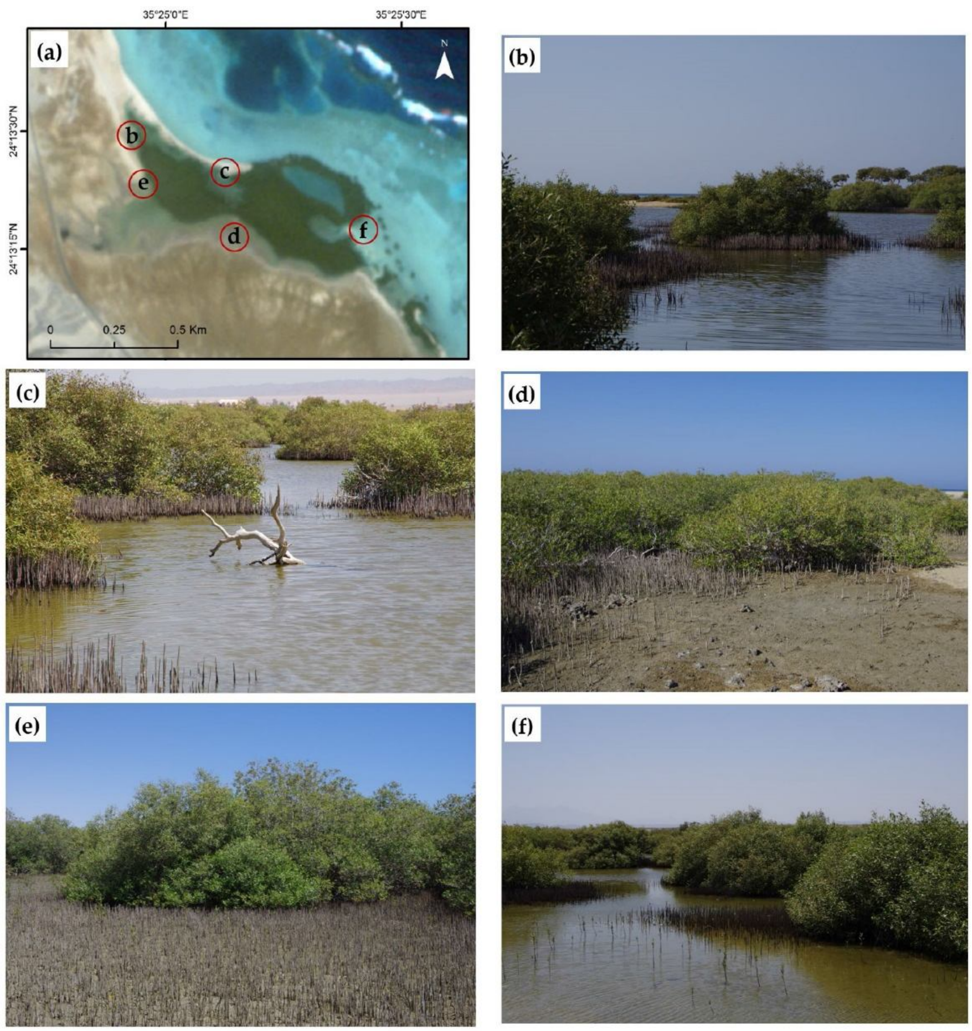

Figure 4.3. (**a**) RapidEye image showing mangroves extent at W. Lehmy stand on the Red Sea coastline, and (**b**–**f**) Field photographs collected during the fieldwork in the study area, showing the mangroves ecosystem and the surrounding habitats.

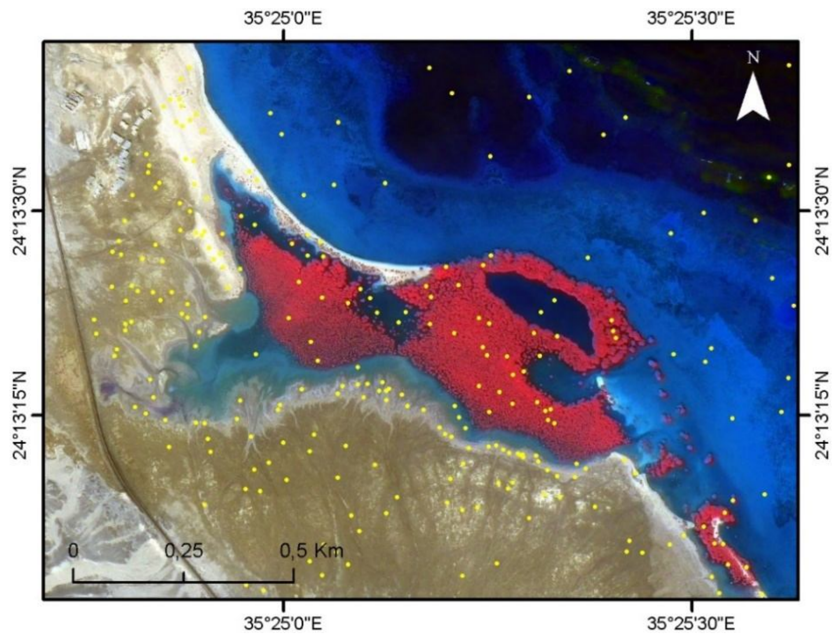

Figure 4.4. Distribution of the sampling points overlaid on the pan-sharpened RapidEye image.

2.5. Object-Based Image Analysis and Feature Extraction

An Object-oriented approach was applied in this study for mapping of mangroves extents. This approach is based on classifying objects that are delineated as homogeneous units with similar spectral characteristics, called segments. Segmentation provides the building blocks of the object-based image analysis (Hay and Castilla, 2008; Lang, 2008). This approach is suitable for classification of high resolution satellite images, as it allows the extraction of meaningful objects, rather than classifying individual pixels (Blaschke, 2010). Segmentation enables the acquisition of a variety of spectral, spatial, and textural features, resulting in improved classification accuracy (Baatz and Schäpe, 2000; Benz *et al*., 2004).

Image pixels of the optical and SAR data with relative homogeneity were clustered using the multi-resolution segmentation algorithm MRS (Xiaoxiao *et al*., 2014) in eCognition Developer V9 (Definiens, 2009). MRS is an ascending area-merging technique where smaller objects are progressively merged into larger objects controlling the advancement in heterogeneity based on three user-defined parameters: scale, shape, and compactness (Laliberte *et al*., 2007). Scale parameter, which regulates the size and homogeneity of image objects (Marceau, 1999), was adjusted until the obtained image objects visually represented the features of interest (canopy cover of mangroves trees). All layers were given equal importance in the segmentation settings, except NIR Infrared, and Red bands, which received double weighting to increase their response signal to vegetation greenness. A bottom-up, region-growing segmentation approach was used to produce consistent results across the relatively heterogeneous study area (Münch *et al*., 2017). Figure (4.5) provides an overview of the entire approach adopted in this study.

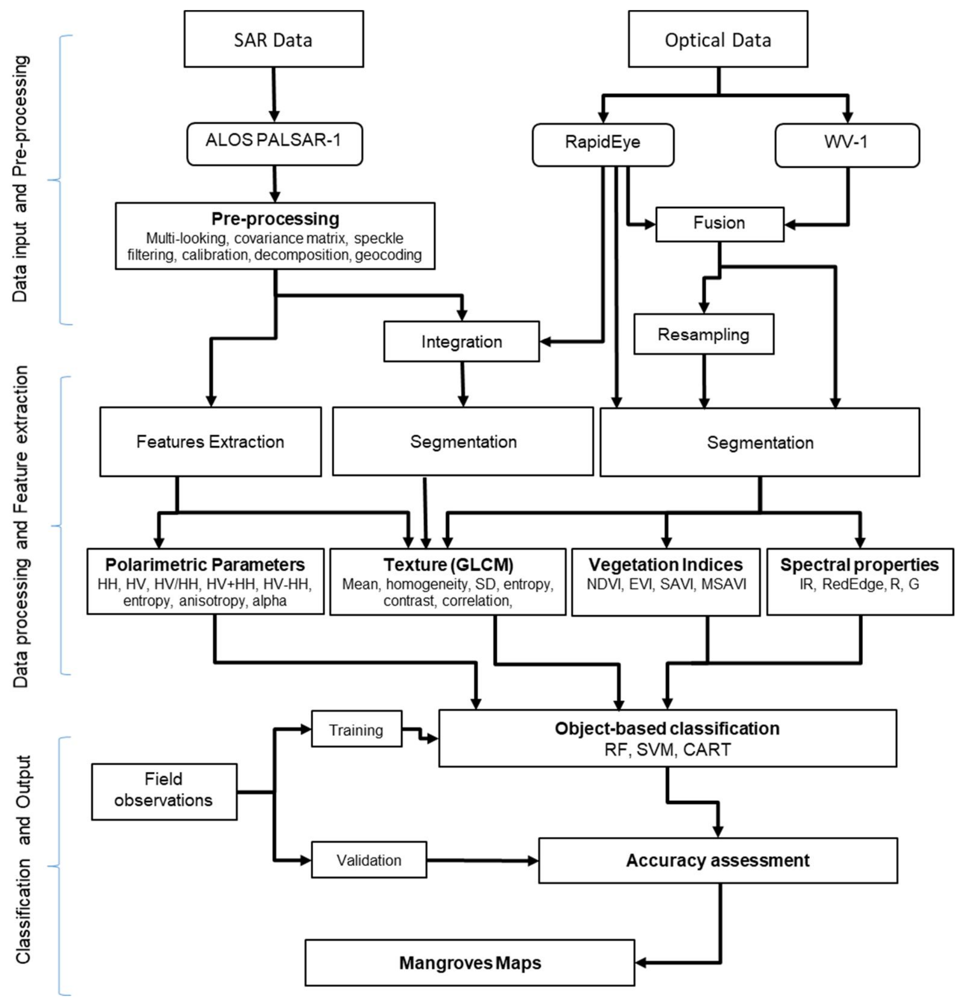

Figure 4.5. Flowchart of the proposed methodology, WV-1: WorldView-1 data, VIs: Vegetation Indices, RF: Random forest, SVM: Support-vector machine, and CART: classification and regression trees.

Several object-based features can be calculated and extracted in eCognition and applied during the classification procedure. In this study, various features were extracted, including vegetation indices (VIs), principal component analysis (PCA) (Taylor, 1977), and gray-level co-occurrence matrix (GLCM) (Haralick *et al*., 1973). VIs and PCA are widely used for the retrieval of vegetation structure as well as land cover classification (Hurni *et al*., 2013). We have selected the following VIs (Table 1): The Normalized Difference Vegetation Index (NDVI), Green Normalized Difference Vegetation Index (gNDVI), Enhanced Vegetation index (EVI2), Soil-adjusted Vegetation Index (SAVI), and Modified Soil-adjusted Vegetation index (MSAVI). NDVI was selected to separate mangroves from other non-vegetated areas. To address the limitations of NDVI that is affected by soil brightness (Carlson and Ripley, 1997) and saturates in high biomass areas (Huete *et al*., 2002; Wang *et al*., 2002), EVI2 was calculated as it shows greater sensitivity to vegetation and reduces atmospheric effects on vegetation index values (Huete *et al*., 2002). SAVI (Haboudane *et al*., 2004) was computed as a corrective index on soil brightness for areas with low vegetation cover and exposed soil surface. The brightness algorithm was calculated to represent the reflectance intensity of bare rocks and soils among other features sharing similar spectral radiance (Kauth and Thomas, 1976; Schönert *et al*., 2014).

GLCM texture measures make use of grey-tone spatial dependence matrix to quantify texture features. The GLCM expresses texture in a user-defined kernel size and considers the spatial co-occurrence of pixel grey levels (Dorigo *et al*., 2012). A kernel size of 7 × 7 was applied to avoid exaggeration of variations with smaller kernel size, or inefficient quantification of texture because of smoothing with larger kernel size (Lu and Batistella, 2005). In addition to the mean (MEN) and variance (VAR), other texture features were also computed for each band including: homogeneity (HOM), contrast (CON), entropy (ENT), dissimilarity (DIS), correlation (COR), and second moment (SEC) as shown in Table (4.1).

Table 4.1. Vegetation indices, and texture features used in this study.

Categories	Variables	Algorithm	Reference
VIs	NDVI	$(NIR - R)/(NIR + R)$	(Tucker, 1979)
	gNDVI	$(NIR - G)/(NIR + G)$	(Gitelson *et al.*, 1996)
	EVI2	$2.5(NIR - R) / (NIR + 2.4 \times R + 1.0)$	(Jiang *et al.*, 2008)
	SAVI	$1.5(NIR - R)]/[NIR + R + 0.5$	(*Huete, 1988*)
	MSAVI	$2(NIR + 1) - \sqrt{\{(NIR + 1)^2 - 8\,(NIR - R)\}}/2$	(Qi *et al.*, 1994)
GLCM texture	MEN	$f\ men = \sum_{i,j=0}^{N-1} i(p_{ij})$	(Haralick *et al.*, 1973)
	VAR	$f\ var = \sum_{i,j=0}^{N-1} p_{ij}\,(i - \mu_i)^2$	
	HOM	$f\ hom = \sum_{i,j=0}^{N-1} p_{ij}/1 + (i - j)^2$	
	CON	$f\ con = \sum_{i,j=0}^{N-1} p_{ij}\,(i - j)^2$	
	ENT	$f\ ent = \sum_{i,j=0}^{N-1} p_{ij}\,(-\ln p_{ij})$	
	DIS	$f\ dis = \sum_{i,j=0}^{N-1} p_{ij}\,\lvert i - j\rvert$	
	COR	$f\ cor = \sum_{i,j=0}^{N-1} p_{ij}\,[(i - \mu_i)(j - \mu_j) / \sqrt{\{(\sigma_i{}^2)(\sigma_j{}^2)\}}\,]$	
	SEC	$f\ sec = \sum_{i,j=0}^{N-1} p_{ij}{}^2$	

NDVI: Normalized difference vegetation index; gNDVI: green Normalized difference vegetation index; EVI2: Enhanced vegetation index; SAVI: Soil adjusted vegetation index; MSAVI: Modified soil adjusted vegetation index; NIR: Near Infrared; R: Red; G: Green. $p_{i,j} = v_{i,j}/\sum_{i,j=0}^{N-1} v_{i,j}$, where $v_{i,j}$ is the value in the cell, i, j of the moving window and N is the number of rows or columns.

Backscattering characteristics of mangroves were investigated using the HH, and HV polarizations offered by the FBD mode of ALOS/PALSAR data, and their polarimetric parameters were retrieved. Decomposition features of, co-, and cross-polarized SAR data were retrieved according to the Alpha-Entropy decomposition proposed by Cloude and Pottier (Cloude and Pottier, 1997), including; entropy (H), anisotropy (A), and alpha angle (α), and the class separability offered by their different feature spaces were analyzed. GLCM texture measures were applied also for the SAR bands and their derived parameters to evaluate their influence on the classification of mangroves ecosystem. Extracted and calculated features were then evaluated to determine the importance of the predefined variables of both SAR and optical data for distinguishing between the different classes in the mangroves ecosystem.

2.6. Image Classification

Three classification scenarios were applied in the current study; Scenario 1 (GA) used only optical images information with the five multispectral bands of RapidEye (blue, green, red, red-edge, and near-infrared) and its calculated features and indices including VIs, PCA as well as texture GLCM features. Scenario 2 (GB) used all the available features from ALOS/PALSAR data; SAR bands and SAR derived parameters including PolSAR and decomposition parameters, as well as the texture GLCM features. Scenario 3 (GC) integrated both optical and SAR data as well as the calculated and derived features, parameters and texture of both datasets to examine the potential of the integrated optical and SAR data in mapping of mangroves extents. Table (4.2) show the three proposed scenarios with different categories, datasets, and selected features and combinations.

Table 4.2. Proposed scenarios for the classification schemes using optical data of RapidEye, SAR data of ALOS/PALSAR, and the integrated optical and SAR data.

Category		Datasets	Selected Features and Combinations
GA	GA1	Spectral bands	B, G, R, Red Edge, and NIR
	GA2	Spectral bands, VIs, and PCA	B, G, R, Red Edge, NIR, VIs, pc1, and pc2
	GA3	Spectral bands, VIs, PCA, and texture	B, G, R, Red Edge, NIR, VIs, pc1, pc2, and texture
GB	GB1	SAR bands	HH and HV
	GB2	SAR bands, PolSAR parameters, and GLCM texture	HH, HV, HV/HH, HV + HH, HV − HH, H, A, α, and GLCM texture
GC	GC1	Spectral bands, and SAR bands	B, G, R, Red Edge, NIR, HH, and HV
	GC2	Spectral bands, VIs, SAR bands, and PolSAR parameters	B, G, R, Red Edge, NIR, VIs, HH, HV, HV/HH, HV + HH, HV − HH, H, A, and α
	GC3	Spectral bands, SAR bands, and PolSAR parameters	B, G, R, Red Edge, NIR, HH, HV, HV/HH, HV + HH, HV − HH, H, A, and α
	GC4	Spectral bands, VIs, and SAR bands	B, G, R, Red Edge, NIR, VIs, HH, and HV
	GC5	Spectral bands, VIs, SAR bands, PolSAR parameters, and texture	B, G, R, Red Edge, NIR, VIs, HH, HV, HV/HH, HV + HH, HV − HH, H, A, α, and GLCM texture

GA: optical data; **GB**: SAR data; **GC**: integrated optical and SAR data; **PCA**: principle components; B: blue; G: Green; R: Red; NIR: near infrared; PolSAR: Polarimetric SAR; VIs: vegetation indices; H: entropy; A: anisotropy; and α: alpha angle.

Because of the variability of the data proposed in the classification schemes (Table 4.2), a comparison of machine learning algorithms was conducted for choosing suitable classification algorithms. We evaluated three different non-parametric classifiers: random forest (RF), support vector machines (SVM), and classification and regression trees (CART). RF is a machine ensemble approach that makes use of multiple self-learning decision trees to parameterize models and use them for estimating categorical or continuous variables (Gislason *et al*., 2006). SVM is a non-parametric statistical learning approach, which can resolve complex class distribution in high dimensional feature spaces (Vapnik, 1982). SVM algorithms discriminate the classes by fitting an optimal separating hyperplane (OSH) between classes using the training samples within feature space and to maximize the margins between OSH and the closest training samples (Foody, 2004; Van Der Linden and Hostert, 2009). The points lying on the boundaries are called support vectors and the middle of the margin is the OSH (Meyer, 2014).

CART is increasingly being used for analysis and classification of remotely sensed data. It has been used successfully for the classification of multispectral imagery (Friedl and Brodley, 1997; Lawrence and Wright, 2001), incorporation of ancillary data with multispectral imagery for increased classification accuracy (Foody, 2002), and change detection analysis (Rogan *et al*., 2003).

2.7. Accuracy Assessment

Accuracy assessment was carried out for the classified images using the high spatial resolution pan-sharpened RapidEye image to check the correspondence of the produced classes to real objects in the study area. If the results were not satisfactory, the classification was improved by selecting more features for better separation of the different classes of mangroves ecosystem. During the training of the classifiers, there was an independent test set for the classification accuracy. Tuning of the classifiers was carried out in a systematic way to identify the most suitable tuning parameters; the number of trees built in the forest (ntree), and the number of possible splitting variables for each node (mtry). Finally, a statistical accuracy assessment was conducted using a confusion matrix. The accuracy assessment was carried out through splitting the data into 70% for the training of the classifiers, and the other 30% for testing the classification results (Rogan *et al*., 2003; McCoy, 2005). The parameters of overall accuracy, producer accuracy, user accuracy, and Kappa coefficient (Congalton and Green, 1999) were derived from the confusion matrix and used for the accuracy assessment of the classified images.

3. RESULTS

3.1. Backscattering Characterization and Parameters Description

Mean backscattered coefficients were identified for the five main land-cover types of the mangroves ecosystem in the study area: mangroves (MV), water (WT), intertidal zone (TZ), waterlogged areas (WG), and coastal plain (CP). Table (4.3) shows the variation of backscattering coefficients for each class at different polarizations HH and HV. It was observed that the class of water (WT) showed the lowest backscattered intensities. The majority of the pixels lying in the range from −26.54 dB to −18.59 dB and from −29.40 dB to −25.96 dB from both HH and HV respectively, a smooth water surface results in no scattering back to the sensor in both HH and HV polarizations. Coastal plain (CP) also showed low backscattered values but slightly higher than WT due to the involvement of soil surface roughness. While higher values were observed in dense homogenous mangroves cover (MV) −8.19 dB and −16.86 dB for both polarizations HH and HV respectively. HV backscattered is closely correlated with mangroves structure and above-ground biomass, with HV reaching higher σ^0 values due to higher sensitivity to volumetric scattering influenced by the random distribution of branches and leaves. The intertidal zone (TZ) and waterlogged areas also showed high backscattering values (WG). Reflections between the vertical aerial roots of mangroves and the water surface of the flooded intertidal zone can result in a strong HH backscatter (Table 4.3).

Table 4.3. Backscatter statistics of PALSAR data for each of the five classes in the mangroves ecosystem.

Class	HH Backscattering (dB)			HV Backscattering (dB)		
	Range	Mean	SD	Range	Mean	SD
WA	−26.54 to −18.59	−23.66	2.15	−29.40 to −25.96	−28.04	1.07
MV	−10.98 to −05.72	−8.19	1.35	−20.37 to −14.60	−16.86	1.18
TZ	−18.77 to −15.51	−16.10	3.36	−27.96 to −24.99	−26.38	0.65
WG	−18.67 to −15.30	−17.15	1.14	−28.81 to −26.68	−27.77	0.55
CP	−24.27 to −20.58	−22.46	0.94	−29.11 to −27.44	−28.26	0.48

The Alpha-Entropy decomposition was generated from eigenvalues-based target decomposition (Figure 4.6). The different classes of mangroves ecosystem overlap each other showing predominantly surface scattering with moderate alpha values and relative high entropy values in the dual-polarization mode. Volume scattering characterizes the mangroves' stand with higher biomass values and multiple canopies. The low values of alpha represent surface scattering characterizing the plane surfaces found in WA and CP classes (Figure 4.6).

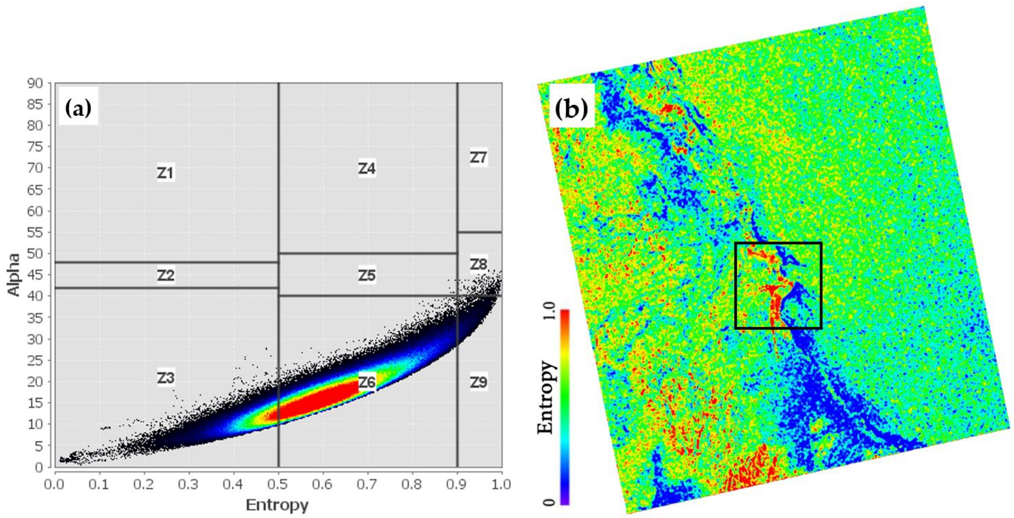

Figure 4.6. (**a**) H-Alpha plane plot of Cloude–Pottier decomposition; and (**b**) Entropy of the entire scene as retrieved from ALOS/PALSAR data, the square box highlights the location of mangroves stand.

3.2. Segmentation and Feature Extraction

The pan-sharpened RapidEye image (Figure 4.7a) achieved the best segmentation results and produced fine units (Figure 4.7b). Shape and compactness were weighted at 0.1 and 0.5, respectively, and scale was set to five due to land cover heterogeneity in the study area. The segments were relatively well divided where mangroves appeared on the coastline. This is because the pan-sharpened RapidEye image has the highest spatial resolution compared to the other optical and SAR data used in this study, and at the meantime keeping the spectral information of the RapidEye multi-spectral image, while the segmentation of SAR data did not divide the vegetation units into many details despite using the same parameter settings. Furthermore, since SAR data contain speckle noise, using SAR imagery for segmentation resulted in obtaining objects that do not correspond to real-world objects (Figure 4.7).

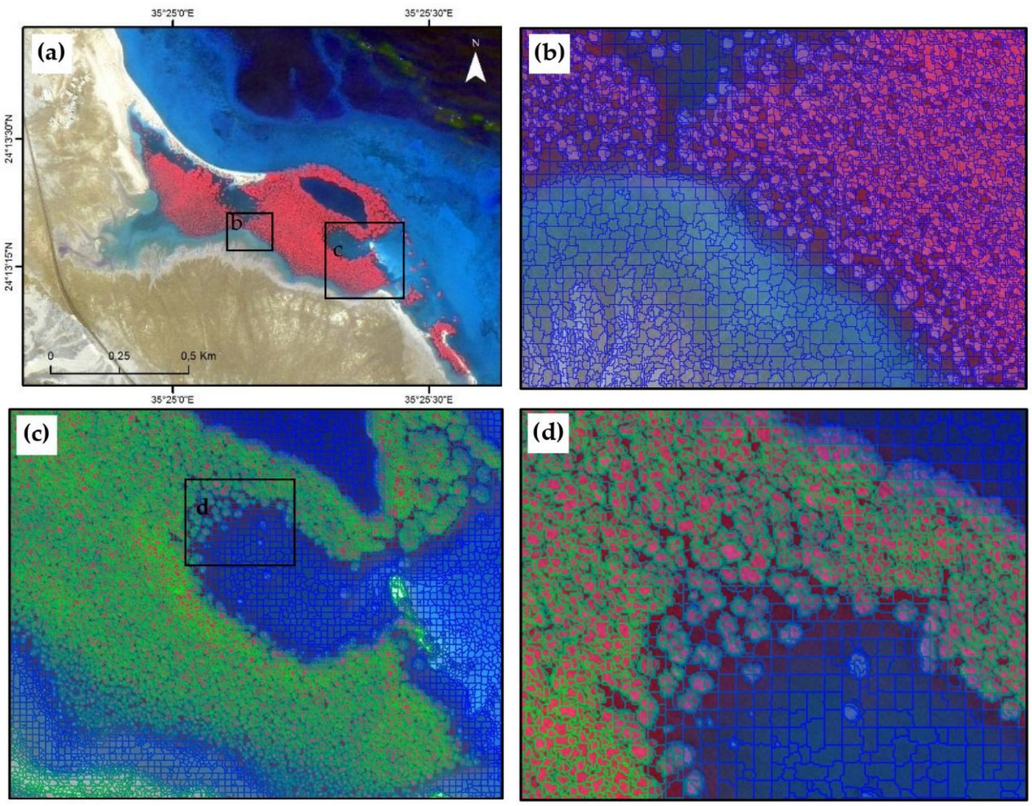

Figure 4.7. (**a**) Pan-sharpened RapidEye image used for segmentation; (**b**) the results of segmentation at [0.1, 0.5, and 5] for shape, compactness, and scale parameters; (**c**) using the object-feature (NIR band) for mangroves feature extraction; and (**d**) delineation of the canopies of mangroves trees in the study area on the Red Sea coastline based on the selected segmentation parameters and extracted object-feature.

3.3. Classification Results and Accuracy Assessment

Table (4.4) provides a summary of the classification results achieved for all data categories; classification of optical data, classification of SAR data, and classification of the integrated SAR and optical data. In category GA (optical data only), the highest overall accuracy achieved was 86.78% in subgroup GA1. The addition of the derived features VIs and PCA to the spectral bands improved the overall accuracy to 89.26% in subgroup GA2. This shows the influence of the derived features (VIs and PCA) on improving the classification accuracy. Classification results indicate that high resolution optical data of RapidEye has the potential to categorize land cover classes within the mangroves ecosystem efficiently (Table 4.4, Figure 4.8).

Table 4.4. Classification Overall accuracies and Kappa coefficient of the classified datasets based on RF, CART, and SVM classifiers.

Categories	Subgroups	Overall Accuracy (OA) %			Kappa Coefficient (K) %		
		RF	CART	SVM	RF	CART	SVM
GA (Optical data)	GA1	86.78	74.42	60.33	83.44	68.14	50.73
	GA2	89.26	83.72	74.79	86.57	79.68	68.63
	GA3	82.23	26.03	76.45	77.86	9.02	70.63
GB (SAR data)	GB1	59.92	53.31	38.43	50.15	42.71	21.19
	GB2	69.83	54.65	45.04	62.21	44.36	32.31
GC (Integrated optical and SAR data)	GC1	74.42	63.95	75.97	68.28	54.74	70.23
	GC2	84.71	68.18	80.23	80.89	60.62	75.29
	GC3	92.15	88.43	62.02	90.18	85.53	52.32
	GC4	87.60	84.11	52.71	84.55	80.04	38.83
	GC5	84.30	78.10	79.25	80.42	72.78	74.04

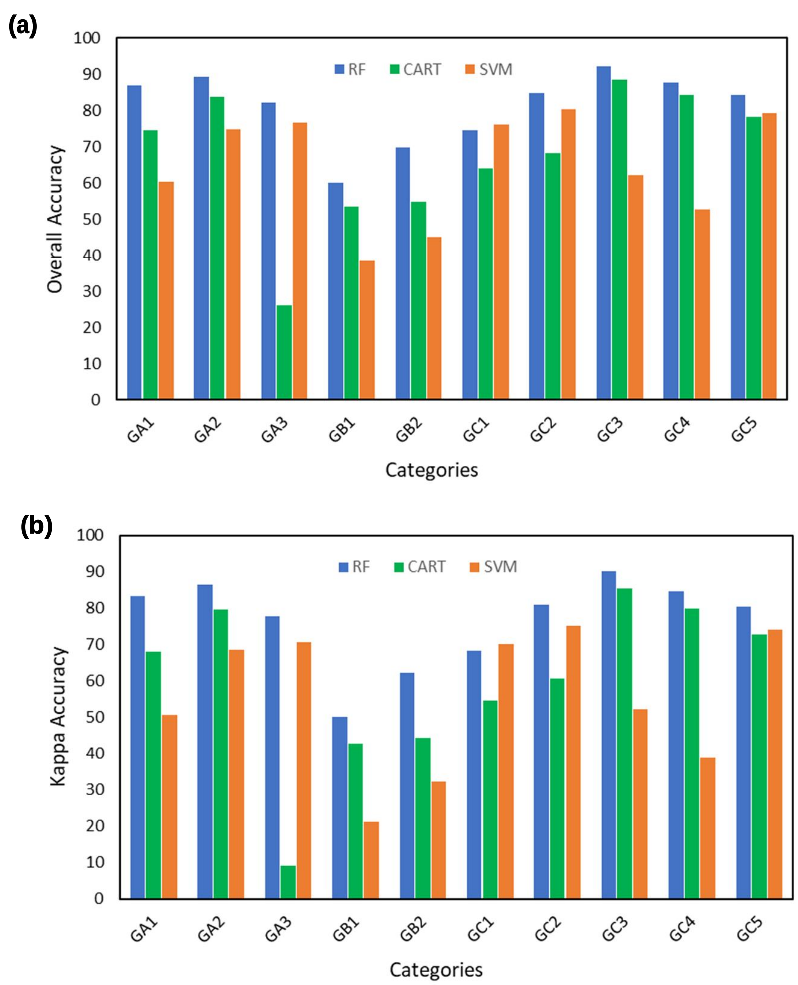

Figure 4.8. (**a**) Classification Overall accuracies; and (**b**) Kappa coefficient, of the classified categories based on RF, CART, and SVM classifiers.

In category GB (SAR data only), the overall accuracy of the RF, CART, and SVM classifications with SAR inputs were 59.92%, 53.31%, and 38.43% respectively in subgroup GB1, and improved to 69.83%, 54.65%, and 45.04% respectively in subgroup GB2 after using PolSAR parameters and texture feature derived from both polarizations (Table 4.4, Figure 4.8).

In category GC (integrated SAR and optical data), the results obtained in this category indicated that the average overall classification accuracies of the data in subgroups GC1–GC5 ranges between 74% and 92% using RF classifier. SAR derived parameters combined with derived features of optical data improved the classification accuracy as indicated in subgroup GC2. The highest overall classification accuracy was achieved in subgroup GC3 based on the integration of SAR backscattering and PolSAR parameters, with surface reflectance of the optical data (92.15%). These results indicate that separability tends to increase, and an improvement in terms of classification accuracy could be achieved when SAR backscattering and SAR derived parameters combined with the surface reflection of optical data. The use of VIs in GC2 and GC4, and texture feature in GC5 slightly improved the accuracy to 84.71%, 87.60%, and 84.30% respectively (Figure 4.8). In general, results of the classification of the three datasets and their accuracy assessment indicated that the derived vegetation indices improved the classification accuracy of the optical dataset in GA, similarly, in SAR dataset GB the accuracy increased after including the derived PolSAR parameters and texture feature into the SAR backscattering. The integrated SAR and optical datasets achieved the highest overall accuracies, and the addition of PolSAR parameters and texture feature improved the accuracy as shown in (GC3), and (GC5) respectively (Figure 4.8).

Figure (4.9) shows the producer's accuracy (PA) and user's accuracy (UA) based on RF, CART and SVM classifications. Based on the producer's accuracy; the class (MV) achieved the highest accuracy of more than 90%, followed by the class of (WA), and the lowest producer's accuracy achieved by the class (WG). Regarding to the user's accuracy, the class (WA) achieved the highest accuracy of more than 90%, followed by the class (CP), and the lowest user's accuracy of less than 70% achieved by the class (MV).

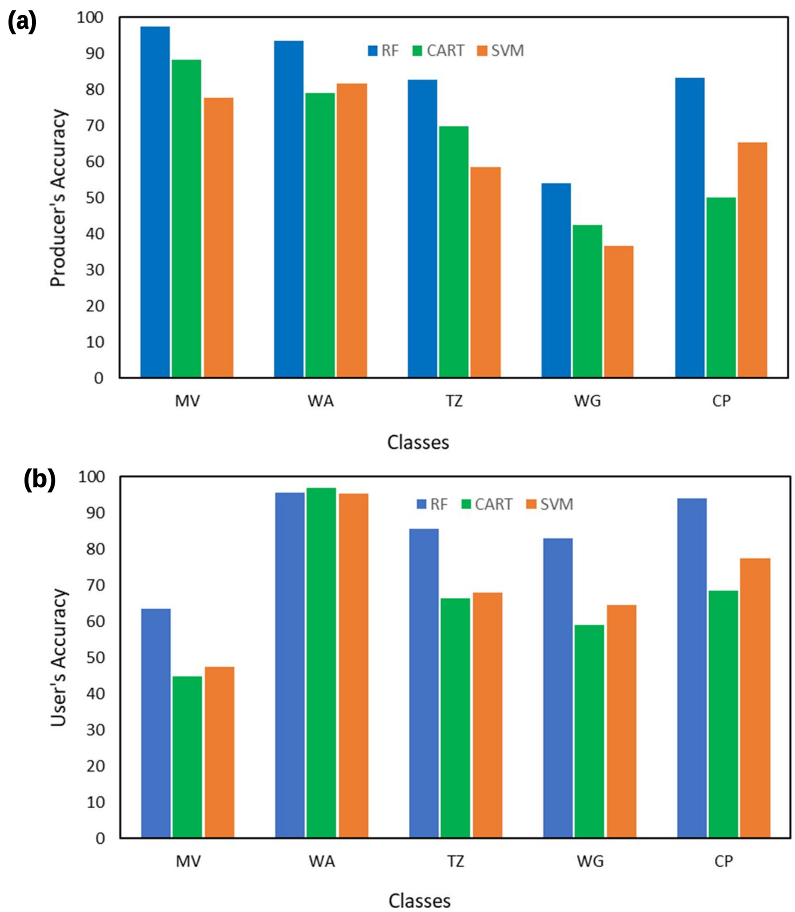

Figure 4.9. (**a**) Producer's accuracies PA%; and (**b**) User's accuracy UA% for different mangroves ecosystem classes based on RF, CART and SVM classifications.

We compared the performance of the three machine learning classifiers used in the current study, RF achieved the highest overall classification accuracy (92.15%) followed by CART with 88.43%, and SVM with 80.23%. Similarly, for the kappa coefficient, RF achieved the highest kappa 90.18% at GC3, while CART and SVM achieved 85.5% and 75.3% at GC3 and GC2, respectively. The highest performance was achieved using the integrated SAR and optical data (GC), the RF increased significantly the accuracy compared to CART and SVM. For SAR data (GB), RF increased the accuracy in the range of 9.91% compared to SVM in the range of 6.61% and CART in the range of 1.34% (Table 4.4). We calculated the variable importance for the different variables evaluated in the current study. Of all variables of optical data, the vegetation indices, particularly gNDVI was found to be the most valuable for class discrimination, while in SAR data, SAR band VH contributed to better class separation. Classification results displaying the distribution of the different land cover classes over the study area, and mapping the mangroves extents are presented in Figure (4.10). The map was produced using the integrated SAR and optical dataset.

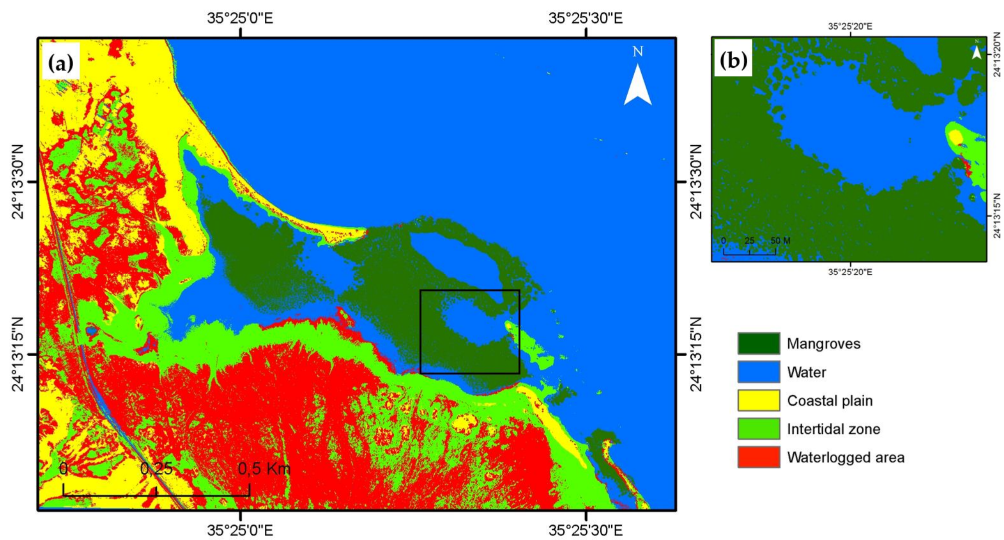

Figure 4.10. (**a**) Classification output of the integrated SAR and optical dataset using RF classifier, displaying the different land cover classes of the mangroves ecosystem in the study area; (**b**) show the delineation of the canopies of the mangroves trees.

4. DISCUSSION

This study demonstrates how remote sensing of the polarimetric SAR data and high resolution optical data can be used for mapping of mangroves extents growing in small patches. In the current study, L-band SAR data of ALOS/PALSAR dual-polarization, and high resolution optical data of RapidEye were used for accurately mapping mangroves extents on the Red Sea coastline in

Egypt, showing the effectiveness of integrating different data types for mangroves mapping.

We found that the integrated SAR and optical data achieved the highest accuracy in classifying the five land cover types in the mangroves ecosystem in the study area. The obtained accuracy value is similar to other classifications based on integrated SAR and optical data in African environments (Haack and Bechdol, 2000; Laurin *et al*., 2013). Data integration improved the classification accuracy by using different data sources to increase the dimensionality of the available information (Ramsey *et al*., 1998; Waleska *et al*., 2011; Lang and McCarty, 2008). The integration of SAR and optical data has been shown to be a good strategy for overcoming the limitations of the optical data, including the availability of cloud-free scenes, and also coping with the limitations of SAR data for single-date information. Our findings are in agreement with (Waleska *et al*., 2011), they mapped 8 classes of land cover near the mouth of the Amazon River using supervised classification of Landsat ETM and a merged ETM–SAR product. The integrated product increased the accuracy and provided additional information, permitting a more efficient identification and mapping of tropical coastal wetlands.

Random Forest classifier achieved the highest accuracy brought in an improvement in the results with respect to other used classifiers. In certain studies, SVM and RF achieved similar performance (Ghosh *et al*., 2014), in other studies, SVM classifier outperforms RF classifier (Burai *et al*., 2014). Unlike the traditional and fast learning decision trees CART, RF is insensitive to small changes in the training datasets and are not prone to overfitting (Prasad *et al*., 2006; Ismail *et al*., 2010). Additionally, RF is less complex and less computer intensive in comparison to the long training times for SVM (Anguita *et al*., 2010). Other studies such as (Wang *et al*., 2008) achieved success with an ANN algorithm to map mangroves species from multi-seasonal IKONOS imagery. The decision to adopt machine learning algorithms should take into consideration the need for expert knowledge, for classifiers optimization and avoiding overfitting.

We applied an object-based approach for mangroves mapping in the current study. This approach allowed to clearly discriminate the different land cover classes within the mangroves ecosystem. Our results are in agreement with (Kamal *et al*., 2015), they applied an object-based approach for multi-scale mangrove composition mapping using multi-resolution data (Landsat TM, ALOS AVNIR-2, and WorldView-2) in two study sites in Australia and Indonesia, the results demonstrated the effectiveness of object-based analysis for mangroves mapping. Our results also are in agreement with (Vo *et al*., 2013), they applied multi-resolution segmentation for mangroves mapping in the Mekong Delta using SPOT5 data, and successfully detected areas with mixed aquaculture-mangrove land cover with high accuracies. The main limitation of the mapping approach related to the classification rule set was its site, sensor and time dependency. This limitation was due to the spectral reflectance variations of the images captured by different sensors and the variations of the mangrove environmental settings. The only uncertainty introduced in the accuracy assessment in the current study was attributed to the time gap of eight years between the acquisition times of PALSAR data and the optical data. Some level of change in mangrove condition may have occurred within this time gap. However, we notice that there was no major disturbance affecting the study areas within this time gap. This difference assumed to be insignificant for observation and mapping of woody vegetation in the arid and semi-arid environments (Santini *et al*., 2013; Kamal *et al*., 2015).

With regards to the techniques tested in the current study to improve the mapping accuracy, we found that the addition of different features derived from both optical and SAR data was effective in improving the overall accuracy; VIs improved the classification accuracy of optical data, texture features improved the classification accuracy of SAR data, and also the accuracy of the integrated SAR and optical data, similarly to what has been found by (Longepe *et al*., 2011) in tropical forests, confirming the value of textural information when this data type is used singularly, and especially for discriminating classes of dense and tall vegetation. Our results are in agreement with several studies which used derived features and parameters for improving classification accuracy. In the study carried out by (Wang *et al*., 2004), the authors found that inclusion of image texture information improved the classification accuracy, and produced promising results. On the other hand, texture features were much less effective when included with optical data, perhaps due to the fact that very high values of accuracy were already reached and thus the margins of improvement were limited. PolSAR parameters improved the classification accuracy of both SAR data and the integrated SAR and optical data. We realized also the addition of different features improved the overall accuracy into a certain margin as seen in GC3, and the addition of more features after this margin reduced the overall accuracy as seen in GC4 and GC5 (Table 4.4).

In this study, we showed that using SAR data only can still provide important landscape information. This result confirms SAR's role in forest and vegetation mapping of tropical regions and suggests that in the areas affected by optical data loss because of the atmospheric conditions, SAR data can be integrated with the available optical data. Using L-band SAR data was beneficial for mapping of mangroves because of the high penetration of L-band into the canopy, HH polarization has been found to be sensitive for detecting water beneath canopy (Hess *et al*., 1995), whereas HV polarization has been known for its sensitivity to volume scattering and biomass (Bourgeau-Chavez *et al*., 2009). Compared to single polarized SAR data, the dual-polarimetric SAR data provided much more information about the backscattering mechanism of the mangroves ecosystem. Therefore, dual-polarimetric SAR data enables a more detailed mapping of mangroves. These results are in agreement with (Souza-Filho *et al.*, 2011), they determined the best polarization configurations (HH, VV, or HV) to discriminate different types of coastal Amazon wetlands, the classification accuracy was slightly improved when combining polarizations, with an overall accuracy of 83% versus single-pol accuracies between 78% and 81%.

The current study shows that using L-band SAR data provided by ALOS PALSAR combined with the high resolution optical data of RapidEye is very useful in mapping of mangroves extents growing in fractions and small patches on the Red Sea coastline, as it provides information on the spatial distribution of mangroves and mangroves ecosystem, which is required for conservation and management of mangroves in this area. In the future work, we will continue using the next generation of L-band SAR data; ALOS-2 PALSAR. It will allow comprehensive monitoring of the Earth surfaces by providing users with more detailed SAR data than ALOS data, allowing continued mapping and monitoring of mangroves ecosystems with higher spatial and temporal resolution.

5. CONCLUSION

In this study, we investigated the contribution of the dual-polarimetric L-band SAR data of ALOS/PALSAR and the high resolution optical data of RapidEye for mapping mangroves extents on the Red Sea coastline. The study also assessed the contribution of various features derived from both SAR and optical datasets including VIs, PCA and GLCM texture as well as the PolSAR parameters derived from the ALOS/PALSAR data to the overall accuracy, using different machine learning algorithms and comparing their performance. The highest overall classification accuracy of 92.15% was achieved by the integrated SAR and optical data. The VIs improved the overall accuracy of optical data classification. Texture features and PolSAR parameters improved the overall accuracy of SAR data, and the integrated SAR and optical data classifications. RF classifier has the highest performance followed by CART, and the lowest accuracy achieved by SVM. The study showed that using SAR data of ALOS/PALSAR integrated with optical data of RapidEye was very useful in the mapping of mangroves extents growing on the Red Sea coastline. The produced maps provided accurate information on the spatial distribution of mangroves in the study area, which is required for the conservation and sustainable management of mangroves in this area.

Chapter 5

Assessing the Impact of Drought on Grasslands using S1 SAR data

This chapter is based on ***Abdel-Hamid, A.****; Dubovyk, O., Valerie, G., and Greve, K. 2019. Assessing the impact of drought stress on grasslands using multi-temporal SAR data of Sentinel-1: A case study in Eastern Cape, South Africa. European Journal of Remote Sensing, In Review.*

ABSTRACT

Grasslands are a major component of the natural vegetation in South Africa, it covers almost one-third of the country's land surface. The current study focuses on assessing the impact of drought stress on communal and commercial grasslands in Eastern Cape using multi-temporal analysis of Sentinel-1 SAR data. Data analysis included retrieval of biophysical parameters of grasslands using Sentinel-1 SAR backscattering coefficients. Correlation analysis was performed between SAR data and NDVI values extracted from Landsat-8 optical data. Linear mixed-effects regression analysis was performed for detecting the impact of drought stress on communal and commercial grasslands during a drought and non-drought growing seasons. Our results indicate that vegetation dynamics in grasslands ecosystems in the study area are highly responsive to climatic fluctuations. A significant correlation between backscattering coefficients of Sentinel-1 SAR data (VH and VV) and NDVI was observed for both communal and commercial grasslands (R^2 = 0.89). Results also demonstrated that communal grasslands are more affected by drought impact than commercial grasslands. In commercial grasslands, management activities can improve the growing conditions of grasslands, reduce the impact of drought, and subsequently increase the resilience and productivity of this ecosystem.

Keywords: Grasslands; drought monitoring; Sentinel-1; Eastern Cape; South Africa.

1. INTRODUCTION

Grasslands cover more than 40% of the Earth's land surface, and are widely used for livestock grazing and fodder production, thereby contributing to global food production in major ways (FAO, 2006). They are a major component of the natural vegetation in South Africa, and covers almost one third of the country's land surface, with a biome comprising 295,233 km^2 of the central regions of the country, extending across the boundaries of seven provinces, and spanning a complex array of socio-economic situations and land use contexts (Palmer and Ainslie, 2005). They provide a range of ecosystem services including the protection of soil fertility, control of soil erosion, and influencing the hydrological cycle (Weigelt *et al*., 2009). In addition, grasslands are among the species-richest vegetation communities in the world, and therefore have important conservation value (Linnell *et al*., 2015). However, the ecosystem services provided by grasslands, and biodiversity, grasslands ecosystems are facing several pressures due to the impact of climate change and unsustainable land management practices. As the local population and especially the rural communities depend on the functionality of these ecosystems, there is a need to understand and detect involved processes that might lead to a potential degradation (Wessels *et al*., 2007).

Climate change is commonly recognized as one of the most important drivers affecting plant ecosystems (Piras *et al*., 2016). Drying and warming climate usually decreases vegetation productivity (Li *et al*., 2013). Grasslands productivity is largely controlled by the amount and timing of precipitation and corresponding seasonal fluctuations in soil water content (Parton *et al*., 2012). Temperature is also an important regulator of grassland productivity (Liu *et al*., 2006). Drought has been a major factor influencing vegetation dynamics in grasslands (Cook *et al*., 2007), and it has substantial social and economic consequences (Wilhite and Buchanan-Smith, 2005). Severe drought can limit grasslands production (Knapp and Smith, 2001), alter nutrient cycling (Evans and Burke, 2013), and increase wildfire risk and susceptibility to invasive plant species (Abatzoglou and Kolden, 2011). Quantifying the economic and social impacts of drought on grasslands is complex due to the wide range of ecosystem services impacted. There is a critical need to understand how drought affects grasslands, in part because drought severity and drought-associated grasslands disturbances are expected to increase with climatic change.

Remote sensing offers a unique perspective for drought monitoring that complements the *in situ*–based climate data traditionally used for this application. Spaceborne sensors provide repeat coverage of spatially continuous measurements collected in a systematic, and objective manner. Vegetation estimates from MODIS and AVHRR have been extensively used for studying vegetation dynamics (Piñeiro *et al*., 2006), but complex spatial patterns that result from the interaction of disturbances with soils, topography, and vegetation are often undetectable with moderate-low resolution sensors (0.25–1 km). Satellite-based indices such as the Normalized Difference Vegetation Index (NDVI) became increasingly used for various environmental monitoring applications including drought monitoring (Kogan, 1997; Peters *et al*., 2002).

Although optical sensor data are useful for drought monitoring, there is a limitation for data acquisition due to cloud contamination. Synthetic Aperture Radar (SAR) data have been used to complement the cloud problems of optical data because SAR data are not influenced by weather conditions (Lang and McCarty, 2008). Due to their sensitivity to dielectric and structural land surface features, SAR remote sensing techniques have shown their potential to derive spatial information from land surfaces, especially radar backscatter from polarimetric SAR systems allows a detailed description of different vegetation and soil properties. Several operational mapping algorithms rely on SAR backscattering from single-polarized (e.g., HH, HV, or VV), dual-polarized (HH/HV or VV/VH), or quad-polarized (HH/HV/VV/VH) SAR data (Morandeira *et al*., 2016). Despite these advantages, there are few SAR-based studies for drought monitoring and assessment of vegetation dynamics in grasslands. The main reason these products have not been developed is the limited availability of SAR data (Santoro *et al*., 2015), which results in spatial and temporal discontinuities when quantifying vegetation dynamics as a result of climate change across broader geographic regions. Until recently, systematically collected SAR datasets, such as that from the Sentinel-1 satellite (Berger *et al*., 2012), have not been available. The European Space Agency currently provides Sentinel-1 SAR data with potentially global coverage that may greatly improve land surface monitoring.

The main objective of this study is to assess the impact of drought stress on communal and commercial grasslands in Eastern Cape Province based on the analysis of multi-temporal SAR data of Sentinel-1. Specific objectives are; (a) evaluation of the potential of Sentinel-1 data in monitoring and retrieval of biophysical parameters of grasslands, (b) characterization and interpretation of the backscattering parameters of grasslands, and (c) assessment of the impact of drought stress on both communal and commercial grasslands in the study area.

2. DATA AND METHODS

2.1 Study Area

The study area is located in Eastern Cape Province, the second largest province in South Africa, with a topographic and climatic complexity and diversity (Clark *et al*., 2009). The mountainous region in the study area forms part of the Great Escarpment Mountains and dominated primarily by grasslands, with large patches of forest on the southern aspects (Hoare and Bredenkamp, 2001). Land ownership is divided into two tenure systems; a privately (commercially) owned land tenure system and communally owned land tenure system. Communal land was predominantly located within the former homeland territories and on municipal land around each town in South Africa.

The climatic conditions in Eastern Cape vary from mild warm temperatures to subtropical conditions at the coast. Droughts can occur throughout the year, but grasslands are particularly vulnerable to droughts in the summer during the growing season which mainly goes from September to March. The precipitation regime is characterized by a large variability at various time scales from intra-seasonal, through inter-annual to decadal and multi-decadal (Kane, 2009). Two main study locations were selected in Sakhisizwe municipality in Eastern Cape, covering the two main grasslands tenure systems; communal and commercial grasslands (Figure 5.1).

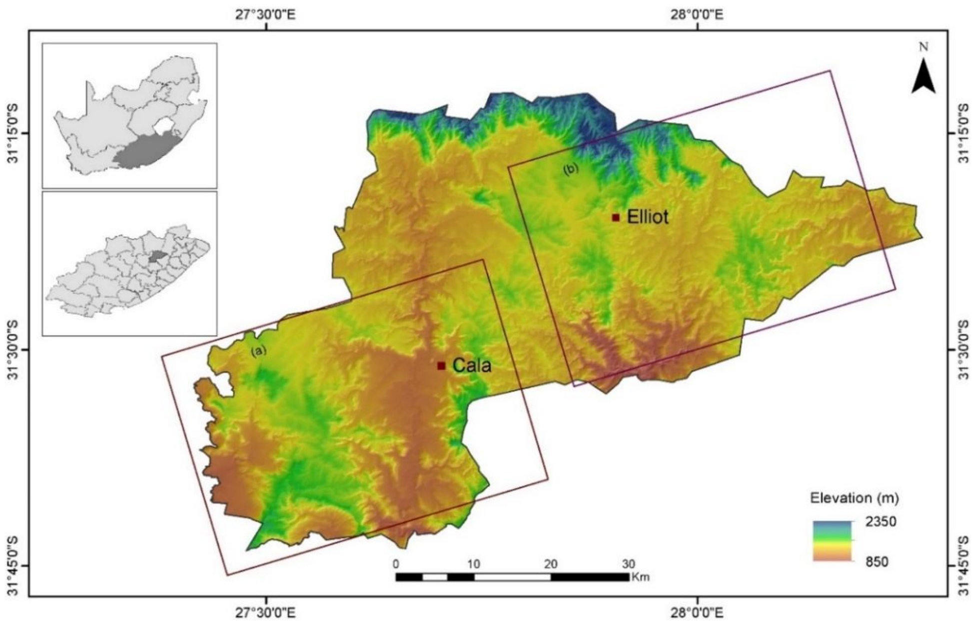

Figure 5.1. Map showing the location of the study area in Eastern Cape Province overlaid on SRTM digital elevation model; (a) communal grasslands, and (b) commercial grasslands.

2.2. Remote Sensing Data

Sentinel-1 SAR data covering the study area were acquired from the European Space Agency (ESA). As part of the Copernicus mission, Sentinel-1 carries a single C-band synthetic aperture radar instrument operating at a centre frequency of 5.405 GHz, and composed of a constellation of two satellites (Sentinel-1A and B) to assure data continuity provided by the ERS-1/2 and ENVISAT satellites (Torres *et al*., 2012). Sentinel-1A was launched in April 2014, and Sentinel-1B was launched in April 2016, jointly provide a nominal 6-day repeat cycle, allowing for continuous monitoring of land surfaces. Sentinel-1 operates in four image modes with various observation strategies, swath widths, and spatial resolutions; the Strip Map mode (SM), Interferometric Wide swath mode (IW), Extra Wide swath mode (EW), and Wave swath mode (WV). Twenty-four scenes of Sentinel-1 SAR data were acquired, covering two growing seasons (2015/2016 and 2016/2017). All the acquired data are in dual-polarization VV/VH, acquired in the Interferometric Wide swath mode (IW), in the GRD format, and product level 1. They are in a range and azimuth resolution of 5m and 20m, respectively. Table (5.1) shows the specifications of the Sentinel-1 data used in the current study.

Table 5.1. Sentinel-1 SAR data used in the current study. All data are in IW mode.

No.	Acquisition Date / Time	Track	Orbit	Pass	No.	Acquisition Date / Time	Track	Orbit
1	2015/10/13 16:53:19	14	8136	Asc	13	2016/10/07 16:53:33	14	13386
2	2015/10/25 16:53:19	14	8311	Asc	14	2016/10/19 16:53:33	14	13561
3	2015/11/06 16:53:19	14	8486	Asc	15	2016/11/12 16:53:33	14	13911
4	2015/11/30 16:53:14	14	8836	Asc	16	2016/11/24 16:53:33	14	14086
5	2015/12/12 16:53:14	14	9011	Asc	17	2016/12/06 16:53:33	14	14261
6	2015/12/24 16:53:13	14	9186	Asc	18	2016/12/18 16:53:32	14	14436
7	2016/01/17 16:53:12	14	9536	Asc	19	2017/01/11 16:53:30	14	14786
8	2016/01/29 16:53:12	14	9711	Asc	20	2017/01/23 16:53:30	14	14961
9	2016/02/10 16:53:22	14	9886	Asc	21	2017/02/04 16:53:30	14	15136
10	2016/02/22 16:53:12	14	10061	Asc	22	2017/02/16 16:53:30	14	15311
11	2016/03/05 16:53:12	14	10236	Asc	23	2017/03/12 16:53:30	14	15661
12	2016/03/17 16:53:12	14	10411	Asc	24	2017/03/24 16:53:30	14	15836

Asc = Ascending pass.

In addition to SAR data, Landsat-8 Operational Land Imager (OLI) optical data were used in the current study, Landsat provides the longest continuous archive of optical satellite data for land surface mapping and monitoring. The launch of the Landsat-8, in particular, has brought new opportunities and a platform for continuity in optical remote sensing. Landsat-8 surface reflectance scenes covering the study area in Eastern Cape during the two growing seasons of grasslands (2015/2016 and 2016/2017) were used in the current study to calculate the Normalized Difference Vegetation Index (NDVI) (Tucker, 1979). Vegetation indices are less sensitive to image-to-image noise, viewing geometry, and atmospheric attenuation, making them particularly advantageous over reflectance products when using large area mosaics covering scenes spread over multiple paths, rows, and dates (Vermote *et al*., 2016).

2.3. Climate Data

Meteorological data covering the main study locations with communal and commercial grasslands, and the surrounded area in Eastern Cape Province, were obtained from the South African Weather Service Organization. The original climatic data were the daily records of precipitation and temperature from 2014 to 2017. In addition, precipitation information based on the Climate Hazards Group Infrared Precipitation with Station (CHIRPS) data were used in the current study. The CHIRPS product provides daily precipitation data for the quasi-global coverage of 50°N-50°S from 1981 to present. The latest product is Version 2.0. It belongs to the "satellite-gauge" category (Funk *et al*., 2015).

2.4. Reference Data

Field work was carried out in the study area in Eastern Cape Province in October 2017, for validation of the remote sensing data analysis. During the field work, field measurements with the corresponding description of the test sites were collected using previously predefined test sites and covering the two study locations in commercial and communal grasslands (Figure 5.2). Identification of the grasslands into the two different tenure systems; communal and commercial grasslands, was also carried out during the field work. In addition to the collected data during the field work; land cover information covering the study area were obtained based on the South African National Land-cover dataset for South Africa produced by GEOTERRAIMAGE in 2013–2014 with overall accuracy of 81.73%, which used to extract the grasslands layer (Graw *et al*., 2017).

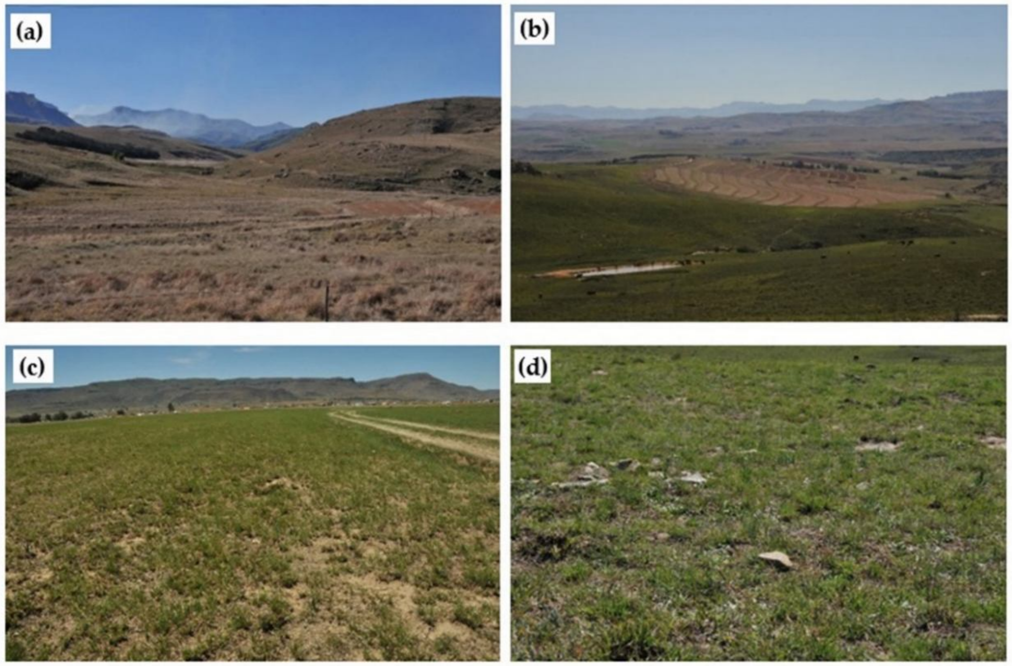

Figure 5.2. Photographs collected during the fieldwork showing the different landforms, and different terrain and topography as well as the different grasslands conditions in commercial grasslands (a & b), and communal grasslands (c & d).

2.5. Data Pre-processing

Sentinel-1 intensities data covering the study area consists of cross-polarized (VH), and co-polarized (VV) data from the high resolution Level-1 ground range detected products (GRD) were speckle-filtered, multi-looked, geocoded, and terrain corrected, followed by calculation of the backscattering coefficients ($\sigma°$) in decibel-scale (dB) (Small, 2011). Lee-Sigma filter (Lee *et al*., 2009) with a combination of 5 x 5 kernels were used to reduce the speckle noise. The image pixels were multi-looked to 30m square pixels using a bilinear method to be consistent with the Landsat-8 data. Terrain correction was conducted using the recently released STRM 1 arc-second (approximately 30m) digital elevation model (DEM). SNAP toolbox (Sentinel Application Platform) developed by ESA was used for SAR data processing.

Landsat-8 images were gathered and processed in Google Earth Engine (GEE, 2015). GEE stores surface reflectance data scenes, which have been pre-processed. The pre-processing steps include geometric and atmospheric correction, cloud masking and resampling to 30m. Landsat-8 images were further processed in the GEE environment to calculate the Normalized Difference Vegetation Index (NDVI). NDVI is one of the most frequently used parameters in vegetation monitoring and eco-climatological studies and is computed as:

$$NDVI = (\rho \quad - \rho \ ) / (\rho \quad + \rho \ ) \qquad (1)$$

Where ϱ_{nir} and ϱ_{r} are the surface reflectances in the near-infrared and red spectral range, respectively. Its values range between -1 and 1, with more positive values indicating green vegetation. Non-vegetated surfaces are not represented robustly and typically show values < 0.3.

CHIRPS data covering the study area during the study periods; drought season (2015/2016), and non-drought season of grasslands (2016/2017) were downloaded, geometrically corrected, cropped to the extent of the study area, aggregated, and resampled to (30 m.). Grasslands information was extracted from the land cover dataset of the study area. Figure (5.3) shows the calculated and extracted products from the remote sensing data used in the current study.

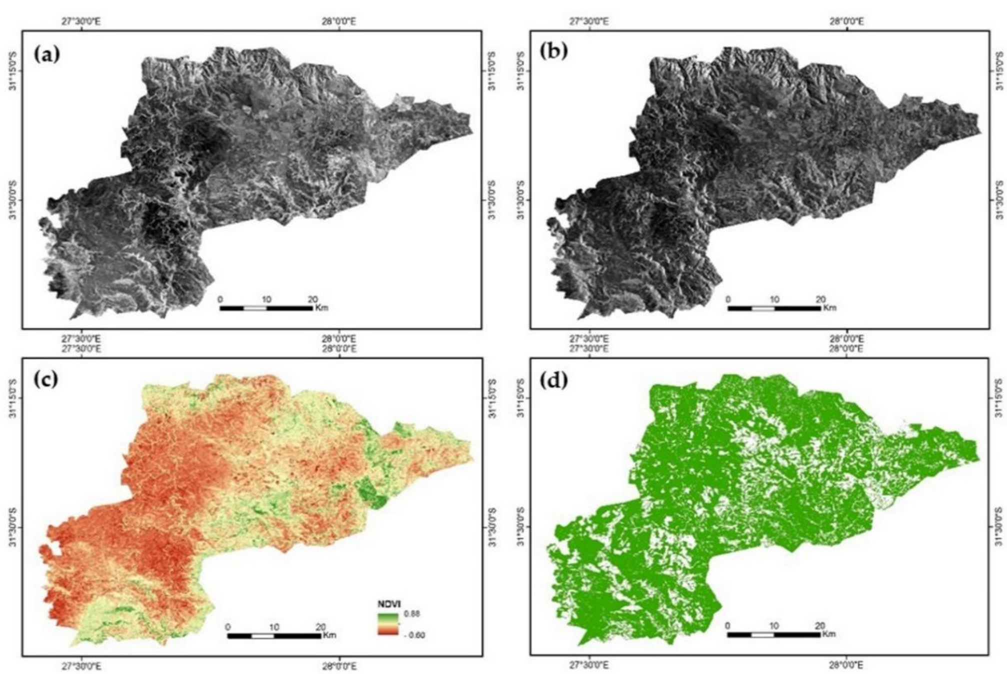

Figure 5.3. Calculated and extracted products used in the current study during the growing season of 2015/2016; (a) VH backscattering coefficient, (b) VV backscattering coefficient, (c) Landsat-8 derived NDVI, and (d) grasslands layer extracted from the land cover dataset.

2.6. Data Analysis

Data analysis in the current study consists of three main steps, (a) multi-temporal analysis of Sentinel-1 SAR data and retrieval of grasslands biophysical parameters, (b) relationship between Sentinel-1 SAR data and Landsat-8 NDVI, and (c) detection of the impact of drought stress on communal and commercial grasslands. Figure (5.4) provides an overview of the entire approach adopted in this study.

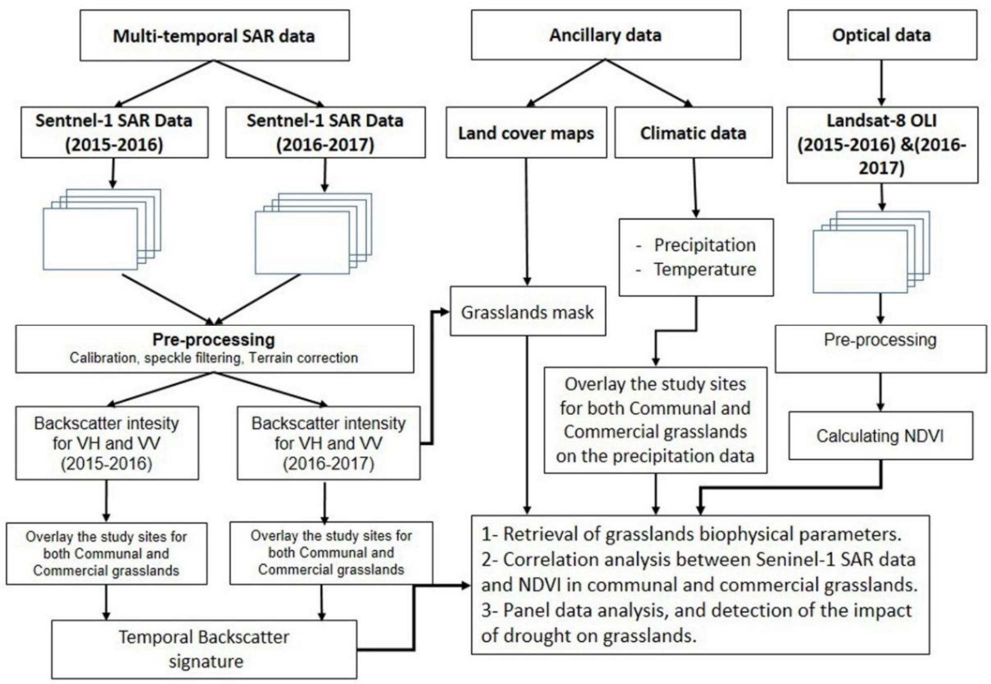

Figure 5.4. Flowchart of the methodology adopted in the current study.

2.6.1. Temporal analysis of Sentinel-1 SAR data and retrieval of grasslands biophysical parameters

Time series analysis of remotely sensed data is a useful tool for monitoring and characterization of land surface features across large areas. In the current study, a time series analysis was performed using Sentinel-1 SAR data to retrieve the biophysical parameters of grasslands in the study area during a drought season 2015/2016 and non-drought season 2016/2017. We focused on deriving the phonological parameters of grasslands using the backscattering coefficients of Sentinel-1 data; VH and VV. The outcomes of the time series analysis were information on the phenological parameters (growth stages of grasslands) for both communal and commercial grasslands during the two growing seasons. Afterwards, the backscattering was overlaid on the precipitation data for better interpretation of the backscattering parameters and understanding the relationship between changes in the backscattering intensities and the corresponding change in precipitation in the study area. In the last step, we compared the backscattering coefficients between the two different study locations with communal and commercial grasslands during the two growing seasons.

2.6.2. Relationship between Sentinel-1 SAR data and Landsat-8 NDVI

Pearson's correlation analysis was used to test the relationship between Sentinel-1 SAR data (backscattering of VH and VV), and Landsat-8 NDVI in communal and commercial grasslands in the study area during the drought and non-drought seasons. The relationships between SAR data and NDVI were analyzed and compared to investigate the potential of using SAR data of Sentinel-1 with Landsat-8 NDVI to estimate the variations between grasslands in communal and commercial grasslands during the drought and non-drought growing seasons. The relationship between SAR backscattering and NDVI is described by the following linear model:

$$dB = a_0 + a_1 D \quad (2)$$

Where a_0 and a_1 are coefficients of the regression modeling, and D is the vegetation index NDVI. In addition, as precipitation has a varied impact on vegetation growth in grasslands ecosystems, we compared the vegetation-precipitation dynamics to evaluate the response of grasslands to the variation in precipitation over communal and commercial grasslands during the drought and non-drought seasons. Data analysis was performed using R version (3.5.0).

2.6.3. Detection of the Impact of Drought stress on Grasslands

We applied a panel data analysis to compare the impact of drought stress on communal and commercial grasslands in Eastern Cape. Regression analysis was performed using the time series of SAR data; VH backscattering, as well as VV backscattering during the drought and non-drought growing seasons of grasslands. Additionally, regression analysis was also conducted using the time series of NDVI for the study sites in both seasons. We applied a linear mixed-effects maximum likelihood (ML) regression model according to the following equation:

$$y = X\beta + Zu + \varepsilon \qquad (3)$$

Where **y** is the n x 1 vector of responses, **X** is the n x p fixed-effects design matrix, $\boldsymbol{\beta}$ are the fixed effects, **Z** is the n x q random-effects design matrix, **u** are the random effects, ε is the n x 1 vector of errors (McLean *et al.*, 1991). All statistical analysis was performed using STATA 14 software.

3. RESULTS

3.1. Characteristics of the climatic conditions in the study area

In South Africa, extreme droughts are sometimes triggered by El Niño Southern Oscillation (ENSO), a quasi-periodic invasion of warm sea surface waters into the central and eastern tropical Pacific Ocean, returning at least once in any ten-year period (Rouault and Richard, 2005). In 2015/2016, South Africa experienced a combined effects of a severe drought and a strong El Niño event. National authorities in South Africa qualified it as the worst in 23 years (Vogel and van Zyl, 2016). This severe drought resulted in significant declines in the harvest in particular during 2016, and seriously depleted the water reserves, the drought has also had a ripple effect on the country's economy that contributed to a decline in Gross Domestic Product. The socio-economic effects of drought across the region are evident, extensive and have negatively affected key sectors of the economy, such as agriculture and food security (Baudoin *et al.*, 2017).

We compared the mean temperature and total precipitation during the drought season 2015/2016 and the non-drought season 2016/2017 in commercial and communal grasslands in the study area. The results highlighted the climatic variations between the two study locations. Communal grasslands received the least amount of rainfall within the growing season, accompanied by increased mean annual temperature than commercial grasslands, with higher mean temperatures in the drought season than the normal growing season (Figure 5.5).

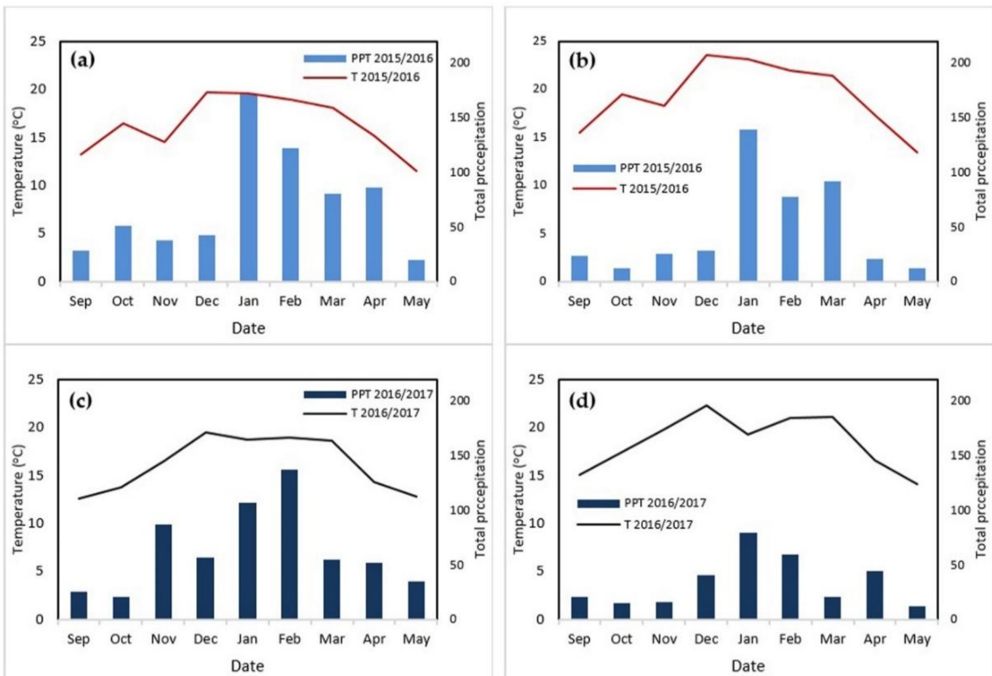

Figure 5.5. Overview of the mean temperature and total precipitation in the study area; (a) in commercial grasslands, and (b) in communal grasslands, during the growing season 2015/2016; and (c & d) during the growing season 2016/2017.

3.2. Temporal analysis of Sentinel-1 SAR data and retrieval of grasslands biophysical parameters

As grasslands in the study area are divided into two major tenure systems; commercial and communal grasslands. These different tenure systems are considered to have a significantly different impact on the conditions of grasslands ecosystems. The high temporal resolution of Sentinel-1 data allows for the monitoring of the signal variations of grasslands. Figure (5.6) shows the backscattering variation in VH and VV polarizations in commercial and communal grasslands in the study area during the drought and non-drought growing seasons. The signals of grasslands in VV backscattering were higher than in VH, and the change in the magnitude of the signal (between grasslands types commercial and communal and also between dates) was greater in VV than in VH, and was greater in commercial grasslands than in communal grasslands.

Figure (5.6) shows a wide range of grasslands backscattering variation in VH from the beginning of the growing season in September until the end of the season in March. This wide range is explained by the multiple scattering caused by the grasses stems. The signal variation of grasslands particularly in VH, comes from two mechanisms that dominate during the growth cycle of grasslands, double-bounce scattering, and volume scattering.

Temporal variations of the backscattering coefficients revealed the phenological changes of grasslands in the study area, which can be differentiated into three main phases; (a) *vegetative phase*: grasslands backscattering increases with time, it increases from low values (around −21 dB in VH and −15 dB in VV) to higher values (around -19 dB in VH, and −13 dB in VV). At the beginning of the season, the backscattering coefficient σ0 is low since the fields are dry, then the incident radar signal is distributed. Only a small proportion of the emitted energy is backscattered to the sensor; the σ0 of the field is very low in both polarizations, followed by an increase in the backscattering that takes place after a rainfall event at the beginning of the growing season. Conversely, at the end of the vegetative phase, when the grasses grow in number and height, the signal was particularly strong, it can be explained by the high proportion of the emitted energy that returns to the sensor because of the double-bounce scattering, (b) *reproductive phase*: when grasses reach their maximum height, the panicles develop, the leaves change direction and the stem dries. From this phase until the end of the season, the σ0 decreases. However, there is a slight increase in σ0 during the reproductive phase, it can be explained by the increase in the proportion of the transmitted signal due to the increased volume of vegetation, and (c) *maturation phase*: during this period, the grasses enter the senescence phase, the leaves and stem continue to dry, the plants move towards the ground, and the σ0 decreased in both VH and VV. This change is related to the decrease in the water content of the grasses which affects σ0, since dried plants have a lower dielectric constant.

3.3. Relationship between Sentinel-1 SAR data and Landsat-8 NDVI

Temporal analysis was conducted by correlating SAR backscattering (VH and VV) over communal and commercial grasslands in Eastern Cape with corresponding NDVI values. Spatial correlation was performed based on the mean values of SAR backscattering of each grassland type and the Landsat-8 NDVI accordingly for both drought and non-drought growing seasons.

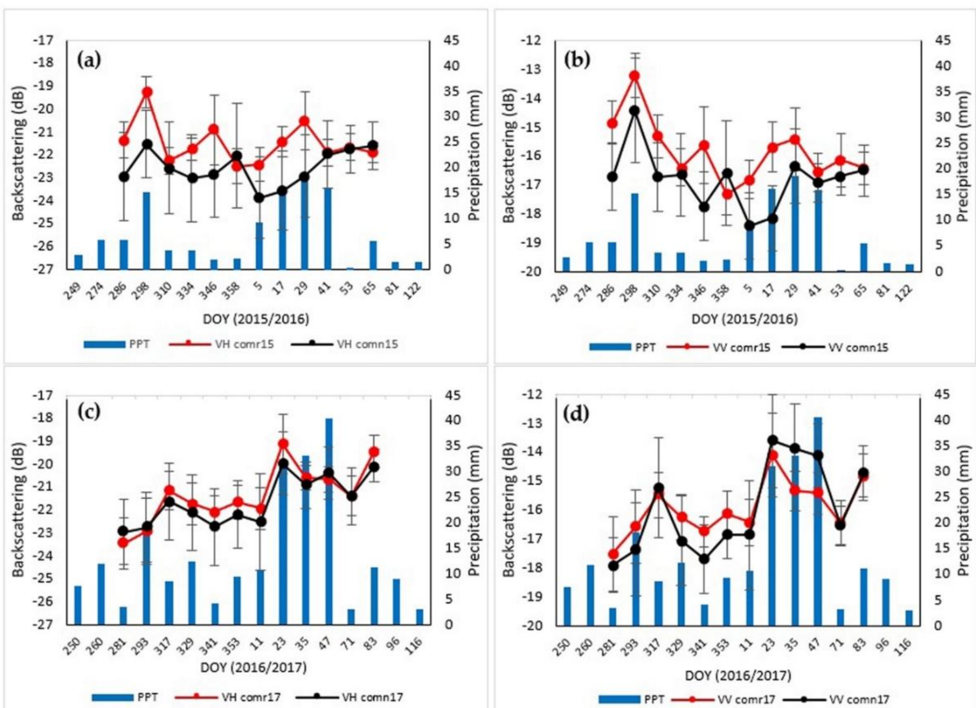

Figure 5.6. Backscattering coefficients of commercial and communal grasslands in the study area overlaid on precipitation data; (a) VH backscattering in 2015/2016, (b) VV backscattering in 2015/2016, (c) VH backscattering in 2016/2017, and (d) VV backscattering in 2016/2017. The x-axis of the figures indicates Julian days of the respective years.

The correlations between SAR backscattering coefficients and NDVI over the communal grasslands in the study area are presented in Figure (5.7). We found that, in the drought growing season, VH backscattering was positively correlated with NDVI (R^2 = 0.89) (Figure 5.7a). In contrast, in the non-drought season when biomass reached a high level, VH backscattering changed, and the correlation of VH backscattering against NDVI decreased (R^2 = 0.79) (Figure 5.7c). VV backscattering was positively correlated with NDVI in the drought season (R^2 = 0.66) (Figure 5.7b), which also decreased in the non-drought season (R^2 = 0.52) (Figure 5.7d). Results also showed that the correlation of VH backscattering with NDVI is higher than the correlation of VV backscattering with NDVI during both the drought and non-drought growing seasons (Figure 5.7).

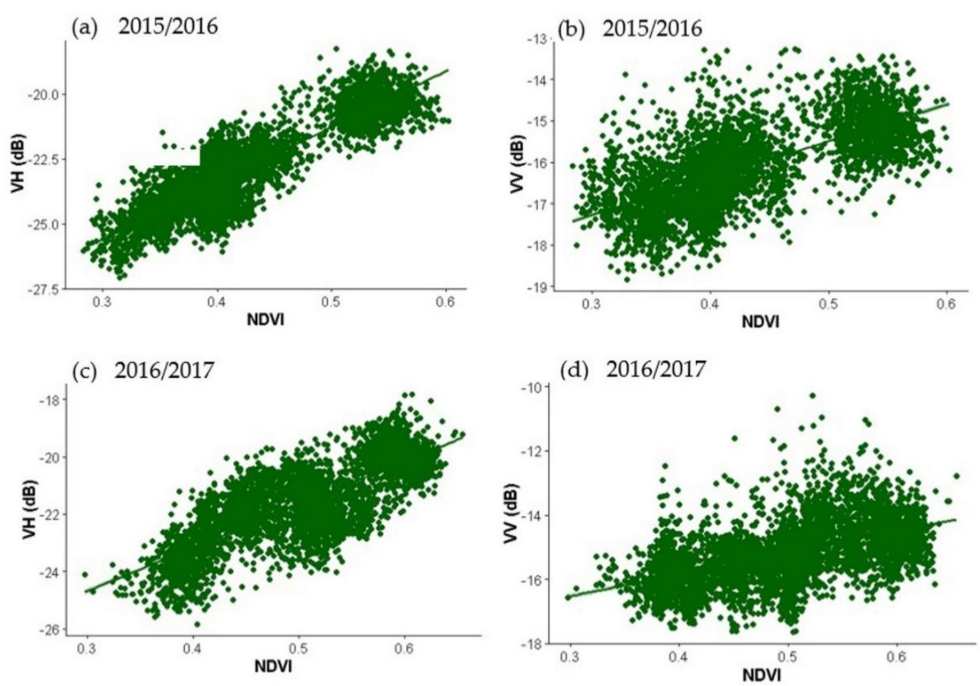

Figure 5.7. Correlation analysis between Sentinel-1 SAR data and NDVI over communal grasslands; (a) VH backscattering with NDVI during the drought season 2015/2016, (b) VV backscattering with NDVI, (c) VH backscattering with NDVI during the non-drought growing season 2016/2017, and (d) VV backscattering with NDVI.

The correlations between SAR backscattering coefficients (VH and VV) and NDVI over the commercial grasslands in the study area are presented in Figure (5.8). A positive correlation was found between SAR backscattering coefficients and NDVI in commercial grasslands with linear relationship. The correlation of VH backscattering with NDVI appeared higher in the drought season (R^2 = 0.65), and lower in the non-drought season (R^2 = 0.48). The correlation of VV backscattering with NDVI was also higher in the drought season (R^2 = 0.46) than in the non-drought growing season, which weakly correlated to NDVI (Figure 5.8). Similar to the correlations in communal grasslands, the correlation of VH backscattering was higher than the correlation of VV backscattering with NDVI. To compare the correlation results for both communal and commercial grasslands, the correlation between Sentinel-1 SAR backscattering for both VH and VV was higher in communal grasslands than in commercial grasslands with strong correlations for VH backscattering with NDVI and weaker correlation for VV backscattering with NDVI.

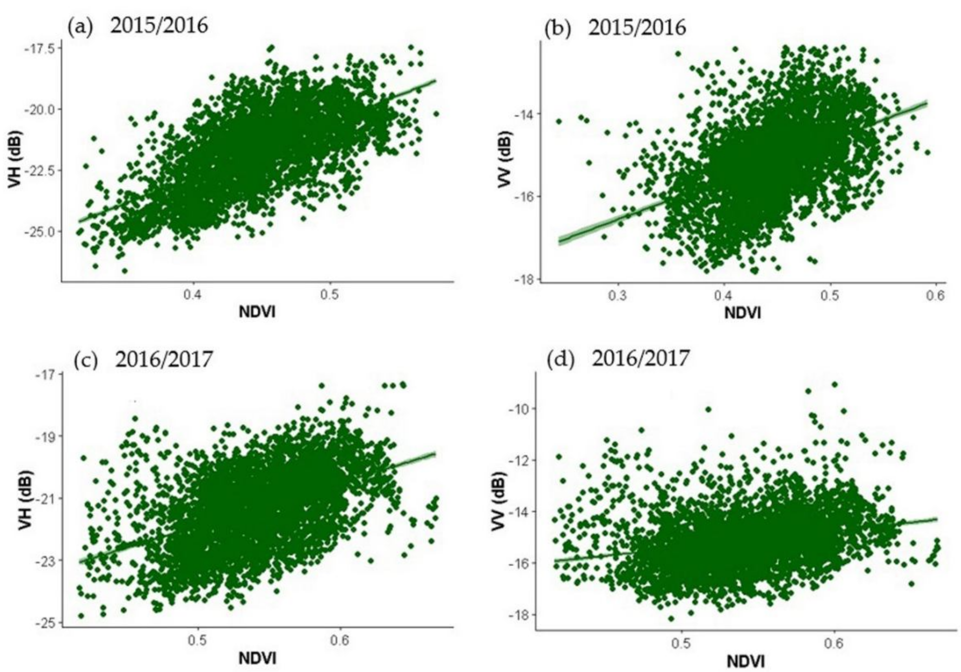

Figure 5.8. Correlation analysis between Sentinel-1 SAR data and NDVI over commercial grasslands; (a) VH backscattering with NDVI during the drought season 2015/2016, (b) VV backscattering with NDVI, (c) VH backscattering with NDVI during the non-drought season 2016/2017, and (d) VV backscattering with NDVI.

We compared the NDVI for commercial and communal grasslands in the study area during the last five years from 2013-2018. Results showed that, in most years, a single NDVI peak was observed during the growing seasons of grasslands, except for the growing season of 2015/2016 (the drought season), a double NDVI-peak was observed, which varied between commercial and communal grasslands (Figure 5.9). This change in the pattern of grasslands growth from single–peak to double-peak during the drought season could be explained by the less rainfall received and the increased mean temperature occurred during the drought season 2015/2016, which suppress the growth of grasslands during this period, and subsequently lead to a change in the pattern of the growing season of grasslands. Figure (5.9) also showed that communal grasslands are more affected by this impact more than commercial grasslands.

We compared the NDVI-precipitation dynamics between commercial and communal grasslands during the drought and non-drought growing seasons. The main active vegetation dynamics in grasslands can be observed between September and March/April, which closely corresponds to the precipitation rates, which increase in October and drop in April (Figure 5.10). In the drought season 2015/206, commercial grasslands started growing at the beginning of the season earlier than communal grasslands which received less amount of rainfall, leading to a delay in the onset of the growing season in communal grasslands. In the non-drought season 2016/2017, commercial grasslands received more rainfall and started the growing season earlier than in the drought year. Communal grasslands received amount of rainfall more than the amount received during the drought season, and less than the amount of rainfall received by commercial grasslands (Figure 5.10).

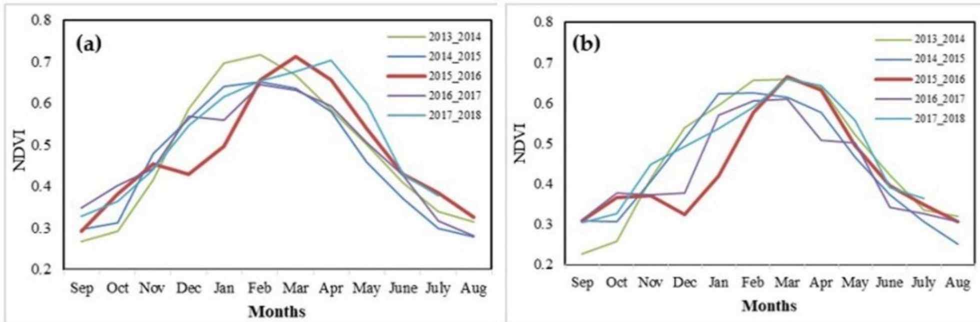

Figure 5.9. Annual normalized difference vegetation index (NDVI) for (a) commercial grasslands, and (b) communal grasslands in Eastern Cape during the last 5 years. The 2015/2016 growing season is highlighted with bold red line.

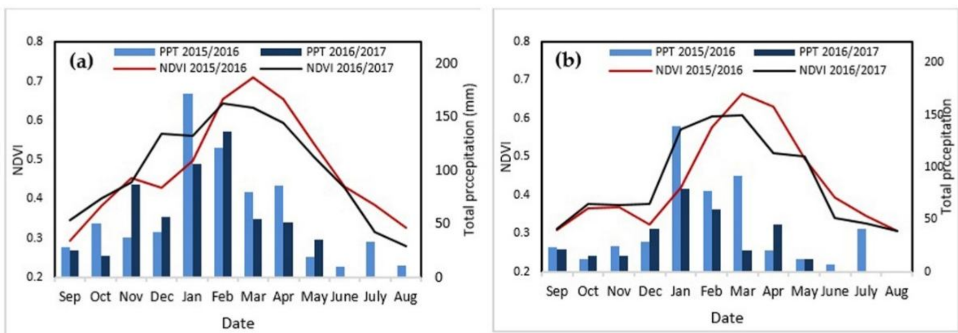

Figure 5.10. Annual normalized difference vegetation index (NDVI) for (a) commercial grasslands, and (b) communal grasslands in the study area overlaid on total precipitation during the drought 2015/2016 and non-drought 2016/2017 growing seasons.

3.4. Impact of drought on communal and commercial grasslands

Figure (5.11) shows the results of the regression analysis of Sentinel-1 SAR data in communal and commercial grasslands in Eastern Cape during the two years. Results showed that the drought season has a significant influence on the VH backscattering for both communal and commercial grasslands, with a higher impact on communal grasslands than commercial grasslands. There is a negative association between the drought season over communal grasslands and VH backscattering (β = - 0.69, p < 0.05) (Figure 5.11a). The variation between the impacts of drought on communal and commercial grasslands is very clear in VV than in VH backscattering, with a higher impact on communal grasslands than in commercial grasslands. A negative association between the drought season over communal grasslands and VV backscattering was detected (β = - 0.90, $p < 0.01$) (Figure 5.11b). Our results also showed that the drought season has a significant influence on NDVI values, there is a negative association between the drought season and NDVI (β = - 0.68, $p < 0.01$), and a negative association between communal grasslands and NDVI (β = - 0.69, $p < 0.05$) (Figure 5.11c).

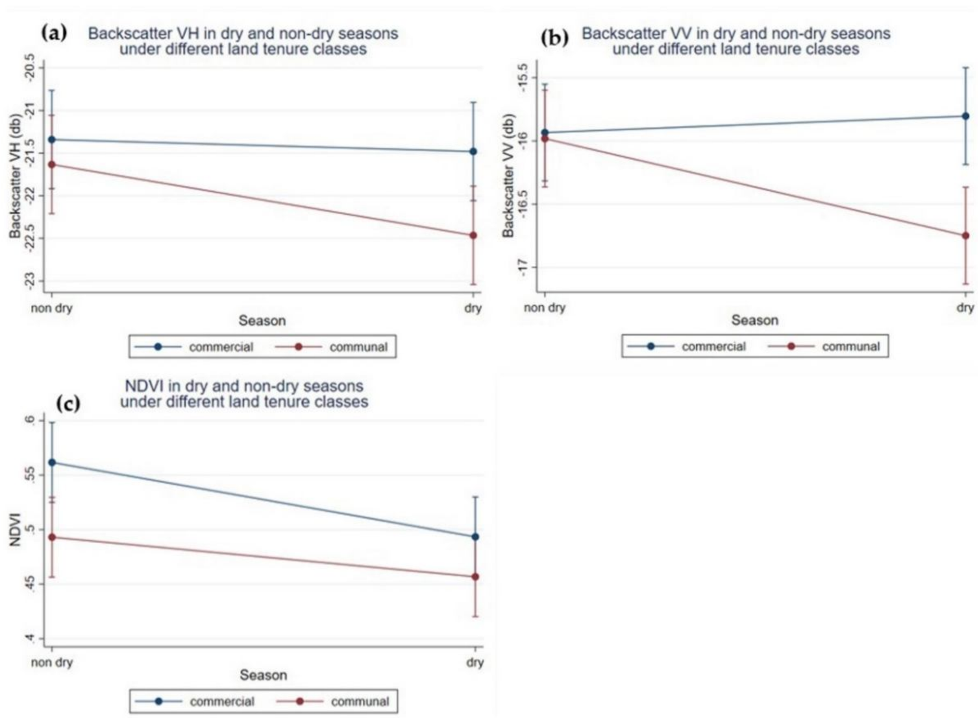

Figure 5.11. Results of the regression analysis in communal and commercial grasslands during the drought and non-drought growing seasons; (a) VH backscattering, (b) VV backscattering, and (c) NDVI. Probability values are significant at ($p < 0.01$) for the three models.

4. DISCUSSION

In this study, we investigated the potential of multi-temporal Sentinel-1 SAR data integrated with field observations and climatic data for monitoring grasslands and detection of the impact of drought on communal and commercial grasslands in Eastern Cape Province. Several studies used SAR data for vegetation mapping and monitoring, but SAR applications for grasslands monitoring have been much less relative to optical data. The reasons for this include limited availability of SAR data, and complex data structures relative to optical data. This condition changed after the launch of Sentinel-1 SAR data (Torres *et al*., 2012), which provided high spatial resolution (< 30 m), and temporally frequent SAR data at the scales needed to support grasslands monitoring, and addressing the impact of climate change on vegetation dynamics in grasslands.

Studies that used SAR data have detailed vegetation backscattering responses for varying wavelengths, polarizations, incidence angles, scales, and field properties. SAR backscattering signal differs at various bands. SAR data with C-band (wavelength of ≃ 5 cm) was used more often for the monitoring of agricultural crops and grasslands due to the relatively small size of plants (McNairn *et al*., 2009; Wiseman *et al*., 2014). In case of low frequency (C-band), the total backscattering is a combination of contributions from soil and vegetation layer, while in case of high frequency; the total backscattering is the contribution of vegetation layer only (Wang *et al*., 2013).

Results of the current study demonstrated the potential of multi-temporal Sentinel-1 SAR data for monitoring the spatio-temporal variations in grasslands, and retrieval of the biophysical parameters of grasslands. Results showed that the signals of grasslands in VV backscattering were higher than in VH backscattering. Our results are in agreement with several studies used SAR data for monitoring of agricultural crops and grasslands, and focused on the analysis of SAR backscattering intensity and polarimetric parameters; for example, McNeill *et al*. (2010), found that TerraSAR-X HH+HV backscatter performed the best among all polarization combinations in pasture areas in New Zealand. Voormansik *et al*. (2013) analyzed dual polarimetric signatures of agricultural grasslands at X-band, indicating several potentially promising polarimetric parameters for detecting mowing events.

We used multi-temporal NDVI data extracted from Landsat-8 to contribute to our understanding of the ability of SAR data for monitoring of grasslands and detection of the impact of drought. Our results revealed a positive correlation between SAR backscattering and NDVI in both communal and commercial grasslands, with a higher correlation of VH backscattering with NDVI in communal grasslands, this is probably related to the fact that VH signal has more capability than optical indices to estimate properties of grass of high biomass. Meanwhile, fluctuation of VH backscattering was also largely attributed to rainfall. Water on leaves after rainfall can cause substantial change of the backscattering coefficient (Wang *et al*., 2013), this in agreement with Ali *et al*. (2013), they used COSMO-SkyMed SAR data in a study of nature conservation sites in the Alpine region, and found that the potential of VV backscatter to detect grazing or mowing activities was undermined by rainfall events, which made backscatter signal increase sharply.

During the last decade, the frequency and impact of natural disasters in the farming community in South Africa have increased significantly, and the most common type of disaster is drought. Data from the Centre for Research on the Epidemiology of Disaster show that drought is a major disaster in South Africa in terms of the number of people affected and total economic loss (Ngaka, 2012). Our results revealed seasonal dynamics of grasslands in the study area and provided insights into explaining the response of grasslands in communal and commercial grasslands to the changes in precipitation and the impact of drought. Other studies such as Graw *et al*. (2017), used optical data only, and compared the precipitation-vegetation dynamics in croplands using Vegetation Condition Index (VCI) based on the MODIS EVI, indicated other drivers for productivity change and drought impact besides rainfall.

Results of the regression analysis in the current study revealed that communal grasslands are more affected by the impact of drought than commercial grasslands. People living in rural areas and resource-poor farmers in communal grasslands are often cited as more vulnerable to the impact of drought

(Pelser *et al*., 2005), their suffering and vulnerability are often exacerbated by a lack of progress in effective drought management, while in commercial grasslands, management activities including; organizing the livestock grazing, firing, resting the fields, and grasslands mowing, were able to improve the growing conditions of commercial grasslands, reduced the impact of drought stress, and subsequently increased the grasslands resilience and productivity.

Limitations of the current study include the short time series of SAR data, explained by the lack of Sentinel-1 data before 2015. In future work, we will combine multi-source SAR data for better prediction of the impact of drought on grasslands. In addition, Sentinel-2 optical data will be integrated with Sentinel-1 data in future work.

5. CONCLUSION

Grasslands are one of the main biomes in Eastern Cape Province; better management of grasslands is of great importance for profitability and sustainability. This study focused on investigating the potential of using multi-temporal dual-polarimetric SAR data of Sentinel-1 for monitoring and detecting the impact of drought on communal and commercial grasslands in Eastern Cape. The availability of multi-temporal SAR data with high temporal and spatial resolution allows for the analysis of seasonal vegetation dynamics in grasslands and retrieval of the biophysical parameters. Correlation between VH backscattering and NDVI was higher than VV backscattering and was higher in communal grasslands over commercial grasslands. Findings presented in this study revealed that communal grasslands are more affected by drought than commercial grasslands. Our results demonstrated the feasibility of using multi-temporal SAR data of Sentinel-1 for grasslands monitoring and detection of the impact of drought on communal and commercial grasslands.

Chapter 6

The Potential of Sentinel-1 InSAR coherence for Grasslands Monitoring

This chapter is based on ***Abdel-Hamid, A.****, Dubovyk, O., and Greve, K. 2019. The potential of Sentinel-1 InSAR coherence for grasslands monitoring in Eastern Cape, South Africa [Manuscript].*

ABSTRACT

This study evaluates the potential of the repeat-pass synthetic aperture radar interferometry (InSAR) coherence for grasslands monitoring in Eastern Cape Province, in South Africa. We used 12 pairs of InSAR data in the Interferometric Wide swath mode (IW), in VV-polarization (with different spatial baseline B⊥ and different temporal repeat intervals between the subsequent acquisitions), covering grasslands in the study area during two growing seasons; drought season (2015/2016) and non-drought season (2016/2017). Results show that non-drought season has higher variability in the coherence between the different regions of interest (ROIs) than the drought season and higher variability in the backscattering coefficient. Based on our results, we conclude that InSAR-based data have shown potential for grasslands monitoring, and the regularity of Sentinel-1 data is well suited for InSAR applications. However, the potential to separate grasslands from other vegetation categories appears to be limited with longer temporal baselines of 12 days intervals using only Sentinel-1A data. This potential will be improved with the 6 days intervals that will become available with Sentinel-1B in the study area.

Keywords: Grasslands, Sentinel-1; InSAR coherence, Eastern Cape; South Africa.

1. INTRODUCTION

Grasslands cover more than 40% of the Earth's land surface and are widely used for livestock grazing and fodder production, thereby contributing to global food production in major ways (FAO, 2006). They are generally located in drier regions (arid and semi-arid environment) and experience high inter-annual variability in precipitation, which in turn, is a key driver of grasslands production and resource deterioration and recovery (McKeon *et al*., 2004; Cobon *et al*., 2017). Grasslands are a major component of the natural vegetation in South Africa, covering almost one-third of the country's land surface, with a biome comprising 295,233 km^2 of the central region of the country. They extend across the boundaries of seven provinces, spanning a complex array of socio-economic situations and land use contexts. The interface between grasslands and other biomes contributes substantially to their floristic and faunal diversity and to the important role they play in the agricultural economy (Palmer and Ainslie, 2005).

Grassland ecosystems support human, fauna and flora populations by providing numerous goods and services such as the provision of forage for livestock, wildlife habitats, and biodiversity conservation (White *et al*., 2000). Additionally, grasslands are the largest terrestrial carbon sink after forests (Derner and Schuman, 2007) and they play a vital role in regulating the global carbon cycle (Franzluebbers, 2010). However, the ecosystem services provided by grasslands, they are facing several pressures due to the impact of unsustainable land management practices and climate change. At least 40% of the grassland biome in South Africa has been irreversibly modified, and nearly 60% of the remaining grassland areas are classified as threatened, and subsequently, these ecosystems are losing vital aspects of their composition, structure, and functioning (Palmer and Ainslie, 2005). This makes it essential to monitor the grasslands' status on a repeated and regular basis.

Drought has been one of the major factors influencing vegetation dynamics in grasslands (Cook *et al*., 2007), causing substantial social and economic consequences (Wilhite and Buchanan-Smith, 2005). Grasslands productivity is largely controlled by the amount and timing of precipitation and corresponding seasonal fluctuations in soil water content (Parton *et al*., 2012). Temperature is also an important regulator of grassland productivity (Liu *et al*., 2006).

In 2015/2016, South Africa experienced combined effects of a severe drought and a strong El Niño event. National authorities qualified it as the worst drought in 23 years (Vogel and van Zyl, 2016). This severe drought resulted in significant declines in the harvest, in particular during 2016, and seriously depleted the water reserves. The drought has also had a ripple effect on the country's economy that contributed to a decline in Gross Domestic Product (Baudoin *et al*., 2017). The socio-economic effects of drought across the region are evident, extensive and have negatively affected key sectors of the economy, such as agriculture and food security (Baudoin *et al*., 2017).

Assessment of the state of grasslands and their dynamics generally relies on the use of optical satellite data. The use of methods based on time series analysis is preferred due to temporal differences caused by plant phenology and management practices. However, the availability of optical data throughout the growing season is limited due to cloud cover, which stimulates studies of other remote sensing data such as Synthetic Aperture Radar (SAR) for monitoring of grasslands (Lang and McCarty, 2008).

Studies that make use of SAR data for vegetation monitoring has mostly focused on SAR backscattering. SAR interferometry (InSAR) was less investigated. InSAR consists of correlating two images acquired from two positions in space slightly separated from each other; the distance between the satellite positions is referred to as the interferometric baseline (Santoro *et al*., 2018). InSAR coherence depends on the temporal separation between image acquisitions (repeat-pass interval) and the spatial distance between the satellites (the length of the baseline). Being sensitive to elevation changes, InSAR captures the three-dimensional structure in its observables; both the interferometric phase and the coherence are related to the elevation of the scattering objects and the density of the vegetation. These observables are, therefore, potentially more suited to the retrieval of biophysical parameters than the intensity of the backscattered signal, since the vertical properties of the vegetation structure are not represented in the backscatter observation (Santoro *et al*., 2018).

InSAR coherence with a range of temporal baselines has shown promising results in surface parameter inversion. Seasonal variation of coherence has been investigated to understand environmental changes over various land covers (Wei and Sandwell, 2010; Ahmed *et al*., 2011). In areas covered by vegetation, the backscatter includes contributions from both the ground surface and the above vegetation canopy, with the balance between the two depending on the penetration capability of the radar signal with respect to the structure, geometry, and density of the vegetation (Kornelsen and Coulibaly, 2013). More recently, Copernicus Sentinel-1 constellation has started to collect SAR imagery in interferometric wide swath mode (IW) with a repeat cycle of 12 days for each satellite, which offers an opportunity for grasslands monitoring based on a dense time series of InSAR data.

The main objective of this study focused on exploring the potential of InSAR coherence of Sentinel-1 for monitoring of communal and commercial grasslands in Eastern Cape under drought and non-drought conditions and investigating the relationship between backscattering intensity and InSAR coherence concerning the potential for grasslands monitoring.

2. DATA AND METHODS

2.1. Study Area

The study area is located in Eastern Cape Province, it is the second-largest province in South Africa, with topographic and climatic complexity and diversity leading to a rich mixture of floristic elements (Clark *et al*., 2009). The mountainous region in the north of the province forms part of the Great Escarpment Mountains and dominated primarily by grasslands with large patches of forest on the south (Hoare *et al*., 2006). The climatic conditions in Eastern Cape vary from mild warm temperatures to subtropical conditions at the coast. Droughts can occur throughout the year, but grasslands are particularly vulnerable to droughts during the growing season in the summer, which mainly goes from September to March. The precipitation regime is characterized by a large variability at various time scales; from intra-seasonal, through inter-annual to decadal and multi-decadal (Kane, 2009). Land ownership in the study area is divided into two tenure systems; communal and commercial systems. In the current study, we focused on the Sakhisizwe municipality in Eastern Cape Province. Two main study locations were selected, covering the two main grassland tenure systems; communal and commercial grasslands (Figure 6.1).

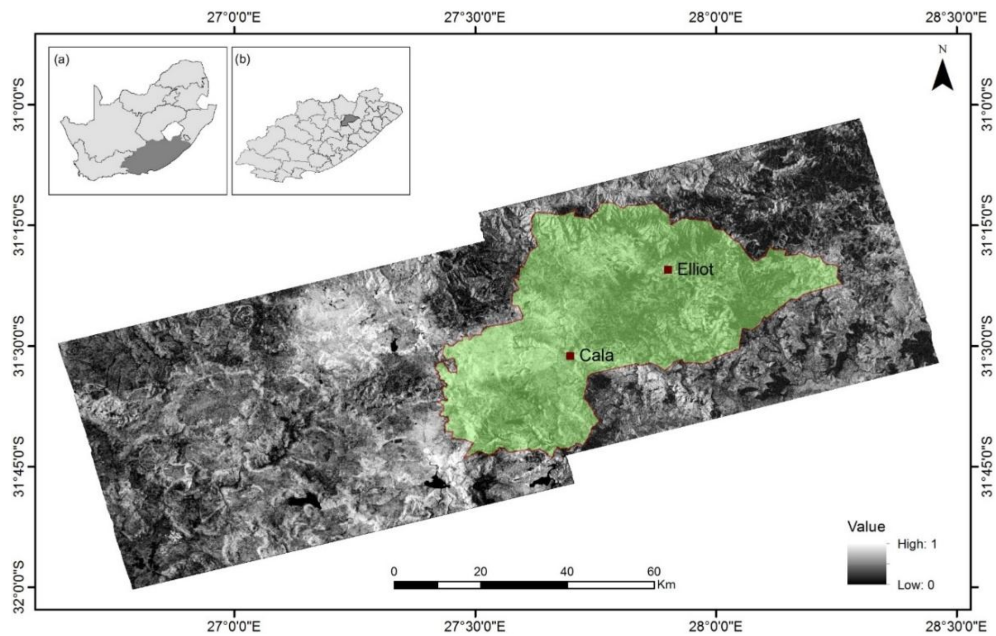

Figure 6.1. Location of the study area in Eastern Cape Province showing the Sakhisizwe municipality with the two main towns; Cala and Elliot, overlaid on the processed InSAR data.

2.2. Data Sources

Sentinel-1 is a C-band synthetic aperture radar (SAR) satellite operating at a Centre frequency of 5.405 GHz (wavelength ~5.54 cm) and consists of a constellation of two satellites (Sentinel-1A and Sentinel-1B). Jointly they provide a nominal 6-day repeat cycle allowing for continuous monitoring of land surfaces.

It operates in four image modes with various observation strategies, swath widths, and spatial resolutions, namely; the Strip Map mode (SM), Interferometric Wide swath mode (IW), Extra Wide swath mode (EW), and Wave swath mode (WV) (Torres *et al*., 2012). Sentinel-1 SAR data covering the study area in Eastern Cape Province was acquired from the European Space Agency (ESA), throughout two growing seasons (2015/2016 and 2016/2017).

We acquired data in the Interferometric Wide swath mode (IW), in dual-polarization VV/VH, single look complex format (SLC), and product level 1. The IW SLC product contains one image per sub-swath, per polarization channel, for a total of three or six images. Each sub-swath image consists of a series of bursts, where each burst was processed as a separate SLC image. The time span between acquisitions was 12 days in ascending orbit. Two sub-swaths were included in the current study, *i.e.*, IW2 and IW3. Precise dates of the different InSAR pairs are provided in Tables (6.1 and 6.2).

Table 6.1. Sentinel-1 InSAR pairs used in the current study for calculating the coherence during the drought season (2015/2016).

Pair	Date (2015/2016)	Mst/Slv	Track	Orbit	B. prep. [m]	B. temp. [days]
P1	2015/10/13 - 2015/10/25	S / M	14	8136 - 8311	-38.63	12
P2	2015/12/12 - 2016/01/05	S / M	14	9011 - 9361	-124.48	24
P3	2016/01/05 - 2016/01/29	S / M	14	9361 - 9711	-50.71	24
P4	2016/01/05 - 2016/02/22	M / S	14	9361 - 10061	-76.48	-48
P5	2016/01/05 - 2016/03/05	M / S	14	9361 - 10236	-29.36	-60
P6	2016/01/05 - 2016/03/17	S / M	14	9361 - 10411	-45.29	72
P7	2016/01/29 - 2016/02/22	M / S	14	9711 - 10061	-126.75	-24
P8	2016/01/29 - 2016/03/05	M / S	14	9711 - 10236	-79.97	-36
P9	2016/01/29 - 2016/03/17	M / S	14	9711 - 10411	-7.04	-48
P10	2016/02/22 - 2016/03/05	S / M	14	10061 - 10236	-47.22	12
P11	2016/02/22 - 2016/03/17	S / M	14	10061 - 10411	-121.69	24
P12	2016/03/05 - 2016/03/17	S / M	14	10236 - 10411	-74.65	12

B. prep. = Baseline perpendicular ($B\perp$), the spatial distance between the two satellites, and **B. temp.** = Baseline temporal, the temporal separation between image acquisitions, **Mst** = master scene, **Slv** = slave scene.

Table 6.2. Sentinel-1 InSAR pairs used in the current study for calculating the coherence during the non-drought the season (2016/2017).

Pair	Date (2016/2017) IW3	Mst/Slv	Track	Orbit	B. prep. [m]	B. temp. [days]
P1	2016/10/07 - 2016/10/19	S / M	14	13386 - 13561	-52.08	12
P2	2016/10/19 - 2016/10/31	M / S	14	13561 - 13736	-104.73	-12
P3	2016/10/31 - 2016/11/12	S / M	14	13736 - 13911	-53.45	12
P4	2016/11/12 - 2016/11/24	M / S	14	13911 - 14086	6.98	-12
P5	2016/11/24 - 2016/12/06	S / M	14	14086 - 14261	12.67	12
P6	2016/12/06 - 2016/12/18	M / S	14	14261 - 14436	-17.43	-12
P7	2016/12/18 - 2017/01/23	S / M	14	14436 - 14961	-56.82	36
P8	2017/01/23 - 2017/02/04	M / S	14	14961 - 15136	6.58	-12
P9	2017/02/04 - 2017/02/16	M / S	14	15136 - 15311	29.59	-12
P10	2017/02/16 - 2017/02/28	M / S	14	15311 - 15486	-30.90	-12
P11	2017/02/28 - 2017/03/12	M / S	14	15486 - 15661	-72.16	-12
P12	2017/03/12 - 2017/03/24	S / M	14	15661 - 15836	-78.76	12

B. prep. = Baseline perpendicular ($B\perp$), the spatial distance between the two satellites, and **B. temp.** = Baseline temporal, the temporal separation between image acquisitions, **Mst** = master scene, **Slv** = slave scene.

Changes in grasslands in the study areas were interpreted in the context of meteorological conditions. Meteorological data covering the study area in Eastern Cape Province were obtained from the South African Weather Service Organization. The original climatic data consist of daily records of precipitation and temperature from 2014 to 2017. Land cover information was obtained based on the South African National Land-cover dataset produced by GEOTERRAIMAGE in 2013–2014, which was generated with 600 multi-seasonal 30 m Landsat-8 multispectral images, and used in the current study to extract the grasslands layer (GEOTERRAIMAGE, 2014). In addition, field measurements were collected during a field expedition in the study area in October 2017. Fieldwork included a description of the test sites in the two main study locations, including 12 test sites in each grassland type (communal and commercial grasslands), and collection of GPS-points for validation of the remote sensing data analysis. Identification of the two grassland types was also carried out during the fieldwork in the study area.

2.3. Pre-Processing and Data Analysis

2.3.1. InSAR Coherence Estimation

Pre-processing of the Interferometric data included the selection of the suitable SLC pairs for InSAR data analysis. Splitting of Sentinel-1 (S1) data into sub-swaths levels covering the study area (IW2 and IW3), selecting VV polarization for the InSAR coherence analysis, applying a precise orbit file, followed by co-registration to the sub-pixel accuracy using the S1 TOPS Co-registration algorithm. After the co-registration, coherence was calculated for each image pair according to:

$$\gamma = \frac{|\langle s_1 s_2^* \rangle|}{\sqrt{\langle s_1 s_1^* \rangle \langle s_2 s_2^* \rangle}} \qquad (1)$$

Where γ is the coherence value at pixel location (x,y), s_1 and s_2 are the complex values of SLC images 1 and 2 at pixel location (x,y), and * stands for the complex conjugation. Additionally, backscattering coefficients (σ°) for VV polarization were calculated for each of the Sentinel-1 images. Both backscatter intensity images and coherence were geocoded to the WGS84 with a pixel size of 30m x 30m in the Universal Transverse Mercator (UTM) projection Zone 35S. Processing of SAR data was performed using the ESA SNAP toolbox (version 6.0). Figure (6.2) shows examples of the different data used in the current study.

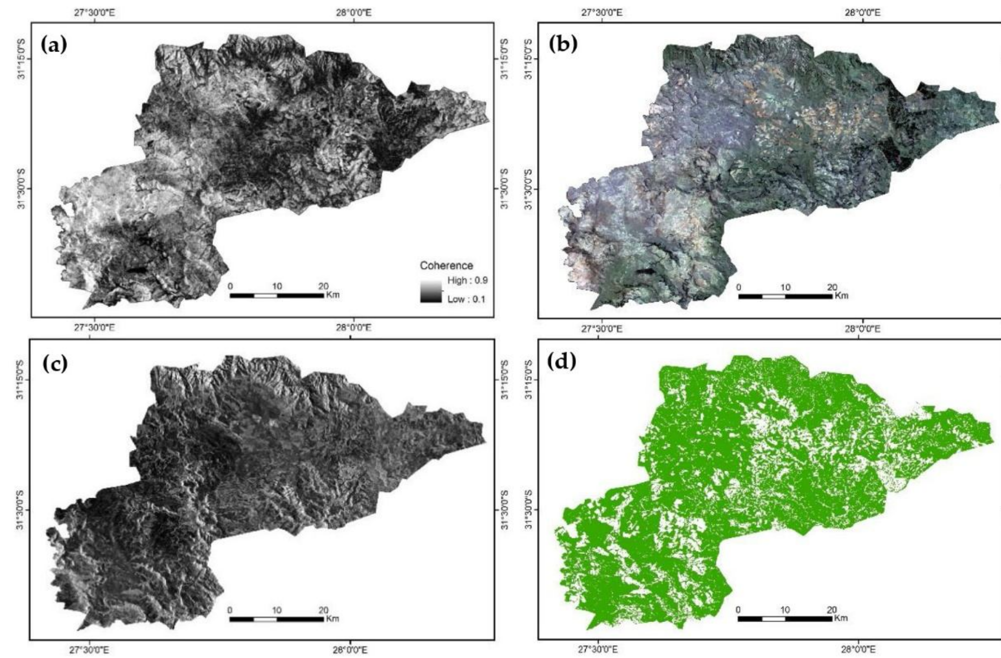

Figure 6.2. (a) Calculated coherence (pair 20151013-20151025), (b) Landsat-8 composite (4,3,2) (c) VV backscattering coefficient, and (d) grasslands layer extracted from the land cover dataset.

2.3.2. Multi-temporal analysis of InSAR coherence

We selected 12 regions of interest (ROIs) in each study location for grasslands monitoring during two growing seasons; drought season (2015/2016), and non-drought season (2016/2017). These ROIs represent different fields within the communal and commercial grasslands that were likely to exhibit different seasonal variations in the backscatter and coherence. We calculated the mean backscatter intensity and coherence values over each ROI for every intensity and coherence image. We established a time series of the mean values, and finally, we compared SAR backscattering and InSAR coherence time series. Figure (6.3) provides an overview of the entire approach adopted in the current study.

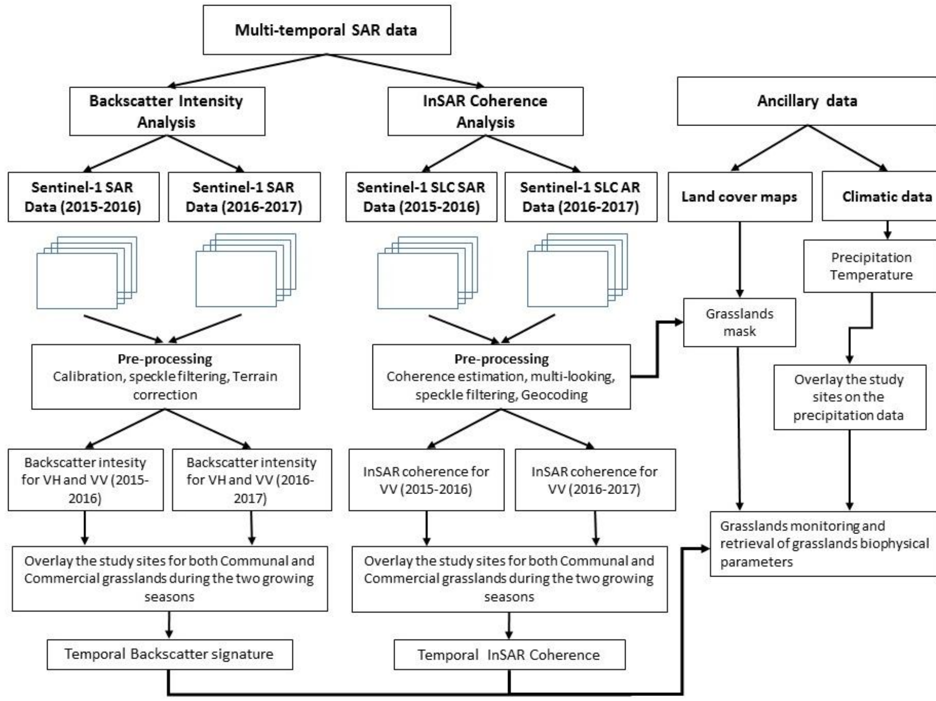

Figure 6.3. Flowchart of the methodology adopted in the current study.

3. RESULTS

3.1. InSAR Coherence Estimation

InSAR coherence γ is the complex correlation between two complex SAR images and consists of a phase and a magnitude component. The magnitude varies between 0 and 1, at which 0 refers to no correlation and 1 to perfect correlation. Figure (6.4) shows the calculated InSAR coherence covering selected test sites in both communal and commercial grasslands in the study area.

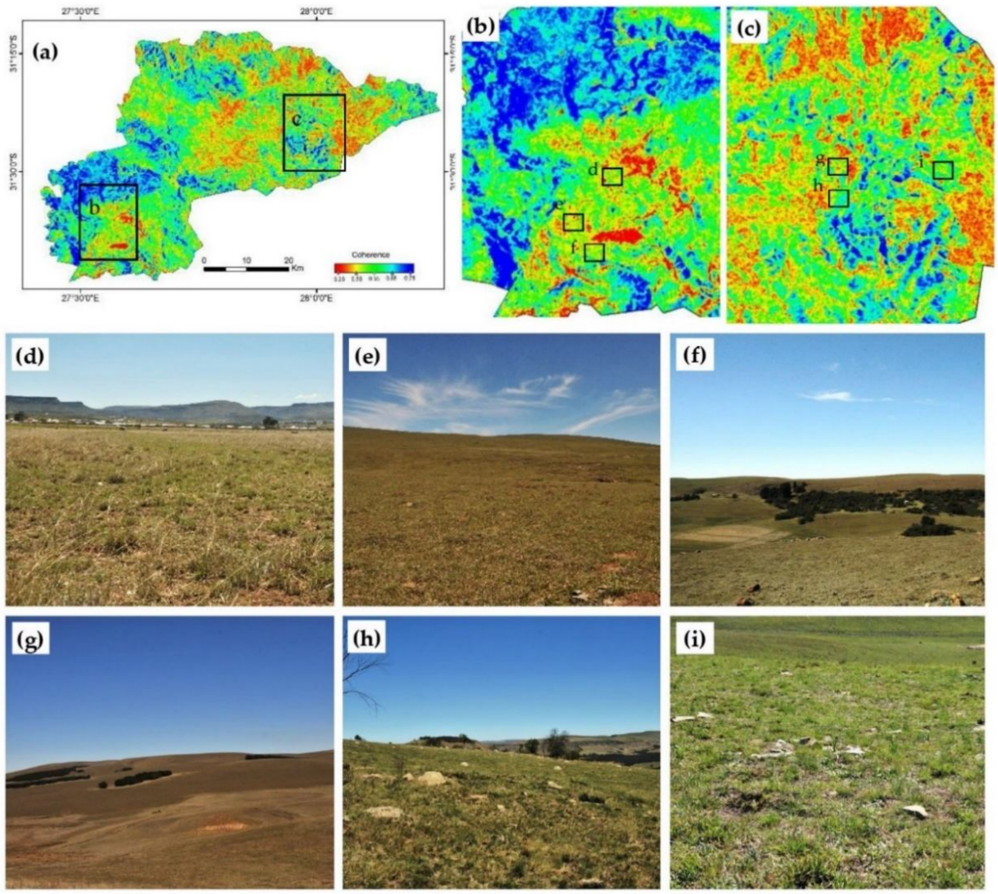

Figure 6.4. InSAR coherence analysis covering different test sites in the communal and commercial grasslands in the study area, (a) Calculated coherence from the InSAR pair (20151013-20151025), (b) subset in communal grasslands, (c) subset in commercial grasslands, (d, e, f) different test sites in communal grasslands, and (g, h, i) different test sites in commercial grasslands.

3.2. Multi-temporal analysis of InSAR coherence

Figure (6.5) shows the results of the multi-temporal analysis of InSAR coherence over communal and commercial grasslands under drought and non-drought conditions. Results showed the variations in the magnitude of coherence between communal and commercial grasslands during the two studied growing seasons. The coherence during the non-drought season (2016/2017) was higher than during the drought season (2015/2016). In addition, the magnitude of the coherence in communal grasslands was higher than in commercial grasslands. The variability of the coherence in communal grasslands was higher than in the commercial grasslands during the drought season. This situation changed during the non-drought season, to be less than the variability in commercial grasslands. Results also showed that the coherence was lower over grasslands at the longer temporal baseline as compared to the minimum intervals (12-days).

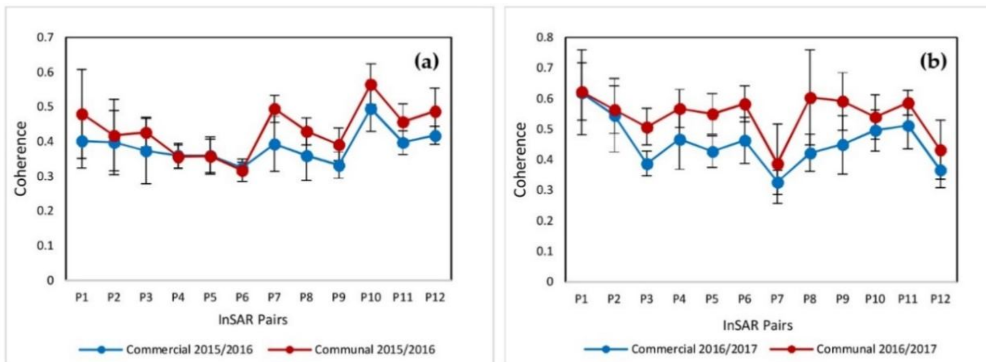

Figure 6.5. InSAR coherence analysis over communal and commercial grasslands in Eastern Cape during, (a) drought season, and (b) non-drought season.

3.3. Comparing SAR backscattering and InSAR Coherence time series

Figure (6.6) shows the comparison between SAR backscattering and InSAR coherence time series over communal and commercial grasslands in the study area during the two studied growing seasons. The coherence generally revealed high variability between communal and commercial grasslands. The non-drought season revealed higher variability in the coherence between ROIs than the drought season, and higher variability than the backscattering coefficient. Commercial grasslands revealed the highest variability in the coherence (between 0.29 and 0.83) and at the same time the highest coherence values (0.83), followed by communal grasslands (between 0.27 and 0.71), with the highest coherence values (0.71) during the non-drought season.

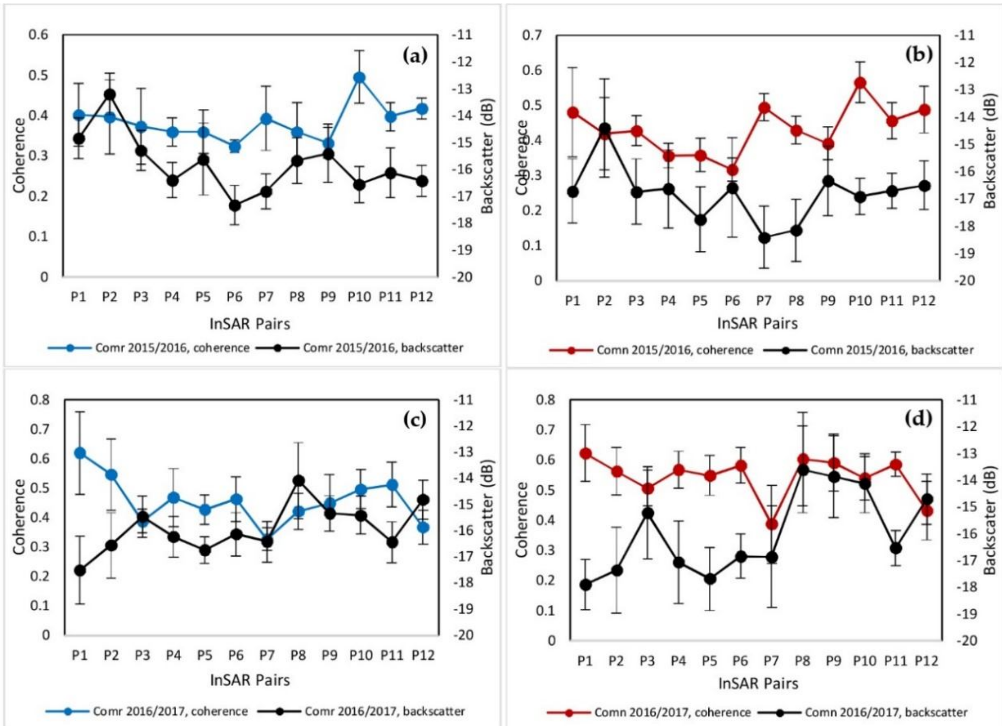

Figure 6.6. Comparing SAR backscattering and InSAR coherence over grasslands in Eastern Cape, (a-b) commercial and communal grasslands during the drought season, and (c-d) commercial and communal grasslands during the non-drought season.

Temporal variations of the backscattering coefficient and coherence revealed the phenological changes of grasslands in the study area. At the beginning of the drought season, the backscattering coefficient was low since the fields are dry, and thus, the incident radar signal was reflected away from the sensor. Only a small proportion of the emitted energy was backscattered to the sensor. This was followed by an increase in the backscattering after a rainfall event. On the other side, the coherence gradually decreased over the first part of the growing season (down ~ 0.2) until the onset of the vegetative phase. Following the onset of the vegetative phase, the reduction in the coherence observed over grasslands during this period coincided with the change in the backscatter.

When the grasses reach their maximum height, the leaves change direction and the stem dries leading to a decrease in the backscattering. However, there is a slight increase in the backscattering during this period that can be explained by the increase in the proportion of the transmitted signal due to the increased volume of vegetation. The decrease in coherence is likely to be due to the phenological changes. Thus, Grasses enter the senescence phase, leaves and stems continue to dry, and plants move towards the ground, causing a decrease in the backscattering. This change is also related to the decrease in the water content of the grasses, which affects the backscatter since dried plants have a lower dielectric constant.

Additionally, we compared the multi-temporal InSAR coherence and the total precipitation during the drought and non-drought seasons over commercial and communal grasslands in the study area (Figure 6.7).

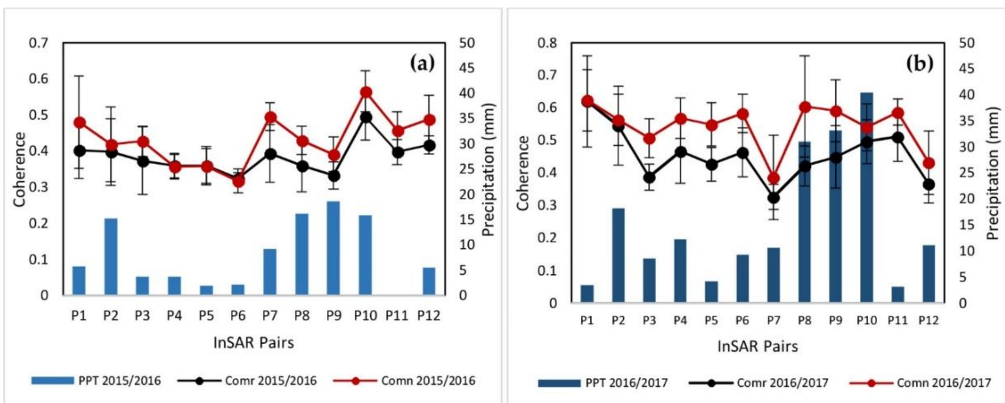

Figure 6.7. Comparing InSAR coherence over communal and commercial grasslands in the study area in relation to Precipitation data during; (a) drought season, and (b) non-drought season.

4. DISCUSSION

We investigated the potential of multi-temporal InSAR coherence of Sentinel-1 SAR data for grasslands monitoring in Eastern Cape Province, which could be an important tool in grassland management at different spatial and temporal scales. While remotely sensed data are often used to monitor ecosystems and biodiversity (Lang *et al*., 2013), Optical image time-series are generally more reliable for identifying vegetation types with a similar physiognomy (e.g. grasslands) (Schuster *et al*., 2015). However, optical data are unsuitable for monitoring of vegetation dynamics in grasslands, as they are limited to cloud-free periods (Claverie *et al*., 2012). Consequently, acquisition of optical time-series is unpredictable and not constant over time (Verbesselt *et al*., 2010). Conversely, Synthetic Aperture Radar (SAR) time-series are not sensitive to visibility conditions and can be acquired day or night (Schuster *et al*., 2015).

In recent years, SAR images have been used for vegetation monitoring and characterization (Schmitt *et al*., 2012; Betbeder *et al*., 2014). In most studies, the backscattering coefficients of radar signals are used for vegetation mapping and monitoring. SAR interferometry (InSAR) has been poorly explored for this purpose (Santoro *et al*., 2018). However, other investigations used SAR interferometry on grasslands (Zalite *et al*., 2016), and crops (Santoro *et al*., 2010) using X- and C-bands. They demonstrate the importance of using InSAR coherence for vegetation monitoring. InSAR potentially more suited to the retrieval of biophysical parameters than the intensity of the backscattered signal since the vertical properties of the vegetation structure are not represented in the backscatter observation (Santoro *et al*., 2018).

VV-polarization was selected in the current study because the signals of grasslands in VV backscattering were higher than in VH, and the change in the magnitude of the signal between grasslands types; communal and commercial and between the seasons; drought and non-drought, was greater in VV than in VH. Our results are in agreement with McNeill *et al*. (2010), they found that TerraSAR-X HH+HV backscatter performed the best among all polarization combinations in pasture areas in New Zealand. Voormansik *et al*. (2013) analyzed dual-polarimetric signatures of agricultural grasslands at X-band, indicating several potentially promising polarimetric parameters for detecting mowing events.

Non-drought season revealed higher variability in the coherence between ROIs than the drought season, and higher variability in the backscattering coefficient. InSAR coherence is sensitive to the changes in surface backscattering, which is dominated by the surface dielectric constant and roughness on the scale of the radar wavelength (Luo *et al*., 2001; Rocca, 2007; Simard *et al*., 2012). Temporal coherence can be influenced by temporal variations of surface backscattering due to changes in soil moisture, surface roughness, and vegetation biomass (Zhang *et al*., 2008; Lavalle *et al*., 2012).

The signal loss due to insufficient phase coherence between SAR datasets is one of the main limitations of InSAR coherence analysis. This phase coherence over time indicates the quality of the interferometric phase. The main sources of the loss of coherence or decorrelation are; temporal decorrelation, spatial decorrelation, volume decorrelation, geometric decorrelation, and thermal noise from the antenna (Zebker and Villasenor, 1992; Just and Bamler, 1994). Additionally, the perpendicular component $B\perp$ of the spatial baseline is of importance (Ackermann *et al*., 2012; Askne *et al*., 2013). We focused in this study on temporal decorrelation caused by changes in the scatterers over time (between the acquisitions). Obtaining InSAR results when processing higher radar frequency bands such as C-band is challenging across vegetated areas due to temporal decorrelation (Zebker and Villasenor, 1992). Generally, InSAR coherence decreases with increasing spatial and temporal baselines between two images (Wegmüller, 1998; Santoro *et al*., 2007). Temporal decorrelation is larger when shorter wavelengths are used.

Although the prediction of temporal decorrelation is extremely challenging, few studies have tried to simulate some components of the temporal decorrelation (Lavalle *et al*., 2012). A recent investigation by Morishita and Hanssen (2015) on pasture using repeat-pass multi-frequency SAR interferometry tried to analyze and develop a temporal decorrelation model. Ali *et al*., (2017) focused on retrieval of grassland biophysical parameters and management practices. Zalite *et al*. (2016) showed that even in case of 1-day temporal baseline, the interferometric coherence was shown to decrease because of an increased proportion of temporal decorrelation over vegetated areas (Askne *et al*., 2003; Santoro *et al*., 2007).

Results revealed the variations in the total precipitation between the two study locations. During the drought season, both communal and commercial grasslands received less precipitation compared to the non-drought season, which explains why the non-drought season had higher variability in the coherence than the drought season. Simard *et al*. (2012) found precipitation events to be the main cause of temporal decorrelation using fully-polarimetric airborne L-band acquisitions over forested landscapes with up to nine-day temporal baselines. Limitations of the current study include the short time series of Sentinel-1 data, explained by the lack of S1 data before 2015. In future work, we will compare multi-source InSAR data from different sensors with different frequencies for better monitoring of grasslands under drought and non-drought conditions.

5. CONCLUSION

In this study, we investigated the potential of Sentinel-1 InSAR data for monitoring and detection of the impact of drought on grasslands in Eastern Cape Province. Analyzed InSAR data included 12 pairs in Interferometric Wide swath mode covering the study area with communal and commercial grasslands during two seasons; drought and non-drought seasons. Results revealed that the non-drought season showed higher variability in the coherence between ROIs than the drought season and higher variability in the backscattering coefficient. InSAR-based approaches have shown potential for monitoring of grasslands under drought and non-drought conditions, and the regularity of Sentinel-1 data is well-suited for InSAR applications. The potential to separate grasslands appears to be limited with longer temporal baseline. This potential will be improved with the 6 days intervals that will become available with Sentinel-1B covering the study area.

Chapter 7

Conclusion and Outlook

This chapter summarizes the main findings reported in this thesis and highlights the implications of using spaceborne SAR data for mapping and monitoring of vegetation in the arid and semi-arid environments in Africa, particularly the two investigated vegetation types; mangroves and grasslands. The chapter concludes with the conclusion and insights into the future perspective of this work.

7.1. Main Findings

Understanding the existing distribution of vegetation in the drylands of Africa, and changes in vegetation properties in response to climate change and land use change is essential for developing strategies for conservation and sustainable management of vegetation in this environment (Siqueira and Durigan, 2007). Remote sensing is considered a viable method for gathering information in a spatially and temporally continuous manner. It offers an efficient and reliable means of collecting spatial information required for assessing vegetation dynamics (Franklin, 2001). Although there are many advantages of using optical remote sensing data for vegetation mapping and monitoring, a major limitation is the availability of cloud-free scenes (Mitchard *et al*., 2011). Several studies have demonstrated the potential of SAR data for vegetation mapping and monitoring indicating that SAR-based methods can potentially outperform the optical remote sensing data (Almeida-Filho *et al*., 2009).

To explore the potential of SAR data for mapping and monitoring of vegetation in the arid and semi-arid environments in Africa, we selected two main case studies. They represent the two main threats affecting the distribution of vegetation in this environment, particularly; climate change, and human disturbance. The first case study is located on the Red Sea coastline in Egypt and focused on mangroves mapping, and the second case study is located in Eastern Cape Province and focused on grasslands monitoring. The findings presented in this thesis, including the three studies in chapters 4, 5 and 6 can be summarized in their contribution to scientific knowledge and the overall objectives of this study as follows:

7.1.1. *Objective I*: Exploring the potential of ALOS PALSAR data for mapping of mangroves extents on the Red Sea coastline

Mangroves are among the most productive and biologically important ecosystems in the world. They are highly productive ecosystems with a rich diversity of flora and fauna (Twilley and Rivera-Monroy, 2005). They support the conservation of biological diversity (Barbier and Sathiratai, 2004). They are considered of great ecological importance (Gedan *et al*., 2011), and great value to the local communities (FAO, 2007). Mangroves experience high yearly loss rates of 1-2% (Beaumont *et al*., 2011). High population pressure in coastal areas has led to the conversion of many mangrove areas to other uses (FAO, 2007). Reasons for this loss are for example over-cutting, over-grazing, and habitat destruction. This places other environmental services provided by mangroves, such as fish nursery areas, coastal protection, and bird roosting areas, at considerable risk.

The study focused on mapping of mangroves extents on the Red Sea coastline in Egypt, through the integration of both L-band SAR data of ALOS/PALSAR and high resolution optical data of RapidEye. We found that the integrated SAR and optical data achieved the highest accuracy of 92.15% in classifying the five land cover types in the mangroves ecosystem. The integration of SAR and optical data has been shown to be a good strategy for overcoming the limitations of the optical data, including the availability of cloud-free scenes, and also coping with the limitations of SAR data for single-date information.

We applied an object-based approach for mapping of mangroves extents in the current study. This approach allowed to clearly discriminate the different land cover classes within the mangroves ecosystem. Additionally, the study focused on assessing the contribution of various features derived from both SAR and optical datasets including vegetation indices (VIs), and texture features (GLCM), as well as the PolSAR parameters derived from the ALOS/PALSAR data, to the overall classification accuracy, using different machine learning algorithms, and comparing their performance.

Random Forest classifier achieved the highest accuracy followed by CART, and the lowest accuracy achieved by SVM. The addition of different features derived from both optical and SAR data was effective in improving the overall accuracy; VIs improved the classification accuracy of optical data, texture features improved the classification accuracy of SAR data and the accuracy of the integrated SAR and optical data. Texture features were much less effective when included with optical data. PolSAR parameters improved the classification accuracy of both SAR data and the integrated SAR and optical data. The addition of different features improved the overall accuracy into a certain margin, and addition of more features after this margin reduced the overall accuracy.

The only uncertainty introduced in the accuracy assessment in the current study was attributed to the time gap between the acquisition times of PALSAR data and the optical data. However, we noticed that there was no major disturbance affecting the study areas within this time gap. This difference assumed to be insignificant for observation and mapping of woody vegetation in the arid and semi-arid environments (Santini *et al*., 2013; Kamal *et al*., 2015). Using SAR data only can still provide important landscape information. This result confirms SAR role in forest and vegetation mapping and suggests that in the areas affected by optical data loss because of the atmospheric conditions, SAR data can be integrated with the available optical data.

Using L-band SAR data was beneficial for mapping of mangroves because of the high penetration of L-band into the canopy, HH polarization has been found to be sensitive for detecting water beneath canopy (Hess *et al*., 1995), whereas HV polarization has been known for its sensitivity to volume scattering and biomass (Bourgeau-Chavez *et al*., 2009). Compared to single-polarized SAR data, the dual-polarimetric SAR data provided much more information about the backscattering mechanism of the mangroves ecosystem. Therefore, dual-polarimetric SAR data enables a more detailed mapping of mangroves. The study showed that using L-band SAR data provided by ALOS PALSAR combined with the high resolution optical data of RapidEye is very useful in mapping mangroves extents growing in fractions and small patches on the Red Sea coastline.

7.1.2. *Objective II*: Assessing the impact of drought on grasslands in Eastern Cape Province using multi-temporal Sentinel-1 data

Grasslands are a major component of the natural vegetation in South Africa, it covers almost one-third of the country's land surface, supporting human, fauna and flora populations by providing numerous goods and services (White *et al*., 2000). Drought has been one of the major factors influencing vegetation dynamics in grasslands (Cook *et al*., 2007) with substantial social and economic consequences. There is a critical need to understand how drought affects grasslands, in part because drought severity and drought-associated grasslands disturbances are expected to increase with the climatic change that might lead to a potential degradation. Better management of grasslands is of great importance for profitability and sustainability.

The study focused on assessing the impact of drought on communal and commercial grasslands in Eastern Cape using multi-temporal SAR data of Sentinel-1. Several studies used remote sensing data for vegetation monitoring, but SAR applications for grasslands monitoring have been much less relative to optical data. The reasons for this include limited availability of SAR data, and complex data structures relative to optical data. This condition changed after the launch of Sentinel-1 SAR data (Torres *et al*., 2012). The availability of multi-temporal SAR data of Sentinel-1 with high temporal and spatial resolution allows for the analysis of seasonal variation, and retrieval of the biophysical parameters of grasslands.

Multi-temporal NDVI data extracted from Landsat-8 were used to contribute to our understanding of the ability of SAR data for monitoring of grasslands and detection of the impact of drought. Results showed that the signals of grasslands in VV backscattering were higher than in VH backscattering. Results also revealed a positive correlation between SAR backscattering and NDVI in both communal and commercial grasslands, with higher correlation of VH backscattering with NDVI in communal grasslands. A linear mixed-effects regression analysis was performed for detecting the impact of drought stress on communal and commercial grasslands in the study area. Results showed that vegetation dynamics in grasslands in the study area are highly responsive to climatic fluctuations. A significant correlation between backscattering coefficients of Sentinel-1 SAR data (VH and VV) and NDVI derived from Landsat-8 was observed for both communal and commercial grasslands (R^2 = 0.89).

Regression analysis revealed that communal grasslands are more affected by the impact of drought than commercial grasslands. Communal grasslands are often cited as more vulnerable to the impact of drought (Pelser *et al*., 2005), due to unsustainable use of resources, while in commercial grasslands, management activities including; organizing the livestock grazing, firing, resting the fields, and grasslands mowing, were able to improve the growing conditions of commercial grasslands, reduced the impact of drought stress, and subsequently increased the grasslands resilience and productivity. The study demonstrated the feasibility of using multi-temporal SAR data of Sentinel-1 for grasslands monitoring and detection of the impact of drought on communal and commercial grasslands. Limitations of the study include the short time series of SAR data, explained by the lack of Sentinel-1 data before 2015.

7.1.3. *Objective III*: Evaluating the potential of InSAR coherence of Sentinel-1 for grasslands monitoring in Eastern Cape Province

This study focused on assessing the potential of InSAR coherence for grasslands monitoring in Eastern Cape. In contrast to SAR backscattering analysis, InSAR exploits the phase component of the microwave signal. It uses the phase difference between two SAR images covering the same area but acquired at different times to detect surface changes. InSAR has been shown to be a powerful technique for vegetation monitoring and potentially more sensitive to changes in the land surface than backscattering variations alone.

We selected 12 regions of interest (ROIs) in two grasslands study locations with communal and commercial grasslands during two growing seasons, drought season (2015/2016), and non-drought season (2016/2017). These ROIs represent different grasslands fields within the communal and commercial grasslands in Eastern Cape Province that were likely to exhibit different seasonal variations in the SAR backscattering and InSAR coherence. Multi-temporal analysis of InSAR coherence showed a large variability during the two growing seasons of the study.

Results revealed the variations in the magnitude of coherence between communal and commercial grasslands during the two studied growing seasons. Non-drought season revealed higher variability in the coherence between ROIs than the drought season. In addition, the magnitude of the coherence in communal grasslands was higher than in commercial grasslands. The variability of the coherence in communal grasslands was higher than in the commercial grasslands during the drought season. This situation changed during the non-drought season, to be less than the variability in commercial grasslands.

The coherence generally revealed high variability between communal and commercial grasslands. Commercial grasslands revealed the highest variability in the coherence (between 0.29 and 0.83) and at the same time the highest coherence values (0.83), followed by communal grasslands (between 0.27 and 0.71), with the highest coherence values (0.71) during the non-drought season. Results revealed the variations in the total precipitation between the two study locations. During the drought season, both communal and commercial grasslands received less precipitation compared to the non-drought season, which explains why the variability in the coherence of the non-drought season was higher in comparison to the variability in the coherence of the drought season. The study demonstrated that InSAR coherence has shown potential for monitoring and detection of the impact of drought on grasslands and the regularity of Sentinel-1 data is well-suited for InSAR applications.

7.3. CONCLUSION

Drylands are under constant threat from multiple stresses and challenges, which occur as a result of a complex interaction of natural processes (such as climate variability, high temperatures, and high potential evapotranspiration), and human-induced processes caused by unsustainable and inadequate land use practices (Reynolds *et al*., 2005). More than half of the African continent can be classified as a dryland system that is characterized by low rainfall and high evapotranspiration (Templeton, 2002). Vegetation degradation is common in the drylands of Africa and this directly leads to soil degradation and desertification (Middleton and D. Thomas, 1997). Desertification threatens the sustainability of the land, and is believed to be one of the most serious global environmental problems. The UNCCD definition of desertification emphasizes two main causative factors, notably climatic variations and human activities; particularly removal of natural vegetation cover (UNCCD, 2005).

Understanding the existing distribution of vegetation in the drylands of Africa, and changes in vegetation properties in response to climate change and land use change is essential for the conservation and sustainable management of vegetation in this environment. This thesis focused on mapping and monitoring of vegetation in the arid and semi-arid environments in Africa. Assessment of the state of vegetation and their dynamics relies on the use of optical remote sensing data. Although there are many advantages of using optical remote sensing data, a major limitation is the availability of cloud-free scenes, which stimulates studies of other remote sensing data sources such as SAR data. SAR data have been used to complement the cloud problems of optical sensor images because SAR data are not influenced by weather conditions.

This thesis highlights the potential and limitations of Spaceborne SAR remote sensing data for mapping and monitoring of vegetation dynamics in the arid and semi-arid environments. SAR technology is a potentially efficient approach for assessing, detecting, and analyzing vegetation dynamics, particularly in remote areas of the arid and semi-arid environments, which characterized by limited accessibility, large spatial extension, and inefficiency of traditional means of ground survey.

Although the working title gives priority to the use of Spaceborne SAR data for mapping and monitoring of vegetation, the emphasis is also put on the advantages of the synergetic application of SAR sensors and the combination with optical data. In the first study in this thesis, ALOS PALSAR data was integrated with high resolution optical data of RapidEye for mapping of mangroves extent on the Red Sea coastline. In the second study, Sentinel-1 SAR and Landsat-8 data were used for assessing and detecting the impact of drought on grasslands in Eastern Cape Province.

This research allows to highlight the following points related to the potential of SAR data for mapping and monitoring of vegetation in the arid and semi-arid environments, based on the two main case studies:

(a) Mapping of Mangroves Extents

- Using SAR data of ALOS/PALSAR integrated with optical data of RapidEye was very useful in the mapping of mangroves extents growing on the Red Sea coastline, showing the effectiveness of integrating different data types for mangroves mapping.

- Applying the Object-based Image Analysis (OBIA) approach for mangroves mapping allowed to clearly discriminating the different land cover classes within the mangroves ecosystem.
- Random forest classifier achieved the highest performance followed by CART, and the lowest accuracy achieved by SVM.
- Vegetation indices improved the overall accuracy of the optical data classification, while texture features and PolSAR parameters improved the overall accuracy of SAR data, and the integrated SAR and optical data classifications.
- The produced maps provided accurate information on the spatial distribution of mangroves in the study area, which is required for the conservation and sustainable management of mangroves in this area.

(b) Monitoring of Grasslands

- The availability of multi-temporal SAR data of Sentinel-1 with high temporal and spatial resolution allows for the analysis of seasonal variation in grasslands and retrieval of the biophysical parameters.
- The obtained spatial knowledge allows an improved understanding of the impact of drought on grasslands.
- The study revealed the seasonal dynamics of grasslands in the study area and provided insights into explaining the response of communal and commercial grasslands to the changes in precipitation and the impact of drought.
- The study revealed that communal grasslands are more affected by drought than commercial grasslands. Management activities improved the growing conditions of commercial grasslands.
- The study demonstrated the feasibility of using multi-temporal SAR data of Sentinel-1 for grasslands monitoring and detection of the impact of drought on communal and commercial grasslands.

- InSAR coherence has shown potential for grasslands monitoring under drought and non-drought conditions, and the regularity of Sentinel-1 data is well-suited for InSAR applications.
- The generated spatial data can contribute to the policy and decision-making process on the conservation and sustainable management of vegetation in the drylands of Africa.
- Data availability and quality are crucial factors for successful applications of Spatio-temporal analyses for mapping and monitoring of vegetation in the arid and semi-arid environments.

7.4. Outlook

The thesis focused on the potential of spaceborne SAR data for mapping and monitoring of vegetation dynamics in the arid and semi-arid environments in Africa. In this section, we would like to point out new challenges and perspectives for dedicated research in the field of SAR remote sensing for environmental monitoring.

In chapter 4, we evaluated the potential of ALOS/PALSAR for mapping of mangroves extents on the Red Sea coastline using object-based image analysis method, through applying different machine learning algorithms, and evaluating various features and parameters for the discrimination of mangroves ecosystem. This method used only one date of ALOS/ PASAR data. Using multi-temporal SAR data for mapping of mangroves will provide more insights on the temporal change in the mangroves, as well as improve the understanding of the driving forces affecting the distribution of mangroves in the study area.

Recommendations are made to use ALOS-2 PALSAR for monitoring of mangroves ecosystems with a higher spatial and temporal resolution of SAR data, as well as using other parameters such decomposition of polarimetric SAR data for better discrimination and identification of mangroves ecosystems based on the different scattering mechanisms. Recommendations also are made for further analysis on the remote sensing of mangroves including applying InSAR data analysis for assessing vegetation height and biomass. Additionally, this study focused on a small area on the Red Sea coastline. Suggestions are made to extend the coverage of the study area to include large study areas with different mangroves extents.

In chapters 5 and 6, we used SAR backscattering and InSAR coherence for monitoring of grasslands and assessing the impact drought on communal and commercial grasslands in Eastern Cape Province. This method used a short time series of Sentinel-1 SAR data, explained by the lack of S1 data before 2015. Recommendations are made to combine multi-source and multi-frequency SAR data with longer time series to avoid the short time series of Sentinel-1 data, for better prediction of the impact of drought on grasslands. In addition, Recommendations are made to integrate SAR data with high resolution and high temporal optical data such as Sentinel-2 for improved monitoring of the impact of drought on grasslands.

References

Abatzoglou, J.T., and Kolden, C.A. 2011. Climate change in western U.S. deserts: potential for increased wildfire and invasive annual grasses. *Rangeland Eco. Manag.* 64, 471-478.

Abu Al-Izz M.S. 1971. Landforms of Egypt. – Cairo: The American University in Cairo Press.

Ahmed, R., Siqueira, P., Hensley, S., Chapman, B., and Bergen, K. 2011. A survey of temporal decorrelation from spaceborne L-band repeat-pass InSAR, *Remote Sens. Environ.*, vol. 115, no. 11, pp. 2887–2896.

Ali, I., Schuster, C., Zebisch, M., Forster, M., Kleinschmit, B., and Notarnicola, C. 2013. First results of monitoring nature conservation sites in alpine region by using very high resolution (VHR) X-band SAR data. *IEEE J. of Selected Topics in Applied Earth Observations and Remote Sens.* 6, 2265 - 2274.

Ali, I., Barrett, B., Cawkwell, F., Green, S., Dwyer, E., and Neumann, M. 2017. Application of Repeat-Pass TerraSAR-X Staring Spotlight Interferometric Coherence to Monitor Pasture Biophysical Parameters: Limitations and Sensitivity Analysis. *IEEE J. of Selected Topics in Applied Earth Observations and Remote Sens.* 1-7.

Almeida-Filho, R., Shimabukuro, Y.E., Rosenqvist, A., and Sanchez, G.A. 2009. Using dual-polarized ALOS PALSAR data for detecting new fronts of deforestation in the Brazilian Amazonia. *Int. J. Remote Sens*. 30, 3735–3743.

Amarsaikhana, D., Blotevogelb, H.H., van Genderenc, J.L., Ganzoriga, M., Gantuyaa, R., and Nerguia, B. 2010. Fusing high resolution SAR and optical imagery for improved urban land cover study and classification. *Int. J. Image Data Fusion.* 1, 83–97.

Anguita, D., Ghio, A., Greco, N., Oneto, L., and Ridella, S. 2010. Model Selection for Support Vector Machines: Advantages and Disadvantages of the Machine Learning Theory. In Proceedings of the International Joint Conference on Neural Networks, Barcelona, Spain, 18–23 July; pp. 1–8.

Archibald, S., and Scholes, R.J. 2007. Leaf green-up in a semi-arid African savanna—separating tree and grass responses to environmental cues. *J. Veg. Sci.* 2007, 181, 583–594.

Askne, J., Santoro, M., Smith, G., Fransson, J.E.S. 2003. Multi-temporal repeat-pass SAR interferometry of boreal forests," *IEEE Trans. Geosci. Remote Sens.*, vol. 41, no. 7, pp. 1540–1550.

Askne, J.I.H., Fransson, J.E.S., Santoro, M., Soja, M.J., and Ulander, L.M.H. 2013. Model-based biomass estimation of a hemi-boreal forest from multi-temporal TanDEM-X acquisitions. *Remote Sens*. 5, 5574–5597.

Aslan, A., Abdullah, F.R., Matthew, W.W., and Scott, M.R. 2016. Mapping spatial distribution and biomass of coastal wetland vegetation in Indonesian Papua by combining active and passive remotely sensed data. *Remote Sens. Environ.* 183, 65–81.

Baatz, M., and Schäpe, A. 2000. Multiresolution segmentation - an optimization approach for high quality multi-scale image segmentation. In *Angewandte Geographische Informationsverarbeitung XII*; Strobl, J., Blaschke, T., Griesebner, G., Eds.; Wichmann: Heidelberg, Germany, pp. 12–23.

Barbier, E.B., and Sathiratai, S. 2004. Shrimp Farming and Mangrove Loss in Thailand; Edward Elgar: Cheltenham, UK.

Barrett, C.B. and Upton, J.B. 2013 Food Security and Sociopolitical Stability in Sub-Saharan Africa. Food Security and Sociopolitical Stability. New York, NY: Oxford University Press.

Baudoin, M.A., Vogel, C., Nortje, K., and Naik, M. 2017. Living with drought in South Africa: lessons learnt from the recent El Niño drought period. *Int. J. of Disaster Risk Reduction*, 23, 128–137

Beaumont, L.J., Pitman, A., Perkins, S., Zimmermann, N.E., Yoccoz, N.G., and Thuiller, W. 2011. Impacts of climate change on the world's most exceptional ecoregions. *Proc. Natl. Acad. Sci. USA*, 108, 2306–2311.

Benz, U.C., Hofmann, P., Willhauck, G., Lingenfelder, I., and Heynen, M. 2004. Multi-resolution, object-oriented fuzzy analysis of remote sensing data for GIS-ready information. *ISPRS J. Photogramm. Remote Sens*. 58, 239–258.

Berger, M., Moreno, J., Johannessen, J.A., Levelt, P.F., and Hanssen, R.F. 2012. ESA's sentinel missions in support of earth system science. *Remote Sens. of Envir.* 120, 84–90.

Blaschke, T. 2010. Object based image analysis for remote sensing. *ISPRS J. Photogramm. Remote Sens*. 65, 2–16.

Bourgeau-Chavez, L.L., Riordan, K., Powell, R.B., Miller, N., and Nowels, M. 2009. Improving wetland characterization with multi-sensor, multi-temporal SAR and optical/infrared data fusion. In *Advances in Geoscience and Remote Sensing*; Jedlovec, G., Ed.; InTech: Rijeka, Crotia.

Burai, P., Deak, B., Valko, O., and Tomor, T. 2014. Classification of herbaceous vegetation using airborne hyperspectral imagery*. Remote Sens.* 7, 2046–2066.

Campbell, B.A. 2002. Radar Remote Sensing of Planetary Surfaces, Cambridge Univ. Press, Cambridge, U. K.

Carlson, T.N., Ripley, D.A. 1997. On the relation between NDVI, fractional vegetation cover, and Leaf Area Index. *Remote Sens. Environ*. *62*, 241–252.

Carreiras, J.M.B., Melo, J.B., Vasconcelos, M.J. 2013. Estimating the above-ground biomass in Miombo Savanna Woodlands (Mozambique, East Africa) using L-band synthetic aperture radar data. *Remote Sens*. 5, 1524–1548.

Clark, V.R., Barker, N.P., and Mucina, L. 2009. The Sneeuberg: a new centre of floristic endemism on the Great Escarpment, South Africa. *South African Journal of Botany*, 75, 196–238.

Cloude, S.R., and Pottier, E. 1997. An entropy based classification scheme for land applications of polarimetric SAR. *IEEE Trans. Geosci. Remote Sens.* 35, 68–78

Cobon, D.H., Baethgen, W.E., Landman, W., Williams, A., van Garderen, E.A., Johnston, P., Malherbe, J., Maluleke, P., Ben Kgakatsi, I., and Davis, P. 2017. Agroclimatology in Grasslands. In: J.L. Hatfield, M.V.K. Sivakumar and J.H. Prueger (Editors), Agroclimatology: Linking Agriculture to Climate. Agronomy Monographs. American Society of Agronomy, Crop Science Society of America, and Soil Science Society of America, Inc., Madison, WI.

Congalton, R.G., and Green, K. 1999. *Assessing the Accuracy of Remotely Sensed Data: Principles and Practices*; Lewis Publishers: Boca Raton, FL, USA.

Cook, E.R., Seager, R., Cane, M.A., and Stahle, D.V. 2007. North American drought: reconstructions, causes, and consequences. *Earth-Science Reviews*, 81(1), 93-134.

Curlander, J.C., and McDonough, R.N. 1991. Synthetic Aperture Radar: Systems and Signal Processing. Wiley.

Davies, J., Poulsen, L., Schulte-Herbrüggen, B., Mackinnon, K., Crawhall, N., Henwood, W.D., Dudley, N., Smith, J. and Gudka, M. 2012. Conserving Dryland Biodiversity. IUCN – Drylands Initiative, Nairobi.

Definiens Ecognition. 2009. Available online: http://www.ecognition.com (accessed on 10 June 2015).

Derner, J.D., and Schuman, G.E. 2007. Carbon sequestration and rangelands: A synthesis of land management effects. *J. Soil Water Conserv*. 62:77–85.

Dorigo, W., Lucieer, A., Podobnikar, T., and Carni, A. 2012. Mapping invasive Fallopia japonica by combined spectral, spatial, and temporal analysis of digital orthophotos*. Int. J. Appl. Earth Obs. Geoinf*. 19, 185–195.

Ehlers, M., Klonus, S., Johan, Ã., Strand, P.R., and Rosso, P. 2010. Multi-sensor image fusion for pan-sharpening in remote sensing. *Int. J. Image Data Fusion*, 1, 25–45.

EL-Gazzar, A. 1995. Egypt: Country Study on Biological Diversity. Publication of National Biodiversity Unit, No. 5, 217 pp.

Ellison, J.C. 2015. Vulnerability assessment of mangroves to climate change and sea-level rise impacts. *Wetl. Ecol. Manag.* 23, 115.

Engler, R., Guisan, A., and Rechsteiner, L. 2004. An improved approach for predicting the distribution of rare and endangered species from occurrence and pseudo-absence data. *J. of App. Ecol.* 41: 263–274.

Evans, S.E., and Burke, I.C. 2013. Carbon and nitrogen decoupling under an 11-year drought in the short grass steppe. *Ecosystems*, 16, 20-33.

FAO. 2001. Global Forest Resources Assessment 2000. FAO Forest Paper, No. 140. FAO, Rome.

FAO. 2006. Livestock's long shadows: environmental issues and options. Food and Agriculture Organization of the United Nations, Rome.

FAO. 2007. *The World's Mangroves 1980–2005*; FAO Forestry 153; FAO: Rome, Italy.

Feller, I.C., Lovelock, C.E., Berger, U., McKee, K.L., Joye, S.B., and Ball, M.C. 2010. Biocomplexity in mangrove ecosystems. *Annu. Rev. Mar. Sci.* 2, 395–417.

Foody, G.M. 2002. Status of Land Cover Classification Accuracy Assessment. *Remote Sens. Environ.* 80, 185–201.

Foody, G.M., and Mathur, A. 2004. Toward intelligent training of supervised image classifications: Directing training data acquisition for SVM classification. *Remote Sens. Environ*. 93, 107.

Franklin, S.E., 2001. Remote sensing for sustainable forest management. CRC Press, Boca Raton, FL.

Franzluebbers, A.J. 2010. Achieving soil organic carbon sequestration with conservation agricultural systems in the southeastern United States. *Soil Sci. Soc. Am. J.* 74:347–357.

Freeman, A., and Durden S.L. 1998. A three-component scattering model for polarimetric SAR data. *IEEE Trans. Geosci. Remote Sens*., 36 (3) (1998), pp. 963-973.

Friedl, M.A., and Brodley, C.E. 1997. Decision tree classification of land cover from remotely sensed data. *Remote Sens. Environ.* 61, 399–409.

Funk, C., Peterson, P., Landsfeld, M., Pedreros, D., Verdin, J., Shukla, S., Husak, G., Rowland, J., Harrison, L., Hoell, A., and Michaelsen, J. 2015. The climate hazards infrared precipitation with stations - A new environmental record for monitoring extremes. *Scientific Data*, 2, 150066.

Galal, N. 1999. Studies on the Coastal Ecology and Management of the Nabq Protected Area, South Sinai, Egypt. Ph.D. Thesis, University of York, York, UK.

Gedan, K.B., Kirwan, M.L., Wolanski, E., Barbier, E.B., and Silliman, B.R. 2011. The present and future role of coastal wetland vegetation in protecting shorelines: Answering recent challenges to the paradigm. *Clim. Chang*. 106, 7–29.

Ghosh, A., Fassnacht, F.E., Joshi, P.K., and Koch, B. 2014. A framework for mapping tree species combining hyperspectral and LiDAR data: Role of selected classifiers and sensor across three spatial scales. *Int. J. Appl. Erath Obs. Geoinf.* 26, 49–63.

Gilman, E., Ellison, J., Duke, N.C., and Field, C. 2008. Threats to mangroves from climate change and adaptation options: A review. *Aquat. Bot.* 89, 237–250.

Giri, C., Pengra, B., Zhu, Z., Singh, A., and Tieszen, L.L. 2007. Monitoring Mangrove forest dynamics of the Sundarbans in Bangladesh and India using multi-temporal satellite data from 1973 to 2000. *Estuar. Coast. Shelf Sci*. 73, 91–100.

Gislason, P.O., Benediktsson, J.A., and Sveinsson, J.R. 2006. Random forests for land cover classification. *Pattern Recogn. Lett*. 27, 294–300.

Gitelson, A., Kaufman, Y., and Merzlyak, M. 1996. Use of a green channel in remote sensing of global vegetation from EOS-MODIS. *Remote Sens. Environ.* 58, 289–298.

Google Earth Engine [GEE]. 2015. A planetary-scale geospatial analysis platform. https://eathengine.google.com. Accessed May 6th, 2017.

Graw, V., Ghazaryan, G., Dall, K., Gómez, A.D., Abdel-Hamid, A., Jordaan, A., Piroska, R., Post, J.; Szarzynski, J., Walz, Y., and Dubovyk, O. 2017. Drought Dynamics and Vegetation Productivity in Different Land Management Systems of Eastern Cape, South Africa - A Remote Sensing Perspective. *Sustainability*, 9, 1728.

Green, E.P., Clark, C.D., Mumby, P.J., Edwards, A.J., and Ellis, A. 1998. Remote sensing techniques for mangrove mapping. *Int. J. Remote Sens.* 19, 935–956.

Green, E.P., Mumby, P.J., Edwards, A.J., and Clark, C.D. 1996. A review of remote sensing for the assessment and management of tropical coastal resources. *Coast. Manag.* 24, 1–40.

Haack, B., and Bechdol, M. 2000. Integrating multisensor data and RADAR texture measures for land cover mapping. *Comput. Geosci.* 26, 411–421.

Haboudane, D., Miller, J.R., Pattey, E., Zarco-Tejada, P.J., and Strachan, I.B. 2004. Hyperspectral vegetation indices and novel algorithms for predicting green LAI of crop canopies: Modelling and validation in the context of precision agriculture. *Remote Sens. Environ*. 90, 337–352.

Häme, T., Rauste, Y., Sirro, L., and Stach, N. 2009. Forest cover mapping in French Guiana since 1992 using satellite radar imagery. In Proceedings of the International Symposium on Remote Sensing of Environment (ISRSE 33), Stresa, Italy, 4–8 May.

Head, S.M. 1987. Introduction. In Key Environments: the Red Sea (A. J. Edwards and S.M. Head, eds.): 1-21. Oxford: Pergamon.

Henderson, F.M., and *Lewis*, A.J. 2008. *Radar* Detection of Wetland Ecosystems A Review. *Int. J. of Remote Sens.* Vol. 29, No. 20.

Haralick, R.M., Shanmugam, K., and Dinstein, I. 1973. Textural features for image classification. *IEEE Trans. Syst. Man Cybern.* 6, 269–285.

Hay, G.J., and Castilla, G. 2008. Geographic Object-Based Image Analysis (GEOBIA): A new name for a new discipline. In *Object Based Image Analysis*; Blaschke, T., Lang, S., Hay, G., Eds.; Springer: Heidelberg/Berlin, Germany; New York, NY, USA, pp. 93–112.

Held, A., Ticehurst, C., Lymburner, L., and Williams, N. 2003. High resolution mapping of tropical mangrove ecosystems using hyperspectral and radar remote sensing. *Int. J. Remote Sens.* 24, 2739–2759.

Hess, L.L., Melack, J.M., Filoso, S., and Wang, Y. 1995. Delineation of inundated area and vegetation along the Amazon floodplain with the SIR-C synthetic aperture radar. *IEEE Trans. Geosci. Remote Sens*. 33, 896–904.

Hoare, D.B., and Bredenkamp, G.J. 2001. Syntaxonomy and environmental gradients of the grasslands of the Stormberg/Drakensberg Mountain Region of the Eastern Cape, South Africa. *South African Journal of Botany*, 67, 595–608.

Hoare, D.B., Mucina, L., Rutherford, M.C., Vlok, J.H., Euston-Brown, D.I., Palmer, A.R., Powrie, L.W., Lecmere-Oertel, R., Procheş, Ş.M., and Dold, A.P. 2006. Albany thicket biome, the vegetation of South Africa, Lesotho and Swaziland. South African National Biodiversity Institute. Pretoria, South Africa, pp. 541-567.

Hoekman, D.H., Vissers, M.A.M., and Wielaard, N. 2010. PALSAR wide-area mapping of Borneo: Methodology and map validation. *IEEE J. Sel. Top. Appl. Earth Obs. Remote Sens*. 3, 605–617.

Hogarth, P.J. 1999. *The Biology of Mangroves*, Oxford University Press: Oxford, UK.

Huete, A., Didan, K., Miura, T., Rodriguez, E.P., Gao, X., and Ferreira, L.G. 2002. Overview of the radiometric and biophysical performance of the MODIS vegetation indices. *Remote Sens. Environ*. 83, 195–213.

Huete, A.R. 1988. A soil-adjusted vegetation index (SAVI). *Remote Sens. Environ.* 25, 295–309.

Hurni, K., Hett, C., Epprecht, M., Messerli, P., and Heinimann, A. 2013. A texture-based land cover classification for the delineation of a shifting cultivation landscape in the Lao PDR using landscape metrics. *Remote Sens.* 5, 3377–3396.

Ismail, R., Mutanga, O., and Kumar, L. 2010. Modelling the potential distribution of pine forests susceptible to Sirex Noctilo infestations in Mpumalanga, South Africa. *Trans. GIS.* 14, 709–726.

Jensen, J.R., Lin, H., Yang, X., Ramsey, E., Davis, B.A., and Thoemke, C.W. 1991. The measurement of mangrove characteristics in southwest Florida using SPOT multispectral data. *Geochem. Int.* 2, 13–21.

Jiang, Z., Huete, A.R., Didan, K., and Miura, T. 2008. Development of a two-band enhanced vegetation index without a blue band. *Remote Sens. Environ.* 112, 3833–3845.

Jordaan, A.J. 2017. Vulnerability, Adaption, to and Coping with Drought. The Case of Commercial and Subsistence Rain Fed Farming in the Eastern Cape. Report to the Water Research Commission and Department of Agriculture, Forestry and Fisheries. 1. Bloemfontein.

Just, D., and Bamler, R. 1994. Phase statistics of interferograms with applications to synthetic aperture radar. *Appl. Opt*. 33, 4361–4368.

Kamal, M., Phinn, S., and Johansen, K. 2015. Object-Based Approach for Multi-Scale Mangrove Composition Mapping Using Multi-Resolution Image Datasets. *Remote Sens*. 7, 4753–4783.

Kane, R.P. 2009. Periodicities, ENSO effects and trends of some South African rainfall series: An update. *South African J. of Sci.* 105, 5-6.

Kauth, R.J., and Thomas, G.S. 1976. The tasseled cap-A graphic description of the spectral-temporal development of agricultural crops as seen by Landsat. In Proceedings of the Symposium on Machine Processing of Remotely Sensed Data, West Lafayette, IN, USA, 9 June–1 July; pp. 4B-41–4B-50.

Ke, Y., Quackenbush, L.J., and Im, J. 2010. Synergistic use of Quick Bird multispectral imagery and LIDAR data for object-based forest species classification. *Remote Sens. Environ.* 114, 1141–1154.

Keyantash, J., and Dracup, J.A. 2002. The quantification of drought: An evaluation of drought indices. *Bull. Am. Meteorol. Soc.* 83, 1167–1180.

Knapp, A.K., and Smith, M.D. 2001. Variation among biomes in temporal dynamics of aboveground primary production. *Science*, 291, 481-484.

Kogan, F.N. 1997. Global drought watch from space. *Bull. Am. Meteorol. Soc.* 78, 621–636.

Kornelsen, K., and Coulibaly, P. 2013. Advances in soil moisture retrieval from synthetic aperture radar and hydrological applications, *J. Hydrol*. 476(1), 460-489.

Lacerda, L.D. (Ed.) 2001. American mangroves. In *Mangrove Ecosystems*; Springer-Verlag: Berlin/Heidelberg, Germany, pp. 1–62.

Lal, R. 2004. Carbon sequestration in dryland ecosystems. Environmental Management 33:528-544.

Laliberte, A.S., Fredrickson, E.L., and Rango, A. 2007. Combining decision trees with hierarchical object-oriented image analysis for mapping arid rangelands. *Photogramm. Eng. Remote Sens*. 73, 197–207.

Lang, M., and McCarty, G. 2008. Wetland Mapping: History and Trends. In *Wetlands: Ecology, Conservation and Management*; Russo, R.E., Ed.; Nova Publishers: New York, NY, USA, pp. 74–112.

Lang, S. 2008. Object-based image analysis for remote sensing applications: Modeling reality—dealing with complexity. In *Object-Based Image Analysis*; Blaschke, T., Lang, S., Hay, G.J., Eds.; Springer: Heidelberg/Berlin, Germany; New York, NY, USA, pp. 1–25.

Langley S.K., Cheshire, H.M., and Humes, K.S. 2001. A comparison of single date and multitemporal satellite image classifications in a semi-arid grassland. *J. Arid Environ.* 49:401–11.

Laurin, G.V., Liesenberg, V., Chen, Q., Guerriero, L., Frate, F.D.; Bartolini, A., Coomes, D., Wilebore, B., Lindsell, J., and Valentini, R. 2013. Optical and SAR sensor synergies for forest and land cover mapping in a tropical site in West Africa. *Int. J. Appl. Earth Obs. Geoinf.* 21, 7–16.

Lavalle, M., Simard, M., and Hensley, S. 2012. A temporal decorrelation model for polarimetric radar interferometers. *IEEE Trans. Geosci. Remote Sens*. 2880-2888, 7.

Lawrence, R.L., and Wright, A. 2001. Rule-based classification systems using classification and regression tree (CART) analysis. *Photogramm. Eng. Remote Sens.* 67, 1137–1142.

Le Toan, T., Quegan, S., Davidson, M.W.J., Balzter, H., Paillou, P., Papathanassiou, K., Plummer, S., Rocca, F., Saatchi, S., and Shugart, H. 2011. The BIOMASS mission: Mapping global forest biomass to better understand the terrestrial carbon cycle. *Remote Sens. Envir*. 115, 2850–2860.

Lee, J.S., Grunes, M.R., and de Grandi, G. 1999. Polarimetric SAR speckle filtering and its implication for classification. *IEEE Trans. Geosci. Remote Sens.* 37, 2363–2373.

Lee, J.-S., and Pottier, E. 2009. Polarimetric radar imaging: from basics to applications. CRC press. doi: http://dx.doi.org/10.1201/9781420054989.

Lee, J.-S., Wen, J.-H., Ainsworth, T.L., Chen, K.-S., and Chen, A.J. 2009. Improved sigma filter for speckle filtering of SAR imagery. *IEEE Trans. Geosci. Remote Sens.* 47, 202–213.

Li, S., Xie, Y., Brown, D.G., Bai, Y., Hua, J., and Judd, K. 2013. Spatial variability of the adaptation of grassland vegetation to climatic change in Inner Mongolia of China. *Applied Geography*, 43, 1-12.

Lillesand, T.M., Kieffer, R.W. Kiefer. 1999. Remote Sensing and Image Interpretation. John Wiley & Sons, Inc. New Jersey.

Lillesand, T.M., Kiefer, R.W. and Chipman, J.W. 2008. *Remote Sensing and Image Interpretation,* New York, Wiley International.

Linnell, J. D.C., Kaczensky, P., Wotschikowsky, U., Lescureux, N., and Boitani, L. 2015. Framing the relationship between people and nature in the context of European conservation. *Conservation Biology*, 29, 978–985.

Liu, X., Yin, Z.-Y., Shao, X., and Qin, N. 2006. Temporal trends and variability of daily maximum and minimum, extreme temperature events, and growing season length over the eastern and central Tibetan Plateau during 1961-2003. *Journal of Geophysical Research*, *Atmospheres*, 111, D19.

Liu, Y., Li, M., Mao, L., and Xu, F. 2006. Review of remotely sensed imagery classification patterns based on object oriented image analysis. *Chin. Geogr. Sci.* 16, 282–288.

Long, B.G., and Skewes, T.D. 1996. A technique for mapping mangroves with Landsat TM satellite data and geographic information system. *Estuar. Coast. Shelf Sci.* 43, 373–381.

Longepe, N., Rakwatin, P., Isoguchi, O., Shimada, M., Uryu, Y., and Yulianto, K. 2011. Assessment of ALOS PALSAR 50 m orthorectified FBD data for regional land cover classification by support vector machines. *IEEE Trans. Geosci. Remote Sens*. 49, 2135–2150.

Lu, D., and Batistella, M. 2005. Exploring TM image texture and its relationships with biomass estimation in Rondônia, Brazilian Amazon. *Acta Amaz.* 35, 249–257.

Lucas, R.M., Mitchell, A.L., Rosenqvist, A., Proisy, C., Melius, A., and Ticehurst, C. 2007. The potential of L-band SAR for quantifying mangrove characteristics and change: Case studies from the tropics. *Aquat. Conserv. Mar. Freshw. Ecosyst.* 17, 245–264.

Luo, X., Askne, J., Smith, G., and Dammert, P. 2001. Coherence characteristics of RADAR signals from rough soil. *Prog. Electromag. Res*. 31, 68–88.

Maillard, C. and Soliman, G. 1986 Hydrography of the Red Sea and Exchanges with the Indian Ocean in Summer. *Oceanologica Acta*, 9, 249-269.

Marceau, D. 1999. The scale issue in the social and natural sciences. *Can. J. Remote Sens*. 25, 347–356.

Masek, J.G., Hayes, D.J., Joseph Hughes, M., Healey, S.P., and Turner, D.P. 2015. The role of remote sensing in process-scaling studies of managed forest ecosystems. For Ecol Manage, Carbon, water and nutrient cycling in managed forests, 355, 109–123.

Mattia, F., Le Toan, T., Souyris, J.-C., De Carolis, G., Floury, N., Posa, F., and Pasquariello, G. 1997. The effect of surface roughness on multifrequency polarimetric SAR data, *IEEE T. Geosci. Remote Sens.* 35, 954–966, 1997.

Maurizio, S., Eriksson, L.E.B., and Fransson, J.E.S. 2015. Reviewing ALOS PALSAR backscatter observations for stem volume retrieval in Swedish forest. *Remote Sens*. 7, 4290–4317.

McCoy, R.M. 2005. *Field Methods in Remote Sensing*; Guildford Press: New York, NY, USA.

McKeon, G., Hall, W., Henry, B., Stone, G., and Watson, I. 2004. Pasture degradation and recovery in Australia's rangelands: Learning from history. Queensland Department of Natural Resources, Mines and Energy, Brisbane, Australia.

McLean, R.A., Sanders, W.L., and Stroup, W.W. 1991. A Unified Approach to Mixed Linear Models. The American Statistician. *American Statistical Assoc.* 45, 54-64.

McNairn, H., Shang, J., Champagne, C., and Jiao, X. 2009. TerraSAR-X and RADARSAT-2 for crop classification and acreage estimation. In Proceedings of IEEE International Geoscience and Remote Sensing Symposium IGARSS (pp. II-898–II-901).

McNeill, S., Pairman, D., Belliss, S., Dalley, D., and Dynes, R. 2010. Robust Estimation of Pasture Biomass Using Dual-Polarisation TerrASAR-X Imagery. In Proceedings of IEEE International Geoscience and Remote Sensing Symposium IGARSS (pp. 3094–3097), Honolulu, HI, USA.

Meyer, D. 2014. Support Vector Machines. Available online: http://cran.rproject.org/web/packages /e1071/vignettes/svm-doc.pdf (accessed on 27 February 2018).

MEA, 2005. Ecosystems and Human Well-being: Desertification Synthesis. Millennium Ecosystem Assessment. World Resources Institute, Washington, DC.

Middleton, N. and D. Thomas, 1997: World Atlas of Desertification, Arnold, London.

Mitchard, E.T.A., Saatchi, S.S., Lewis, S.L., Feldpausch, T.R., Woodhouse, I.H., Sonke, B., Rowland, C., and Meir, P. 2011. Measuring biomass changes due to woody encroachment and deforestation/degradation in a forest-savanna boundary region of central Africa using multi-temporal L-band radar backscatter. *Remote Sens. Environ*. 115, 2861–2873.

Morandeira, N., Grings, F., Facchinetti, C., and Kandus, P. 2016. Mapping plant functional types in floodplain wetlands: An analysis of c-band polarimetric SAR data from Radarsat-2. *Remote Sens.* 8, 174.

Morishita, Y., and Hanssen, R. 2015. Temporal decorrelation in L-, C-, and Xband satellite radar interferometry for pasture on drained peat soils," *IEEE Trans. Geosci. Remote Sens.*, vol. 53, no. 2, pp. 1096–1104.

Münch, Z., Okoye, P.I., Gibson, L., Mantel, S., and Palmer, A. 2017. Characterizing Degradation Gradients through Land Cover Change Analysis in Rural Eastern Cape, South Africa. *Geosciences.* 7, 7.

Naidoo, L., Mathieu, R., Main, R., Kleynhans, W., Wessels, K., Asner, G., and Leblon, B. 2015. Savannah woody structure modelling and mapping using multi-frequency (X-, C- and L-band) Synthetic Aperture Radar data. *ISPRS J. Photogramm. Remote Sens.* 105, 234–250.

Neukermans, G., Dahdouh-Guebas, F., Kairo, J.G., and Koedam, N. 2008. Mangrove species and stand mapping in Gazi Bay (Kenya) using Quickbird satellite imagery. *J. Spat. Sci.* 53, 75–86.

Ngaka, M.J. 2012. Drought preparedness, impact and response: A case of the Eastern Cape and Free State provinces of South Africa. *J. of Disaster Risk Studies*, 4, 1.

Nordberg, M.L., Evertson, J. 2003. Vegetation index differencing and linear regression for change detection in a Swedish mountain range using Landsat TM and ETM+ imagery. *Land Degradation & Development* 16:139–149.

Ortega-Huerta, M.A., and Peterson, T.A. 2004. Modelling spatial patterns of biodiversity for conservation prioritization in northeastern Mexico. *Diversity and Distributions,* 10:39-54.

Palmer, A.R., and Ainslie, A.M. 2005. Grasslands of South Africa. In: Food and Agriculture Organization, (Eds.), Grasslands of the World. Rome (Italy) (pp. 77–120), Food and Agriculture Organization [FAO] of the United Nations (UN).

Parton, W., Morgan, J., Smith, D., Del Grosso, S., Prihodko, L., LeCain, D., Kelly, R., and Lutz, S. 2012. Impact of precipitation dynamics on net ecosystem productivity. *Global Change Biology*, 18, 915–927.

Paudel, K.P., and Andersen, P. 2010. Assessing rangeland degradation using multi- temporal satellite images and grazing pressure surface model in Upper Mustang, Trans Himalaya, Nepal. *Remote Sens. of Envir.* 114(8), 1845–1855.

Pelser, A.J., Redelinghuys, N., Viljoen, M.F., and Teweldemehin, M.Y. 2005. Policy Guidelines for the evaluation of social, economic and political impacts of drought and aridity, University of Free State, Bloemfontein, South Africa.

Peters, A.J., Walter-Shea, E.A., Ji, L., Vina, A., Hayes, M., and Svoboda, M. 2002. Drought monitoring with NDVI-based Standardized Vegetation Index. *Photogrammetric Engineering and Remote Sensing*, 68, 71–75.

Pettorelli, N., Laurance, W.F., O'Brien, T.G., Wegmann, M., Nagendra, H., Turner, W. 2014. Satellite remote sensing for applied ecologists: opportunities and challenges. *J. of App. Ecol.* 51, 839–848.

Piñeiro, G., Oesterheld, M., and Paruelo J.M. 2006. Seasonal Variation in Aboveground Production and Radiation-use Efficiency of Temperate rangelands Estimated through Remote Sensing. *Ecosystems*, 9, 357–373.

Piras, M., Mascaro, G., Deidda, R., and Vivoni, E.R. 2016. Impacts of climate change on precipitation and discharge extremes through the use of statistical downscaling approaches in a Mediterranean basin. *Science of the Total Environment*, 543, 952–964.

Pohl, C., and Van Genderen, J.L. 1998. Multisensor image fusion in remote sensing: Concepts, methods and applications. *Int. J. Remote Sens*. 19, 823–854.

Pottier, E., Ferro-Famil, L., Allain, S., Cloude, S., Hajnsek, I., Papathanassiou, K., Moreira, A., Williams, M., Minchella, A., and Lavalle, M. 2009. Overview of the PolSARpro V4.0 software: The open source toolbox for polarimetric and interferometric polarimetric SAR data processing. In Proceedings of the IEEE International Geoscience and Remote Sensing Symposium, Cape Town, South Africa, 12–17 July; pp. IV-936–IV-939.

Prasad, A.M., Iverson, L.R., and Liaw, A. 2006. Newer classification and regression tree techniques: Bagging and random forests for ecological prediction. *Ecosystems.* 9, 181–199.

Qi, J., Chehbouni, A., Huete, A.R., Kerr, Y.H., and Sorooshian, S. 1994. A Modified Soil Adjusted Vegetation Index. *Remote Sens. Environ.* 48, 119–126.

Ramsey, E.W., III, Chappell, D.K., Jacobs, D., Sapkota, S.K., and Baldwin, D.G. 1998. Resource management of forested wetlands: Hurricane impact and recovery mapping by combining Landsat TM and NOAA AVHRR data. *Photogramm. Eng. Remote Sens.* 64, 733–738.

Rasolofoharinoro, M., Blasco, F., Bellan, M., Aizpuru, M., Gauquelin, T., and Denis, J. 1998. A remote sensing based methodology for mangrove studies in Madagascar. *Int. J. Remote Sens.* 19, 1873–1886.

Reynolds, J.F., Stafford-Smith, D.M., Lambin, E.F., Turner II, B.L., Mortimore, M., Batterbury, S.P.J., Downing, T.E., Dowlatabadi, H., Fernandéz, R.J., Herrick, J.E., Huber-Sannwald, E., Jiang, H., Leemans, R., Lynam, T., Maestre, F.T., Ayarza, M., and Walker, B. 2007. Global Desertification: building a science for dryland development. Science 316: 847-851.

Richards, M.A., Scheer, J.A., and Holm, W.A. (Eds.), 2009. Principles of Modern Radar, Volume I: Basic Techniques. Scitech Publishing.

Rocca, F. 2007. Modeling Interferograms Stacks. *IEEE Trans. Geosci. Remote Sens*. 45, 3289–3299.

Rogan, J., Miller, J., Stow, D., Franklin, J., Levien, L., and Fisher, C. 2003. Land-cover change monitoring with classification trees using Landsat TM and ancillary data. *Photogramm. Eng. and Remote Sens.* 69, 793–804.

Rosenqvist, A., Shimada, M., Ito, N., and Watanabe, M. 2007. ALOS PALSAR: a pathfinder mission for global-scale monitoring of the environment *IEEE Trans. Geosci. and Remote Sens.* 45, pp. 3307-3316

Rouault, M., and Richard, Y. 2005. Intensity and spatial extent of droughts in southern Africa, *Geophysical Research Letters*, 32, 15702.

Safriel, U., Adeel, Z., Niemeijer, D., Puigdefabregas, J., White, R., Lal, R., Winslow, M., Ziedler, J., Prince, S., Archer, E., King, C., Shapiro, B., Wessels, K., Nielsen, T., Portnov, B., Reshef, I., Thonell, J., Lachman, E., and McNab, D. 2005. Dryland systems. In R.M. Hassan, R.J. Scholes & N. Ash (Eds.) Millenium Ecosystem Assessment: Ecosystems and Human Well-being: Current State and Trends: Findings of the Condition and Trends Working Group. Washington, DC: Island Press, 623-662.

Sanderson, E.W., Jaiteh, M., Levy, M.A., Redford, K.H., Wannebo, A.V., and Woolmer, G. 2002. The Human Footprint and the Last of the Wild. *BioScience,* 52: 891–904.

Santini, N.S., Hua, Q.; Schmitz, N., and Lovelock, C.E. 2013. Radiocarbon Dating and Wood Density Chronologies of Mangrove Trees in Arid Western Australia. *PLoS ONE*, 8, e80116.

Santoro, M., Shvidenko, A., McCallum, I., Askne, J., and Schmullius, C. 2007. Properties of ERS-1/2 coherence in the Siberian boreal forest and implications for stem volume retrieval. *Remote Sens. Environ*. 106, 154–172.

Santoro, M., Wegmüller, U., and Askne, J. 2010. Signatures of ERS—Envisat Interferometric SAR Coherence and Phase of Short Vegetation: An analysis in the case of maize fields, *IEEE Trans. Geosci. Remote Sens.*, 48, 4, pp. 1702–1713.

Santoro, M., Wegmüller, U., Lamarche, C., Bontemps, S., Defourny, P., and Arino, O. 2015. Strengths and weaknesses of multi-year Envisat ASAR backscatter measurements to map permanent open water bodies at global scale. *Remote Sens. of Enviro.* 171, 185–201.

Santoro, M., Wegmüller, U., and Askne, J. 2018. Forest stem volume estimation using C-band interferometric SAR coherence data of the ERS-1 mission 3-days repeat-interval phase. *Remote Sen. of Environ.* 216, 684–696

Schönert, M., Weichelt, H., Zillmann, E., and Jürgens, C. 2014. Derivation of tasseled cap coefficients for RapidEye data. In Proceedings of the SPIE 9245, Earth Resources and Environmental Remote Sensing/GIS Applications V, Amsterdam. The Netherlands, 23–25 September; p. 92450Q.

Sheppard, C.R.C., Price, A.R.G., and Roberts, C.M. 1992. Marine Ecology of the Arabian Region: Patterns and Processes in Extreme Tropical Environments Academic Press, London.

Shimada, M., Isoguchi, O., Tadono, T., and Isono, K. 2009. PALSAR radiometric and geometric calibration. *IEEE Trans. Geosci. Remote Sens.* 47, 3915–3932.

Simard, M., Hensley, S., and Lavalle, M. 2012. An empirical assessment of temporal decorrelation using the uninhabited aerial vehicle synthetic aperture radar over forested landscapes. *Remote Sens*. 4, 975–986.

Siqueira, M.F. and Durigan, G. 2007. Modelagem da distribuicaogeografica de especieslenhosas de cerrado no Estado de Sao Paulo. *Revista Brasileira de Botaanica* 30: 239–249.

Skujins, J. 1991. Semiarid Lands and Deserts: Soil Resource and Reclamation. Boca Raton: CRC Press.

Small, D. 2011. Flattening gamma: Radiometric terrain correction for SAR imagery. *IEEE Trans. Geosci. Remote Sens.* 49, 3081–3093.

Souza-Filho, P.W.M., Paradella, W.R., Rodrigues, S.W.P., Costa, F.R., Mura, J.C., and Gonçalves, F.D. 2011. Discrimination of coastal wetland environments in the Amazon region based on multi-polarized L-band airborne Synthetic Aperture Radar imagery. *Estuar. Coast. Shelf Sci.* 95, 88–98.

Spalding, M.D., Blasco, F., and Field, C.D. 1997. *World Mangrove Atlas*; International Society for Mangrove Ecosystems: Okinawa, Japan.

Stafford Smith, M., Abel, N., Walker, B., and Chapin III, F.S. 2009. Drylands: Coping with Uncertainty, Thresholds, and Changes in State. In F.S. Chapin III, G.P. Kofinas, and C. Folke (Eds.) Principles of Ecosystem Stewardship. New York: Springer, 171-195.

Stellmes, M., Sonnenschein, R., Röder, A.,Udelhoven T., Sommer, S., and Hill, J., 2015. Land degradation assessment and monitoring of dry lands. In Thenkabail, P.S. (Editor), Remote Sensing of Water Resources, Disasters, and Urban Studies, CRC Press, pp. 417–451. ISBN 978148221791 9.

Sun, G., Ranson, K.J., Guo, Z., Zhang, Z., Montesano, P., and Kimes, D. 2011. Forest Biomass Mapping from Lidar and Radar Synergies. *Remote Sens. Environ.* 115, 2906–2916.

Taylor, P.J. 1977. *Quantitative Methods in Geography: An Introduction to Spatial Analysis*; Houghton Mifflin Boston: Boston, MA, USA.

Templeton A. 2002. Out of Africa again and again. Nature 416: 45-51.

Thomas, D.S.G., and Middleton, N.J. 1994. Desertification: Exploding the Myth. Wiley, Chichester 194pp.

Torres, R., Snoeij, P., Geudtner, D., Bibby, D., Davidson, M., Attema, E., Potin, P., Rommen, B., Floury, N., Brown, M., Traver, I.N., Deghaye, P., Duesmann, B., Rosich, B., Miranda, N., Bruno, C., L'Abbate, M., Croci, R., Pietropaolo, A., Huchler, M., and Rostan, F. 2012. Gmes Sentinel-1 mission. *Remote Sens. of Environ.* 120, 9–24.

Treuhaft, R.N., Law, B.E., and Asner, G.P. 2004. Forest attributes from radar interferometric structure and its fusion with optical remote sensing. *Bioscience* 54, 561–571.

Tucker, C.J. 1979. Red and photographic infrared linear combinations for monitoring vegetation. *Remote Sens. Environ.* 8, 127–150.

Twilley, R.R., and Rivera-Monroy, V.H. 2005. Developing performance measures of mangrove wetlands using simulation models of hydrology, nutrient biogeochemistry, and community dynamics. *J. Coast. Res.* 40, 79–93.

Tyc, G., Tulip, J., Schulten, D., Krischke, M., and Oxfort, M. 2005. The RapidEye mission. *Des. Acta Astronaut*. 56, 213–219.

United Nations Convention to Combat Desertification (UNCCD), 2005: An Introduction to the United Nations Convention to Combat Desertification.

Van Der Linden, S., and Hostert, P. 2009. The influence of urban structures on impervious surface maps from airborne hyperspectral data. *Remote Sens. Environ.* 113, 2298–2305.

Vapnik, V. 1982. *Estimation of Dependences Based on Empirical Data*; Springer Series in Statistics; Springer: Secaucus, NJ, USA.

Vermote, E., Justice, C., Claverie, M., and Franch, B. 2016. Preliminary analysis of the performance of the Landsat 8/OLI land surface reflectance product. *Remote Sensing of Environment*, 185, 46–56.

Vo, Q.T., Oppelt, N., Leinenkugel, P., and Kuenzer, C. 2013. Remote sensing in mapping mangrove ecosystems - An object-based approach. *Remote Sens*. 5, 183–201.

Vogel, C., and van Zyl, K. 2016. Drought: In Search of Sustainable Solutions to a Persistent, 'Wicked' Problem in South Africa. In Salzmann, N., Huggel, C., Nussbaumer, S. U., & Ziervogel, G. (Eds.), Climate Chang Adaptation Strategies – An upstream-downstream Perspective (pp. 195–211), Springer International Publishing, Switzerland.

Voormansik, k., Jagdhuber, T., Olesk, A., Hajnsek, I., and Papathanassiou, K.P. 2013. Towards a detection of grassland cutting practices with dual polarimetric TerraSAR-X data. *International Journal of Remote Sensing*, 34, 8081–8103.

Waleska, S., Rodrigues, P., Walfir, P., and Souza-Filho, M. 2011. Use of Multi-Sensor Data to Identify and Map Tropical Coastal Wetlands in the Amazon of Northern Brazil. *Wetlands.* 31, 11–23.

Walters, B.B., Roennbaeck, P., Kovacs, J., Crona, B., Hussain, S., Badola, R., Primavera, J.H., Barbier, E.B., and Dahdouh-Guebas, F. 2008. Ethnobiology, socio-economics and adaptive management of mangroves: A review. *Aquat. Bot.* 89, 220–236.

Wang, Z., Liu, C., and Huete, A. 2002. From AVHRR-NDVI to MODIS-EVI: Advances in vegetation index research. *Acta Ecol. Sin*., 23, 979–987.

Wang, L., Silván-Cárdenas, J.L., and Sousa, W.P. 2008. Neural Network Classification of Mangrove Species from Multi-seasonal Ikonos Imagery. *Photogram. Eng. Remote Sens.* 74, 921–927.

Wang, L., Sousa, W.P., Gong, P., and Biging, G.S. 2004. Comparison of IKONOS and QuickBird images for mapping mangrove species on the Caribbean coast of Panama. *Remote Sens. Environ.* 91, 432–440.

Wang, X., Ge, L., and Li, X. 2013. Pasture Monitoring Using SAR with COSMO-SkyMed, ENVISAT ASAR, and ALOS PALSAR in Otway, Australia. *Remote Sensing*, 5, 3611-3636.

Wang, Z., Liu, C., and Huete, A. 2002. From AVHRR-NDVI to MODIS-EVI: Advances in vegetation index research. *Acta Ecol. Sin*. 23, 979–987.

Watson, R. T., Noble, I. R., Bolin, B., Ravindranath, N. H., Verardo D. J., and Dokken, D. J. 2000. Land use, land-use change, and forestry: special report of the Intergovernmental Panel on Climate Change. Cambridge: Cambridge Univ. Press.

Wdowinski, S., and Eriksson, S. 2009. *EOS Trans. Am. Geophys. Union*, 90, 153.

Wegmüller, U. 1998. SAR interferometric and differential interferometric processing. In T. I. Stein (Ed.), IEEE international Geoscience and Remote Sensing Symposium IGARSS (pp. 1106–1108). Seattle, USA: IEEE Publications.

Wegmüller, U. 1999. Automated terrain corrected SAR geocoding. In Proceedings of the IGARSS 1999, Hamburg, Germany, 28 June–2 July.

Wei, M., and Sandwell, D.T. 2010. Decorrelation of L-band and C-band interferometry over vegetated areas in California," *IEEE Trans. Geosci. Remote Sens.*, vol. 48, no. 7, pp. 2942–2952.

Weigelt, A., Weisser, W.W., Buchmann, N., and Scherer-Lorenzen, M. 2009. Biodiversity for multifunctional grasslands: equal productivity in high-diversity low-input and low-diversity high-input systems. *Biogeosciences*, 6, 1695-1706.

Wessels, K.J., Prince, S.D., Frost, P.E., and van Zyl, D. 2007. Can human-induced land degradation be distinguished from the effects of rainfall variability? A case study in South Africa. *Journal of Arid Environments*, 68, 271–297.

White R., Murray S., and Rohweder M. 2000. Pilot analysis of global ecosystems: grassland ecosystems technical report. World Resources Institute, Washington, DC.

Wilhite, D.A. 2000. Chapter 1 Drought as a Natural Hazard: Concepts and Definitions. In *Drought: A Global Assessment*; Wilhite, D.A., Ed.; Routledge: London, UK, pp. 3–18.

Wilhite, D.A., and Buchanan-Smith, M. 2005. Drought as hazard: understanding the natural and social context. In: Wilhite, D.A., (Ed.), Drought and Water Crises: Science, Technology and Management Issues (pp. 3-29). Boca Raton, FL: Taylor and Francis.

Wiseman, G., McNairn, H., Homayouni, S., and Shang, J. 2014. RADARSAT-2 polarimetric SAR response to crop biomass for agricultural production monitoring. *IEEE Journal of Selected Topics in Applied Earth Observation and Remote Sensing*, 7, 4461–4471.

Woodhouse I.H. 2006. Introduction to microwave remote sensing. CRC Press, Taylor & Francis Group, Boca Raton.

Wulder, M.A., and Franklin, S.E. (Eds.), 2003. Remote Sensing of Forest Environments: Concepts and Case Studies, 1st ed. Kluwer Academic Publishers, Boston, Dordrecht, London.

Wulder, M.A., Hall, R.J., Coops, N.C., and Franklin, S.E. 2004. High spatial resolution remotely sensed data for ecosystem characterization. *BioScience* 54, 511–521.

Xiaoxiao, L., Soe, W.M., Yujia, Z., Chritopher, G., Xiaoxiang, Z., and Billie, L.T. 2014. Object-based land cover classification for metropolitan Phoenix, Arizona, using aerial photography. *Int. J. Appl. Earth Obs. Geoinf*. 33, 321–330.

Zahran, M.A., and Willis, A.J. 2009. *The Vegetation of Egypt*, 2nd ed.; Chapman & Hall: London, UK, 424p.

Zalite, K., Antropov, O., Praks, J., Voormansik, K., and Noorma, M. 2016. Monitoring of agricultural grasslands with time series of X-band repeat-pass interferometric SAR, *IEEE J. Select. Topics Appl. Earth Observ. Remote Sens.*, 9, 8, pp. 3687–3697.

Zebker, H., and Villasenor, J. 1992. Decorrelation in interferometric radar echoes. *IEEE Trans. Geosci. Remote Sens*. 45, 950–959.

Zlinszky, A., Heilmeier, H., Balzter, H., Czúcz, B., and Pfeifer, N. 2015. Remote Sensing and GIS for Habitat. Quality Monitoring: New Approaches and Future Research. *Remote Sens*. 7, 7987–7994.

Appendices

Appendix 1. Backscattering coefficients of VH polarization in (dB) extracted from Sentinel-1 SAR data, covering the commercial grasslands in the study area in Eastern Cape, during the first (2015/2016) and second (2016/2017) growing seasons.

G	Date	S1	S2	S3	S4	S5	S6
1	13-Oct-15	-21.45	-21.29	-20.69	-21.97	-22.35	-20.29
1	25-Oct-15	-18.87	-19.32	-19.31	-17.83	-20.32	-18.87
1	6-Nov-15	-22.90	-23.23	-21.76	-22.13	-22.60	-21.32
1	30-Nov-15	-21.15	-21.53	-21.77	-21.83	-22.72	-22.18
1	12-Dec-15	-21.48	-22.01	-21.77	-23.30	-21.15	-22.81
1	24-Dec-15	-21.27	-22.02	-22.86	-23.45	-23.73	-23.03
1	5-Jan-16	-21.47	-22.42	-22.62	-23.67	-22.82	-23.00
1	17-Jan-16	-20.57	-21.15	-21.76	-21.56	-22.53	-21.73
1	29-Jan-16	-20.23	-19.47	-18.34	-22.08	-22.94	-20.90
1	10-Feb-16	-21.51	-22.63	-21.13	-21.97	-22.86	-21.43
1	22-Feb-16	-21.58	-21.88	-21.02	-21.46	-22.49	-21.35
1	5-Mar-16	-21.64	-21.83	-21.53	-22.17	-22.18	-21.51
		S7	**S8**	**S9**	**S10**	**S11**	**S12**
1	13-Oct-15	-21.24	-22.82	-21.26	-20.20	-21.35	-21.23
1	25-Oct-15	-19.76	-18.95	-19.04	-18.82	-19.99	-20.13
1	6-Nov-15	-21.37	-22.29	-21.93	-22.17	-22.72	-22.50
1	30-Nov-15	-21.57	-21.85	-21.71	-20.88	-22.16	-21.62
1	12-Dec-15	-21.41	-20.19	-19.23	-18.31	-19.75	-19.36
1	24-Dec-15	-21.63	-22.05	-21.80	-22.67	-22.10	-23.17
1	5-Jan-16	-22.29	-21.89	-21.29	-22.05	-22.10	-23.40
1	17-Jan-16	-20.65	-21.62	-21.29	-20.71	-20.98	-22.45
1	29-Jan-16	-20.34	-21.28	-20.08	-18.99	-20.53	-21.06
1	10-Feb-16	-21.57	-22.32	-21.12	-21.54	-22.06	-22.61
1	22-Feb-16	-21.01	-22.16	-21.41	-20.73	-22.09	-22.48
1	5-Mar-16	-21.50	-22.85	-21.39	-21.85	-22.17	-22.12
		S1	**S2**	**S3**	**S4**	**S5**	**S6**
1	7-Oct-16	-23.40	-23.95	-22.49	-23.26	-23.77	-22.40
1	19-Oct-16	-20.61	-21.96	-22.69	-22.42	-23.71	-21.78
1	12-Nov-16	-20.08	-20.42	-20.66	-21.34	-21.83	-20.87
1	24-Nov-16	-20.70	-22.21	-21.87	-21.88	-22.26	-21.21
1	6-Dec-16	-21.75	-22.58	-21.57	-22.32	-22.86	-21.74
1	18-Dec-16	-21.55	-21.98	-20.74	-21.35	-22.40	-21.33
1	11-Jan-17	-20.58	-21.85	-21.20	-22.82	-22.65	-22.24
1	23-Jan-17	-22.01	-21.14	-18.23	-18.89	-19.94	-19.26
1	4-Feb-17	-20.11	-20.82	-19.93	-20.88	-21.16	-20.35
1	16-Feb-17	-20.21	-20.23	-19.78	-21.26	-21.24	-20.80

1	12-Mar-17	-21.22	-20.29	-20.55	-21.38	-22.48	-20.78
1	24-Mar-17	-19.52	-20.07	-18.03	-19.60	-20.47	-19.57
		S7	**S8**	**S9**	**S10**	**S11**	**S12**
1	7-Oct-16	-21.59	-22.58	-24.86	-24.23	-25.41	-23.54
1	19-Oct-16	-21.35	-23.06	-24.59	-23.51	-25.77	-23.87
1	12-Nov-16	-20.88	-21.87	-22.14	-20.09	-20.99	-22.71
1	24-Nov-16	-20.47	-22.34	-22.81	-20.16	-22.96	-21.80
1	6-Dec-16	-20.64	-22.90	-22.05	-21.31	-22.53	-22.51
1	18-Dec-16	-20.30	-22.65	-22.03	-21.17	-22.68	-21.57
1	11-Jan-17	-21.15	-23.03	-22.02	-20.85	-21.46	-23.29
1	23-Jan-17	-18.62	-18.52	-17.66	-18.30	-18.35	-18.40
1	4-Feb-17	-20.78	-20.11	-20.95	-20.24	-20.15	-21.65
1	16-Feb-17	-20.27	-20.98	-20.80	-19.86	-21.05	-21.43
1	12-Mar-17	-20.34	-22.22	-22.19	-20.76	-22.75	-21.58
1	24-Mar-17	-18.60	-19.01	-20.18	-18.91	-19.40	-19.92

Appendix 2. Backscattering coefficients of VH polarization in (dB) extracted from Sentinel-1 SAR data, covering the communal grasslands in the study area in Eastern Cape, during the first (2015/2016) and second (2016/2017) growing seasons.

G	Date	S1	S2	S3	S4	S5	S6
2	13-Oct-15	-24.93	-25.62	-22.63	-20.28	-25.22	-20.30
2	25-Oct-15	-20.79	-22.98	-22.41	-19.11	-22.64	-19.89
2	6-Nov-15	-24.53	-25.23	-22.34	-19.37	-25.03	-20.45
2	30-Nov-15	-24.41	-25.30	-22.63	-20.23	-25.19	-20.46
2	12-Dec-15	-24.67	-25.08	-22.49	-19.56	-25.33	-20.91
2	24-Dec-15	-25.07	-24.16	-21.96	-18.91	-24.76	-19.93
2	5-Jan-16	-26.25	-25.61	-24.10	-20.88	-26.00	-21.86
2	17-Jan-16	-26.05	-25.56	-23.81	-20.92	-25.74	-21.69
2	29-Jan-16	-25.36	-25.66	-22.72	-20.27	-24.70	-21.16
1	10-Feb-16	-24.05	-23.76	-21.10	-19.19	-23.69	-20.88
2	22-Feb-16	-22.87	-23.50	-21.60	-19.47	-21.83	-21.24
2	5-Mar-16	-23.01	-23.20	-20.92	-19.57	-21.48	-21.07
		S7	**S8**	**S9**	**S10**	**S11**	**S12**
2	13-Oct-15	-21.45	-22.47	-21.49	-24.31	-21.70	-23.37
2	25-Oct-15	-21.17	-21.06	-20.30	-23.87	-21.08	-22.68
2	6-Nov-15	-21.24	-21.54	-20.92	-24.01	-21.36	-23.55
2	30-Nov-15	-20.83	-22.95	-20.49	-24.59	-22.55	-24.29
2	12-Dec-15	-21.75	-22.16	-21.72	-24.41	-22.76	-22.41
2	24-Dec-15	-20.64	-20.38	-19.16	-24.02	-22.77	-21.20
2	5-Jan-16	-22.27	-23.42	-21.97	-24.62	-23.35	-24.53
2	17-Jan-16	-22.37	-23.13	-21.92	-24.32	-23.31	-22.75
2	29-Jan-16	-22.11	-22.15	-21.43	-24.27	-22.52	-21.96
2	10-Feb-16	-21.50	-21.98	-21.39	-22.98	-21.55	-21.27
2	22-Feb-16	-21.18	-22.16	-21.63	-22.51	-21.18	-21.22

2	5-Mar-16	-21.37	-21.36	-21.01	-22.33	-21.77	-21.80
		S1	**S2**	**S3**	**S4**	**S5**	**S6**
2	7-Oct-16	-24.64	-25.31	-22.89	-20.82	-25.12	-21.60
2	19-Oct-16	-22.58	-25.27	-22.82	-20.63	-25.51	-21.46
2	12-Nov-16	-20.87	-25.22	-21.14	-19.23	-24.06	-20.69
2	24-Nov-16	-21.53	-25.09	-22.71	-19.59	-24.92	-20.88
2	6-Dec-16	-24.18	-25.19	-23.62	-20.02	-24.86	-21.16
2	18-Dec-16	-23.66	-24.15	-22.62	-19.47	-24.19	-21.15
2	11-Jan-17	-24.34	-25.56	-23.23	-19.32	-25.05	-20.43
2	23-Jan-17	-17.33	-22.12	-18.91	-18.54	-21.72	-19.69
2	4-Feb-17	-21.01	-22.33	-19.61	-19.01	-21.69	-20.16
2	16-Feb-17	-21.20	-22.15	-19.37	-18.54	-21.21	-19.83
2	12-Mar-17	-23.52	-22.37	-21.14	-18.76	-22.63	-20.49
2	24-Mar-17	-20.45	-20.18	-19.64	-18.46	-21.12	-19.69
		S7	**S8**	**S9**	**S10**	**S11**	**S12**
2	7-Oct-16	-22.41	-21.98	-22.27	-23.80	-22.49	-22.11
2	19-Oct-16	-22.12	-22.06	-22.20	-24.37	-22.13	-21.91
2	12-Nov-16	-20.47	-21.83	-20.57	-22.63	-21.90	-20.84
2	24-Nov-16	-20.89	-21.51	-21.33	-23.30	-22.30	-21.20
2	6-Dec-16	-21.56	-22.88	-20.95	-24.26	-22.05	-22.21
2	18-Dec-16	-21.31	-21.86	-20.84	-23.37	-22.15	-21.46
2	11-Jan-17	-21.15	-22.64	-19.93	-24.39	-23.17	-21.10
2	23-Jan-17	-19.77	-20.06	-19.26	-21.25	-20.81	-20.20
2	4-Feb-17	-21.06	-21.28	-19.95	-21.86	-21.83	-21.07
2	16-Feb-17	-20.65	-20.73	-19.37	-21.34	-21.32	-18.89
2	12-Mar-17	-21.46	-21.74	-20.28	-22.08	-20.94	-21.21
2	24-Mar-17	-20.02	-20.02	-19.34	-20.77	-20.65	-20.46

Appendix 3. Backscattering coefficients of VV polarization in (dB) extracted from Sentinel-1 SAR data, covering the commercial grasslands in the study area in Eastern Cape, during the first (2015/2016) and second (2016/2017) growing seasons.

G	Date	S1	S2	S3	S4	S5	S6
1	13-Oct-15	-14.72	-14.21	-15.19	-16.33	-16.07	-14.29
1	25-Oct-15	-13.05	-12.78	-13.14	-13.29	-14.18	-13.46
1	6-Nov-15	-13.75	-15.56	-14.89	-14.82	-16.33	-15.37
1	30-Nov-15	-15.33	-16.82	-16.04	-15.94	-17.60	-16.53
1	12-Dec-15	-16.07	-16.19	-16.13	-17.22	-16.16	-17.28
1	24-Dec-15	-15.93	-17.00	-17.16	-17.57	-18.24	-18.02
1	5-Jan-16	-15.62	-17.55	-16.13	-17.46	-17.56	-17.41
1	17-Jan-16	-15.07	-14.91	-14.78	-15.28	-16.85	-16.00
1	29-Jan-16	-15.43	-14.88	-13.42	-15.08	-17.33	-15.90
1	10-Feb-16	-16.19	-16.46	-16.04	-15.87	-17.40	-16.02
1	22-Feb-16	-16.94	-16.75	-14.54	-15.20	-17.20	-15.94
1	5-Mar-16	-16.38	-16.23	-15.94	-16.34	-17.46	-16.32

		S7	S8	S9	S10	S11	S12
1	13-Oct-15	-14.77	-13.67	-14.79	-14.60	-14.59	-14.80
1	25-Oct-15	-14.08	-11.26	-13.76	-12.52	-13.58	-13.23
1	6-Nov-15	-14.79	-15.98	-15.53	-14.84	-16.38	-15.27
1	30-Nov-15	-16.29	-16.61	-16.53	-15.55	-16.24	-17.22
1	12-Dec-15	-17.35	-14.28	-14.23	-14.16	-14.55	-13.87
1	24-Dec-15	-17.77	-17.15	-16.49	-17.23	-16.88	-18.44
1	5-Jan-16	-17.06	-17.26	-16.37	-16.68	-16.31	-16.31
1	17-Jan-16	-15.74	-16.57	-15.85	-14.24	-15.83	-16.97
1	29-Jan-16	-16.23	-16.87	-14.87	-14.20	-15.24	-15.38
1	10-Feb-16	-17.10	-17.99	-16.10	-15.90	-16.93	-16.63
1	22-Feb-16	-16.65	-17.10	-15.75	-14.59	-16.27	-16.57
1	5-Mar-16	-16.06	-16.85	-15.53	-16.61	-17.40	-15.91
		S1	**S2**	**S3**	**S4**	**S5**	**S6**
1	7-Oct-16	-17.03	-19.82	-17.11	-15.61	-18.32	-16.74
1	19-Oct-16	-15.14	-15.26	-16.79	-15.34	-17.94	-16.43
1	12-Nov-16	-14.96	-15.03	-15.26	-16.67	-15.75	-15.63
1	24-Nov-16	-16.33	-16.58	-16.25	-16.10	-16.92	-16.26
1	6-Dec-16	-16.62	-17.69	-16.12	-16.70	-17.23	-16.77
1	18-Dec-16	-16.40	-16.72	-15.11	-15.30	-17.37	-15.90
1	11-Jan-17	-16.76	-16.99	-16.24	-16.88	-17.90	-16.88
1	23-Jan-17	-15.94	-17.12	-13.56	-14.30	-15.34	-14.41
1	4-Feb-17	-15.56	-16.26	-14.36	-15.35	-16.34	-15.47
1	16-Feb-17	-15.39	-15.90	-14.31	-15.97	-16.40	-15.17
1	12-Mar-17	-16.20	-16.82	-15.31	-15.87	-17.54	-15.88
1	24-Mar-17	-15.58	-15.98	-13.50	-15.32	-15.63	-14.52
		S7	**S8**	**S9**	**S10**	**S11**	**S12**
1	7-Oct-16	-16.58	-17.08	-17.98	-16.24	-19.74	-17.83
1	19-Oct-16	-15.74	-17.21	-17.65	-15.19	-18.90	-17.22
1	12-Nov-16	-15.79	-14.55	-15.96	-14.32	-14.91	-16.82
1	24-Nov-16	-15.95	-15.12	-16.37	-14.73	-17.72	-16.56
1	6-Dec-16	-16.20	-17.29	-16.74	-16.03	-16.41	-17.13
1	18-Dec-16	-15.95	-16.68	-16.78	-14.88	-17.11	-15.52
1	11-Jan-17	-15.57	-16.41	-16.68	-14.91	-15.60	-16.31
1	23-Jan-17	-13.70	-13.82	-13.01	-13.16	-12.71	-12.01
1	4-Feb-17	-15.46	-15.34	-14.67	-14.67	-14.56	-16.06
1	16-Feb-17	-15.30	-15.16	-15.80	-13.91	-15.83	-15.81
1	12-Mar-17	-15.96	-17.70	-17.00	-15.54	-17.18	-16.37
1	24-Mar-17	-15.00	-14.29	-14.65	-13.93	-15.04	-14.35

Appendix 4. Backscattering coefficients of VV polarization in (dB) extracted from Sentinel-1 SAR data, covering the communal grasslands in the study area in Eastern Cape, during the first (2015/2016) and second (2016/2017) growing seasons.

G	Date	S1	S2	S3	S4	S5	S6
2	13-Oct-15	-17.11	-18.03	-17.39	-14.82	-18.06	-14.79
2	25-Oct-15	-11.80	-12.80	-16.95	-13.17	-12.69	-14.20
2	6-Nov-15	-17.31	-18.58	-16.53	-14.61	-17.77	-15.22
2	30-Nov-15	-17.06	-18.12	-15.78	-14.64	-18.04	-15.34
2	12-Dec-15	-17.97	-18.76	-18.29	-15.44	-18.99	-16.88
2	24-Dec-15	-18.79	-16.34	-18.13	-14.65	-17.20	-15.04
2	5-Jan-16	-18.72	-19.69	-18.14	-16.37	-19.05	-17.29
2	17-Jan-16	-18.50	-19.65	-18.22	-16.31	-19.24	-17.09
2	29-Jan-16	-16.72	-18.08	-14.80	-14.95	-17.18	-15.30
1	10-Feb-16	-17.13	-17.50	-17.07	-15.57	-16.74	-17.13
2	22-Feb-16	-16.54	-16.55	-17.18	-15.49	-16.21	-17.32
2	5-Mar-16	-17.18	-16.64	-16.71	-15.37	-15.43	-16.88
		S7	**S8**	**S9**	**S10**	**S11**	**S12**
2	13-Oct-15	-15.60	-17.49	-15.63	-17.37	-16.20	-16.97
2	25-Oct-15	-13.53	-14.95	-13.31	-17.11	-15.79	-15.71
2	6-Nov-15	-15.82	-17.11	-15.67	-17.65	-16.21	-17.36
2	30-Nov-15	-14.82	-17.62	-14.08	-17.97	-16.98	-17.29
2	12-Dec-15	-16.76	-18.47	-16.13	-19.11	-17.87	-17.30
2	24-Dec-15	-14.58	-15.98	-12.88	-18.82	-17.08	-16.38
2	5-Jan-16	-17.58	-19.51	-16.91	-19.77	-18.32	-18.74
2	17-Jan-16	-17.98	-19.44	-16.55	-18.73	-18.23	-17.63
2	29-Jan-16	-15.87	-17.40	-14.68	-17.89	-16.95	-15.74
2	10-Feb-16	-16.40	-17.82	-16.72	-17.11	-17.39	-15.98
2	22-Feb-16	-17.24	-17.72	-16.57	-16.96	-17.15	-15.97
2	5-Mar-16	-16.94	-17.61	-14.87	-16.98	-17.33	-16.39
		S1	**S2**	**S3**	**S4**	**S5**	**S6**
2	7-Oct-16	-17.81	-19.55	-17.98	-16.36	-18.87	-17.05
2	19-Oct-16	-13.21	-18.65	-18.32	-16.29	-18.63	-16.48
2	12-Nov-16	-12.05	-16.77	-13.39	-14.82	-17.79	-14.48
2	24-Nov-16	-12.88	-18.28	-17.91	-15.83	-18.72	-16.76
2	6-Dec-16	-17.21	-19.03	-18.05	-16.02	-19.23	-16.28
2	18-Dec-16	-17.06	-15.82	-17.40	-15.25	-16.43	-16.58
2	11-Jan-17	-16.58	-19.38	-16.59	-15.27	-19.85	-14.75
2	23-Jan-17	-10.01	-12.73	-12.94	-13.90	-12.64	-14.14
2	4-Feb-17	-11.47	-12.79	-12.21	-14.57	-12.38	-14.15
2	16-Feb-17	-12.97	-14.32	-12.87	-14.11	-13.09	-14.48
2	12-Mar-17	-16.63	-16.02	-16.68	-15.12	-16.84	-16.47
2	24-Mar-17	-13.12	-13.86	-14.78	-14.21	-14.33	-14.45
		S7	**S8**	**S9**	**S10**	**S11**	**S12**
2	7-Oct-16	-17.08	-18.61	-17.04	-18.26	-18.66	-17.60
2	19-Oct-16	-17.05	-18.64	-17.27	-18.93	-18.22	-16.78

2	12-Nov-16	-13.86	-16.85	-13.97	-16.42	-16.72	-15.48
2	24-Nov-16	-17.51	-17.84	-16.68	-17.95	-17.67	-16.66
2	6-Dec-16	-17.04	-19.20	-16.49	-18.93	-17.75	-17.07
2	18-Dec-16	-16.65	-17.85	-16.40	-17.89	-17.73	-17.05
2	11-Jan-17	-15.16	-17.84	-14.60	-19.18	-17.61	-15.45
2	23-Jan-17	-13.38	-15.48	-14.41	-12.49	-15.78	-15.27
2	4-Feb-17	-14.10	-16.02	-14.83	-12.66	-15.30	-15.93
2	16-Feb-17	-14.41	-16.37	-14.50	-12.96	-15.65	-13.77
2	12-Mar-17	-16.74	-18.05	-16.45	-16.30	-16.67	-16.43
2	24-Mar-17	-14.77	-16.30	-15.71	-14.19	-16.19	-14.65

Appendix 5. InSAR coherence of VV polarization extracted from Sentinel-1 InSAR data, covering the commercial grasslands in the study area in Eastern Cape, during the first (2015/2016) and second (2016/2017) growing seasons.

G	Pairs	S1	S2	S3	S4	S5	S6
1	13Oct15 - 25Oct15	0.3745	0.4579	0.3824	0.3736	0.3735	0.4740
1	12Dec15 - 05Jan16	0.4631	0.4901	0.4289	0.5526	0.3183	0.5216
1	05Jan16 - 29Jan16	0.4331	0.3730	0.2778	0.5327	0.5275	0.4731
1	05Jan16 - 22Feb16	0.3620	0.3291	0.3592	0.4498	0.3717	0.3671
1	05Jan16 - 05Mar16	0.3741	0.3317	0.3463	0.5102	0.3692	0.3670
1	05Jan16 - 17Mar16	0.3190	0.3225	0.2909	0.3283	0.3343	0.3274
1	29Jan16 - 22Feb16	0.4193	0.3645	0.2792	0.5707	0.4191	0.4833
1	29Jan16 - 05Mar16	0.3874	0.3280	0.3150	0.5306	0.3711	0.4688
1	29Jan16 - 17Mar16	0.3985	0.3865	0.3176	0.3522	0.3216	0.3564
1	22Feb16 - 05Mar16	0.4907	0.4866	0.4834	0.6250	0.4555	0.5484
1	22Feb16 - 17Mar16	0.4058	0.4189	0.4277	0.4295	0.3654	0.4109
1	05Mar16 - 17Mar16	0.4191	0.4497	0.4053	0.3714	0.4445	0.4171
		S7	**S8**	**S9**	**S10**	**S11**	**S12**
1	13Oct15 - 25Oct15	0.4460	0.5853	0.3610	0.3907	0.3148	0.2991
1	12Dec15 - 05Jan16	0.4125	0.3034	0.2975	0.3334	0.3277	0.3196
1	05Jan16 - 29Jan16	0.3106	0.3370	0.3070	0.3181	0.3062	0.2842
1	05Jan16 - 22Feb16	0.3194	0.3604	0.3523	0.3749	0.3538	0.3157
1	05Jan16 - 05Mar16	0.2968	0.3241	0.3341	0.3895	0.3302	0.3429
1	05Jan16 - 17Mar16	0.3265	0.3308	0.3232	0.3440	0.3459	0.3034
1	29Jan16 - 22Feb16	0.3940	0.4016	0.3064	0.4009	0.3151	0.3669
1	29Jan16 - 05Mar16	0.2903	0.3324	0.3237	0.3413	0.2921	0.3366
1	29Jan16 - 17Mar16	0.2955	0.3082	0.3203	0.3575	0.2715	0.3065
1	22Feb16 - 05Mar16	0.3686	0.5343	0.4403	0.4739	0.4850	0.5610
1	22Feb16 - 17Mar16	0.3066	0.3877	0.3794	0.4138	0.4103	0.4154
1	05Mar16 - 17Mar16	0.4519	0.4083	0.4374	0.3931	0.3888	0.4234
		S1	**S2**	**S3**	**S4**	**S5**	**S6**
1	07Oct16 - 19Oct16	0.4664	0.4911	0.6531	0.8317	0.6305	0.4961
1	19Oct16 - 31Oct16	0.4050	0.4144	0.4876	0.7462	0.5534	0.4866
1	31Oct16 - 12Nov16	0.3965	0.3772	0.3661	0.3509	0.4536	0.3712

1	12Nov16 - 24Nov16	0.6013	0.4762	0.3460	0.4237	0.5521	0.4734
1	24Nov16 - 06Dec16	0.4261	0.4033	0.3162	0.4784	0.4774	0.4776
1	06Dec16 - 18Dec16	0.4435	0.4518	0.3374	0.5547	0.4649	0.4643
1	18Dec16 - 23Jan17	0.3655	0.4076	0.2644	0.3022	0.2930	0.3470
1	23Jan17 - 04Feb17	0.4361	0.4743	0.4142	0.4306	0.4461	0.5015
1	04Feb17 - 16Feb17	0.5315	0.5429	0.3897	0.3652	0.3920	0.3623
1	16Feb17 - 28Feb17	0.5877	0.5550	0.3971	0.5282	0.4576	0.5681
1	28Feb17 - 12Mar17	0.5522	0.4117	0.3776	0.6430	0.5262	0.5689
1	12Mar17 - 24Mar17	0.3889	0.5056	0.3931	0.2935	0.3576	0.3630
		S7	**S8**	**S9**	**S10**	**S11**	**S12**
1	07Oct16 - 19Oct16	0.4138	0.8253	0.7106	0.6617	0.7258	0.5318
1	19Oct16 - 31Oct16	0.4472	0.7753	0.5598	0.6152	0.5940	0.4630
1	31Oct16 - 12Nov16	0.4424	0.4527	0.3657	0.3763	0.3303	0.3664
1	12Nov16 - 24Nov16	0.3481	0.6251	0.3895	0.5378	0.4936	0.3426
1	24Nov16 - 06Dec16	0.3981	0.4873	0.4209	0.4296	0.4413	0.3674
1	06Dec16 - 18Dec16	0.4304	0.6070	0.4376	0.4861	0.5203	0.3557
1	18Dec16 - 23Jan17	0.3390	0.3396	0.3318	0.3314	0.2934	0.2979
1	23Jan17 - 04Feb17	0.3499	0.5125	0.3583	0.3693	0.4478	0.3200
1	04Feb17 - 16Feb17	0.3679	0.6048	0.5236	0.4076	0.5667	0.3353
1	16Feb17 - 28Feb17	0.4807	0.5021	0.5255	0.4498	0.5305	0.3731
1	28Feb17 - 12Mar17	0.4345	0.5104	0.5398	0.5777	0.4692	0.5227
1	12Mar17 - 24Mar17	0.2749	0.3562	0.3914	0.3340	0.3882	0.3505

Appendix 6. InSAR coherence of VV polarization extracted from Sentinel-1 InSAR data, covering the communal grasslands in the study area in Eastern Cape, during the first (2015/2016) and second (2016/2017) growing seasons.

G	Pairs	S1	S2	S3	S4	S5	S6
2	13Oct15 - 25Oct15	0.4446	0.5484	0.6607	0.3050	0.5366	0.3673
2	12Dec15 - 05Jan16	0.5397	0.4761	0.4552	0.2715	0.4866	0.3030
2	05Jan16 - 29Jan16	0.4111	0.4035	0.3982	0.3481	0.4074	0.4777
2	05Jan16 - 22Feb16	0.3363	0.3631	0.3289	0.2863	0.3340	0.3731
2	05Jan16 - 05Mar16	0.3424	0.3637	0.3232	0.3098	0.3177	0.4076
2	05Jan16 - 17Mar16	0.3197	0.3532	0.3060	0.2603	0.3219	0.3188
2	29Jan16 - 22Feb16	0.4695	0.5120	0.4782	0.4431	0.4456	0.5144
2	29Jan16 - 05Mar16	0.4168	0.4535	0.4516	0.3732	0.4276	0.4480
2	29Jan16 - 17Mar16	0.3549	0.4349	0.4434	0.3399	0.3510	0.3875
2	22Feb16 - 05Mar16	0.5451	0.6708	0.6204	0.5107	0.6130	0.5213
2	22Feb16 - 17Mar16	0.4473	0.5366	0.4767	0.3935	0.4491	0.4698
2	05Mar16 - 17Mar16	0.4695	0.5518	0.5013	0.4367	0.5038	0.4614
		S7	**S8**	**S9**	**S10**	**S11**	**S12**
2	13Oct15 - 25Oct15	0.4172	0.3414	0.4080	0.7170	0.5737	0.4468
2	12Dec15 - 05Jan16	0.4378	0.2618	0.3808	0.5528	0.5105	0.3458
2	05Jan16 - 29Jan16	0.4479	0.3822	0.4652	0.4682	0.4857	0.4300
2	05Jan16 - 22Feb16	0.4019	0.3358	0.3672	0.3934	0.4012	0.3586

2	05Jan16 - 05Mar16	0.4166	0.3287	0.2900	0.4157	0.4299	0.3570
2	05Jan16 - 17Mar16	0.3565	0.2639	0.2881	0.3533	0.3436	0.3247
2	29Jan16 - 22Feb16	0.5410	0.4842	0.5218	0.5578	0.5219	0.4506
2	29Jan16 - 05Mar16	0.4699	0.3809	0.4019	0.4993	0.4490	0.3835
2	29Jan16 - 17Mar16	0.4632	0.3342	0.3915	0.4508	0.4023	0.3434
2	22Feb16 - 05Mar16	0.6095	0.5066	0.5005	0.5934	0.5902	0.5056
2	22Feb16 - 17Mar16	0.5067	0.3568	0.4548	0.5197	0.4598	0.4114
2	05Mar16 - 17Mar16	0.4932	0.3737	0.6421	0.5236	0.4515	0.4530
		S1	**S2**	**S3**	**S4**	**S5**	**S6**
2	07Oct16 - 19Oct16	0.4173	0.6022	0.6704	0.5922	0.6802	0.6907
2	19Oct16 - 31Oct16	0.4344	0.5454	0.6349	0.5028	0.6379	0.5638
2	31Oct16 - 12Nov16	0.4549	0.5858	0.5578	0.4209	0.6020	0.4697
2	12Nov16 - 24Nov16	0.6737	0.6420	0.5625	0.4896	0.6663	0.5027
2	24Nov16 - 06Dec16	0.4884	0.5965	0.6022	0.4537	0.6338	0.6426
2	06Dec16 - 18Dec16	0.6503	0.5407	0.6289	0.4983	0.4933	0.6225
2	18Dec16 - 23Jan17	0.3656	0.6374	0.4797	0.2679	0.5893	0.3780
2	23Jan17 - 04Feb17	0.6160	0.7888	0.7838	0.3709	0.7291	0.6584
2	04Feb17 - 16Feb17	0.5804	0.6102	0.6732	0.4445	0.6065	0.6783
2	16Feb17 - 28Feb17	0.5147	0.5320	0.5140	0.5058	0.4646	0.6259
2	28Feb17 - 12Mar17	0.5996	0.6003	0.5514	0.5190	0.6199	0.6350
2	12Mar17 - 24Mar17	0.4731	0.6292	0.4624	0.3133	0.5317	0.4255
		S7	**S8**	**S9**	**S10**	**S11**	**S12**
2	07Oct16 - 19Oct16	0.7111	0.6620	0.6748	0.6745	0.6481	0.4547
2	19Oct16 - 31Oct16	0.6578	0.5813	0.5961	0.6251	0.5680	0.4151
2	31Oct16 - 12Nov16	0.5268	0.4694	0.5131	0.5615	0.4798	0.4432
2	12Nov16 - 24Nov16	0.5271	0.5190	0.5589	0.5883	0.5338	0.5515
2	24Nov16 - 06Dec16	0.5906	0.4885	0.5298	0.5864	0.5117	0.4676
2	06Dec16 - 18Dec16	0.6256	0.5822	0.5198	0.6479	0.6315	0.5498
2	18Dec16 - 23Jan17	0.3423	0.2699	0.2956	0.4627	0.2363	0.3208
2	23Jan17 - 04Feb17	0.5961	0.4648	0.5353	0.8130	0.3812	0.5065
2	04Feb17 - 16Feb17	0.6852	0.5967	0.6274	0.6768	0.5265	0.3903
2	16Feb17 - 28Feb17	0.6442	0.5325	0.5680	0.6164	0.5755	0.3878
2	28Feb17 - 12Mar17	0.6052	0.5033	0.6022	0.6039	0.6007	0.5967
2	12Mar17 - 24Mar17	0.3995	0.3102	0.3631	0.5327	0.3590	0.3828

To reference this thesis:

Abdel-Hamid, A. 2020. Spaceborne SAR remote sensing for monitoring of vegetation dynamics in arid and semi-arid environment, Ph.D. Thesis, University of Bonn.